An Investigation into the Minimum Dimensionality Required for Accurate Simulation of Proton Exchange Membrane Fuel Cells by the Comparison Between 1- and 3-Dimension Models

by

Karthik Shekhar

Submitted to the Department of Chemical Engineering
in partial fulfilment of the requirements for the degree of

Master of Science in Chemical Engineering

at the

University of Cape Town

08 May 2013

Supervised by:

A/Prof. Randhir Rawatlal

Dr. Olaf Conrad

PLAGIARISM DECLARATION

I, Karthik Shekhar, hereby certify that this submission is my own work, with the exception of the obtained, and referenced, literature resources, as well as the information and knowledge obtained from the project supervisors.

Name: Signature: Date:

ABSTRACT

Hydrogen has been studied intensively as a potential energy carrier as it allows for a reduced carbon footprint in the environment. Fuel cell (FC) technology has been studied in detail to implement hydrogen as well as other renewable sources as a feasible fuel. Further development in fuel cell design is hampered by the lack of fundamental models which reveal the physical and chemical interactions. While computational fluid dynamics simulations are available, the timeframe for solving these simulations renders them unfeasible in any rigorous FC design optimisation. The objective of the present investigation was to determine the minimum dimension of a mathematical model that can accurately simulate processes occurring within a proton exchange membrane fuel cell (PEMFC). To this end, 1-D (directional axis perpendicular to the membrane) and 3-D steady state isothermal mathematical models were developed and simulated in order to investigate the transport of reactant species through the various layers of the cell at the anode side.

The 1-D model was developed using Fick's Law and the control volume approach to model mass transfer in the cell. An assumption was made that the pressure gradient through the gas diffusion layer (GDL) is negligible, leading to the transport process in the GDL being modelled as a diffusion-driven process. To simulate the catalyst layer in the 1-D system, an interfacial model was proposed whereby the reactants are consumed at the surface of the catalyst layer. To obtain the boundary conditions of the model, an assumption was made that the concentration gradient is linear through each of the zones. This was done as a first estimate to obtain the concentrations at each of the interfaces (flow channel/GDL and GDL/catalyst layer). The 3-D model was developed using a complete Navier-Stokes approach. The GDL and catalyst layers were modelled as continua accounting for the porosity and permeability of each layer. A momentum sink term was developed based on Darcy's law for each layer in all three directions of interest. To simulate the rate of hydrogen oxidation, a species sink term was developed based on current density for the catalyst layer continuum outlined above. Results obtained from investigating the anode side rather than the entire cell for each model were thought to be sufficient to perform a comparative analysis in acquiring a better understanding on the model accuracy. For a single phase system, this assumption was not restricted to the anode only and will allow the accuracy of the model to be extended to the cathode side. The model results were validated using experimental data obtained from the University of Cape Town (UCT) HySA/Catalysis fuel cell laboratory under the same operating conditions as the model.

The results of the normalised 3-D model concentration profiles for hydrogen at the anode showed that, in contrast with several papers in the literature, concentration through the GDL and catalyst layer in x- and y-axis were significant. This was proved when considering the concentration of hydrogen in the anode catalyst layer along the x-axis which showed a much more significant decrease in concentration due to reactant consumption than along the z-axis which showed a negligible change in concentration gradient from the GDL to the catalyst layer. It was also shown that the assumption that the major concentration gradient in the channels is along the channel holds true as the concentration

gradient in the axis perpendicular to the channel (y- and z-axis) were found to be very low. When comparing the results of the 1-D and 3-D model concentration profiles, it was noted that both models predict the same final concentration at the catalyst layer which brought up a flaw in the use of polarization curves to validate and compare different fuel cell models as the predicted polarization curves are independent of the concentration profile through the cell. However, because the intermediate concentrations in the two models differ, the 1-D model cannot be fully trusted and therefore alternatives must be developed to account for transport along the channel (x-axis) as well as perpendicular to the membrane (z-axis). Finally, when comparing the simulation time of the two models, the estimated simulation time for the 3-D model was 10-20 minutes depending on processor power while the 1-D model took less than one minute to run. This provides a 95% time saved when the 1-D model is used instead of the 3-D model.

In conclusion, while a 1-D model does not predict exactly the same results as that of the 3-D model, for a single phase system, it can be used for practical applications, most notably the study of cell performance by variation of different operating and physical parameters in a cost-effective manner. The 1-D model can be further built upon to account for transport along the channel (x-axis) as well as perpendicular to the membrane (z-axis). Such a model is known as a 1-D + 1-D model. This model will allow a more accurate representation of the transport phenomena within a PEMFC during operation and will be more comparable to a 3-D model.

TABLE OF CONTENTS

LIST OF TABLES

LIST OF FIGURES

Main Text

Appendices

LIST OF ACRONYMS

1-D	One-Dimensional
2-D	Two-Dimensional
3-D	Three-Dimensional
AFC	Alkaline Fuel Cells
CFD	Computational Fluid Dynamics
DMFC	Direct Methanol Fuel Cell
FC	Fuel Cell
GDL	Gas Diffusion Layer
HOR	Hydrogen Oxidation Reaction
MEA	Membrane Electrode Assembly
MFC	Microbial Fuel Cells
MCFC	Molten Carbonate Fuels Cells
MFM	Multi-Fluid Model
MM	Multi-component Mixture
MMM	Multi-component Mixture Model
NVS	Navier-Stokes
OCV	Open Circuit Voltage
ORR	Oxygen Reduction Reaction
PAFC	Phosphoric Acid Fuel Cells
PEM	Proton Exchange Membrane
PEMFC	Proton Exchange Membrane Fuel Cell
PFSA	Perfluoro-Sulfonic Acid
PSEPVE	Perfluoro-Sulfonylfluoride Ethyl-Propyl-Vinyl Ether
PTFE	Poly(Tetrafluoroethylene)

SOFC	Solid Oxide Fuel Cells
UDF	User Defined Function
UFT	Unsaturated Flow Theory
UCT	University of Cape Town

NOMENCLATURE

a	Water activity	
$A_{Channel}$	Channel cross-sectional area	[m^2]
A_{MEA}	MEA surface area	[m^2]
C_j	Concentration of species *j*	[$kmol/m^3$]
D_j	Diffusion coefficient of species *j*	[m^2/s]
dC_j	Change in species concentration	[s]
dt	Change in time	[s]
dz	Change in distance in z-direction	[m]
E_{OCV}	Nernst potential at OCV	[V]
F	Faradays constant	[C/mol]
g	Acceleration due to gravity	[m^2/sec]
ΔG_{rxn}	Gibbs free energy of reaction (reduction or oxidation)	[J/mol]
Gr	Grashoff number	
h_i	Mass transfer coefficient through zone *i*	[m/sec]
i	Local current density	[A/cm^2]
i_L	Limiting current density	[A/cm^2]
i_0	Exchange current density	[A/cm^2]
$K_{GDL/cat\ layer}$	Permeability through GDL and catalyst layer	[m^2]
$k_{membrane}$	Membrane conductivity	[S/m]
L	Characteristic length	[m]

M_j	Molar Mass of species *j*	[kg/kmol]
n_d	Electro-osmotic drag coefficient	
n	Number of electrons taking part in reaction	
N	Total number of species	
N_j	Molar flux of species *j*	[kmol/m^2.sec]
P_j	Partial Pressure of species *j*	[Pa]
$P_{sat}(T)$	Saturation pressure of species *j* at given *T*	[Pa]
P_{cell}	Total cell pressure	[Pa]
Q	Volumetric flowrate	[m^3/sec]
R	Universal gas constant	[J/moj.K]
Ra	Rayleigh number	
$R_{Electron/\,proton}$	Resistance due to electron and proton transfer	[Ω]
Sh	Sherwood number	
Sc	Schmidt number	
$S_{H_2/O_2/H_2O}$	Source terms for hydrogen, oxygen and water	[kg/m^3.sec]
S_{mom}	Source terms for momentum	[N/m^3]
T	Temperature	[K]
t	Time	[sec]
$t_{GDL/membrane}$	Thickness of membrane and GDL	[m]
u_j	Velocity of species *j*	[m/s]
x_j	Mass fraction of species *j*	

y_j	Mole fraction of species *j*	

GREEK LETTERS

α	Transfer coefficient at either anode or cathode	
δ	Change in variable (distance, concentration, etc.)	
ε	porosity of GDL or catalyst layer	
ϕ	electric potential	[V]
γ	activity coefficient	
η_{act}	Voltage losses due to activation polarization	[V]
$\eta_{concentration}$	Voltage losses due to concentration polarization	[V]
η_{ohmic}	Voltage losses due to ohmic polarization	[V]
μ	dynamic viscosity	[kg/m.sec]
ν	kinematic viscosity	[m^2/sec]
ρ	mass density	[kg/m^3]
τ_{ii}	Viscous stress	[Pa]
τ_{ij}	Total normal stress	[Pa]
ζ	Stoichiometric coefficient for either anode or cathode	

SUBSCRIPTS

act	Activation
j	Species
ref	Reference value
x,y,z	x-, y- or z-axis

Pro	Protons
Elec	Electrons
L	Limiting
a	Anode
c	Cathode

ACKNOWLEDGEMENTS

This research could have not been completed without the assistance of several people and organisations, before commencing with the overview of the research, I would like to take this opportunity to thank these people and organisations in full.

Firstly I would like to thank my sponsors, HySA/Catalysis, for their financial support which played a big role towards the completion of my MSc. In any project, a mentor or supervisor is key in order to be successful, I was fortunate in my research activities to not have one supervisor but two in A/Prof. Randhir Rawatlal (who acted as my primary supervisor) and Dr. Olaf Conrad (who acted as my co-supervisor). Both had continuous open door policies throughout the course of my research and were always willing to assist in any way they could.

With that in mind, a special thanks to Dr. Conrad for persuading A/Prof. Torsten Berning from Aalborg University to have his sabbatical at UCT. His extensive knowledge in the field of fuel cell modelling and water management was invaluable while his assistance in understanding the procedure for designing the 3-D model was vital in its completion.

The Members of HySA/Catalysis at UCT cannot be overlooked. Nabeel Hussain, Dr. Pieter Levecque, Dr. Shiro Tanaka and Dr. Sharon Blair all deserve recognition for their input during our weekly journal club meetings as well as the constant reviewing and editing of the material presented in this document.

I would also like to thank Dr. Waldo Coetzee and Dr. Harish Appa for providing assistance in understanding CFD mathematics as well as some of the more intricate details of the CFD solver *FLUENT* and the geometry editor *GAMBIT* that were used to develop and simulate the 3-D model.

My family have been a continued source of support, not only in the last two years, but throughout my life and I would like to thank them from the bottom of my heart.

Finally a special mention to the late Kevin Japp, words cannot express the sadness towards your untimely passing. Your friendship and support as a colleague will always be treasured.

1. FUEL CELL TECHNOLOGY

Approximately 33% of the world's primary energy consumption is related to oil. Of this 33%, approximately 70% is used in the transportation sector (IEA, 2011). Even though the earth's oil reserves are a finite resource, the global rate of consumption is expected to rise exponentially while the production rate is expected to peak in the coming years. The imbalance between consumption and production has led to severe market price fluctuations as well as political instability between oil rich nations in the Middle East and the rest of the world. Beside the finite quantity of this fossil fuel, a more immediate concern is the increasing effect of global warming caused by the accumulation of carbon dioxide released during fossil fuel combustion.

Therefore the restructure of the energy policy towards the usage of renewable and "clean" sources is of significant importance. Hydrogen has been studied intensively as a potential energy carrier as it can be produced using electrolysis or methane gas reforming and allows for a carbon dioxide free environment as hydrogen oxidation produces pure water as the only by-product.

Fuel cell technology has been studied in detail to implement hydrogen as well as other renewable sources as a feasible fuel with the Polymer electrolyte membrane (PEMFC) fuel cell being of particular interest to the automotive industry due to the low start-up times of this type of FC as well as the relatively small size allowing for mobile usage. Modelling plays a significant role in the development of fuel cell technology as it allows for new designs to be tested and improved upon in a cost effective manner. However, complex models are associated with large simulation times which can be a hindrance when simple quick solutions are required.

With this in mind, the present study focuses on the development of a one-dimensional (1-D) (directional axis perpendicular to the membrane) and three-dimensional (3-D) steady state isothermal mathematical PEMFC models by using first principles. Both models will be used to simulate the transport of reactant species through the various layers of the cell at the anode side. The results obtained will be compared to investigate the accuracy of the simple 1-D model in comparison with the more complex 3-D model. The broader aim of this research is to develop the fundamentals of PEMFC modelling in order to create a foundation for HySA/Catalysis.

Fuel cells (FCs) are electrochemical devices that convert the chemical energy in fuels directly into electrical energy in the presence of specific catalysts. FCs can be classified into six main categories (Pollet, 2010), namely, proton exchange membrane fuels cells (PEMFCs), alkaline fuel cells (AFCs), phosphoric acid fuel cells (PAFCs), molten carbonate fuels cells (MCFCs), solid oxide fuel cells (SOFCs) and microbial fuel cells (MFCs). These categories are characterised by the raw materials used as well as electrode composition and structure and operating temperature of the cell.

The following study focuses only on hydrogen powered FCs, more specifically PEMFCs which are characterised by an acidic electrolyte membrane, low operating temperatures (60-80 °C) and a compact structural design. Therefore, further investigation and discussion will be based on the above FC type.

1.1. Proton Exchange Membrane Fuel Cells – A Component Analysis

As stated above, the key feature that differentiates a PEMFC from other FCs is that it makes use of proton conductive polymer membrane as an electrolyte; the membrane is impermeable to gases and electrons but conducts protons (Barbir, 2005).

The general structure of a PEMFC consists of an outer gas channel layer (flow-field plate), where the hydrogen (fuel) and oxygen (oxidant) flow, separately on either side. The next layer, made of graphitic cloth or paper, is the gas diffusion layer (GDL). The GDL is used to disperse the gases over the inner layers (catalyst layer and the proton exchange membrane (PEM)) by allowing the gases to diffuse through the material layers of the GDL. The layers following the GDL are the micro-porous and active catalyst layers; the latter is typically made up of platinum supported on graphitic carbon particles (Barbir, 2005; Wang et al., 2010). The two electrodes (anode and cathode) of the FC are made up of the GDL and the catalyst layer. The anode is on the fuel side, while the cathode is on the oxidant side, the following reactions occur on the electrodes:

Anode reaction: $2H_2 \xrightarrow{Pt} 4H^+ + 4e^-$ *Reaction 1*

Cathode reaction: $O_2 + 4H^+ + 4e^- \xrightarrow{Pt} 2H_2O$ *Reaction 2*

These electrodes are separated from one another using the PEM; the PEM inhibits electron transfer while aiding proton conductivity. The two electrodes together with the PEM form the membrane electrode assembly (MEA). The MEA is then framed by the bipolar plates. The basic design of a typical PEMFC is illustrated in Figure 1.

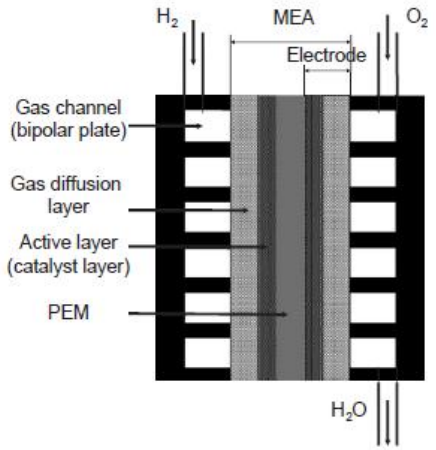

Figure 1: Illustration of a hydrogen powered PEMFC (Caillard et al., 2005)

The PEMFC components that were briefly discussed above are now further discussed in order to try and gain a deeper insight into their design.

1.1.1. The Proton Exchange Membrane

The PEM that is used in a PEMFC must have several qualities in order to allow for effective FC operation. The PEM must have high proton conductivity while preventing electron transport and gas crossover and it must be mechanically and chemically stable in both ambient and FC operating conditions.

The membranes for PEM fuel cells are normally made of perfluorocarbon-sulfonic acid ionomer, which is a copolymer of poly(tetrafluorethylene) (PTFE) (Barbir, 2005). The best known commercial membrane is produced by DuPont and is traded under the trademark Nafion^{TM}; it uses perfluoro-sulfonylfluoride ethyl-propyl-vinyl ether (PSEPVE) (Barbir, 2005; Mehta & Cooper, 2003). Nafion^{TM} is an example of a perfluoro-sulfonic acid (PFSA) membrane. A typical chemical structure of Nafion^{TM} is illustrated in Figure 2. PSFA membranes have two advantages in the context of FCs, the first is that they are chemically stable in oxidative and reductive environments due to the PTFE backbone, the second is that due to the sulfonic acid (SO_3H) functional groups, a high proton conductivity can be obtained in a well hydrated PFSA membrane (Mehta & Cooper, 2003; Wang et al., 2010).

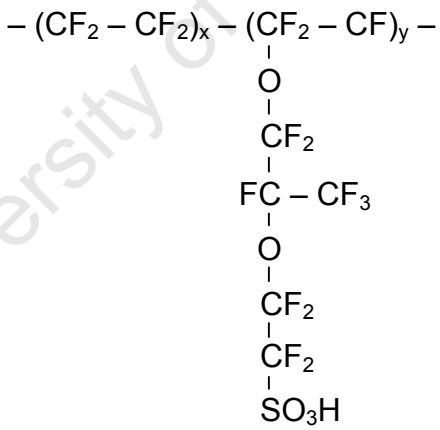

Figure 2: Chemical Structure of Nafion^{TM} (Barbir, 2005)

Proton transport through the membrane is largely dependent on the membrane water content. There are two mechanisms for proton transport (Wang et al., 2010), the first being proposed by Kreuer et al. (1982) is called “vehicular” diffusion which is dependent on the water diffusivity in the membrane. In this mechanism, protons attach to water molecules to create hydronium ions (H_3O^+), thereby creating a proton concentration gradient. This gradient causes the diffusion of protons from regions of high concentration to those of low concentration (Kreuer et al., 1982). The second mechanism is one where the side chains of the sulfonic groups are connected due to a high water content in the membrane, this allows for the direct migration of protons by “hopping” through each site (Kornyshev et al., 2003). The water content in a PEM can be expressed in two ways; the first

is grams water per gram dry polymer while the second method expresses the water content in the membrane, λ, as a function of the water molecules per sulfonic acid groups present in the polymer.

A well hydrated membrane is of critical importance in achieving good proton conduction for the above reasons. However, due to the porous structure of the membrane, gases permeate through (solubility and diffusivity). A thick membrane will reduce the permeability effect; however, dehydration of the membrane could occur on the anode side if the membrane is too thick at higher current densities. This is due to water being transferred to the cathode side through electro-osmotic drag. A thinner membrane will counteract the effect of electro-osmotic drag through back-diffusion of product water formed at the cathode (Barbir, 2006); however the gas permeability through the membrane will increase. Therefore, a compromise is required when designing the PEM.

1.1.2. The Catalyst Layer

A result of the low operating temperatures of a PEMFC (60-80 °C) is a slow reaction rate; this is especially true for the oxygen reduction reaction (ORR) at the cathode side. Therefore to improve the reaction rate (by reducing the activation barrier), the reactions have to be catalysed. Catalysed carbon particles along with a certain amount of ionomer are applied as an ink onto the porous, electrically conductive substrate (GDL) or the membrane. The ionomer allows the catalyst particles to be in ionic contact throughout the layer and is applied to ensure that the hydrogen protons can migrate from the anode catalyst layer towards the cathode layer. The surface area of the catalyst layer is an important factor and therefore, in preparing the layer, one must use small catalyst particles finely dispersed over the catalyst support surface (Barbir, 2006). The common catalyst supports are carbon powders with a high mesoporous area.

Although the catalyst layer is the thinnest layer in the cell (5-30 μm thick), it is the most complicated layer consisting of a three- phase composite made up of interconnected networks (catalysed carbon, the electrolyte phase and the void space) to allow for proton, electron and reactant transport respectively (Mukherjee & Wang, 2007).

Platinum has been found to be the only economically viable catalyst (Verbrugge, 1994), with slight platinum-alloy composition variations such as Pt-Co and Pt-Ni being used in many situations, especially on the cathode side (Caillard et al., 2005).

1.1.3. The Gas Diffusion Layer

The GDL is a vital component of the PEMFC, playing multiple roles during operation. Key among which are the through plane flow induced by electrochemical reaction, heat transfer, electron transport and two-phase water transport (Dutta et al., 2000; Nam & Kaviany, 2003; Wang et al., 2010). The most common material of construction for the GDL is porous carbon fibre. If the fibres are woven together, the material is called carbon cloth, however if they are bonded together by

resins, the resulting material is called carbon paper (Wang et al., 2010). The GDL is normally designed to aid in liquid water removal. This is done by designing the GDL to be hydrophobic, to do this; PTFE is incorporated into the GDL structure to modify its wettability (Benziger et al., 2005; Wang et al., 2010).

1.1.4. The Bipolar Plates

The gas flow channels that supply reactant gases and remove by-product water are housed in the bipolar plates of a PEMFC. The gas flow channels are machined into the bipolar plates and have typical cross-sectional dimensions of 1 mm (Wang et al., 2010). Besides housing the flow channels, bipolar plates provide mechanical support for the MEA as well as aid in the providing a conductive passage for the transport of electrons as well as heat. The electrical conductivity between the bipolar plates and GDL is of key importance so as to minimize the ohmic losses (cf. 1.2.3).

In fuel cell stacks, they also separate cells from one another; one plate normally contacts the cathode of one cell on one side and the anode of another cell on the other side. The common material of construction used to manufacture bipolar plates is stainless steel or graphite.

1.2. PEMFC Performance and Loss Mechanisms

1.2.1. The Theoretical Potential

The theoretical potential of a PEMFC is determined from the Nernst equation is predicted when no current is being drawn, this type of PEMFC operation falls under open circuit (equilibrium) conditions and the potential obtained is called open circuit voltage (OCV). However, in practice, the OCV obtained is much lower than that predicted by the Nernst equation and when an external load is applied, the potential drop from the predicted potential is even greater (Barbir, 2005). The losses in potential can be classified into three main types, namely, activation, ohmic and concentration losses, a fourth less significant loss type known as crossover and internal current losses also occurs during cell operation. Figure 3 illustrates a typical polarization curve showing the additive losses (defined by the term “actual polarization curve” on the figure) as well as the domains of each individual loss stated above.

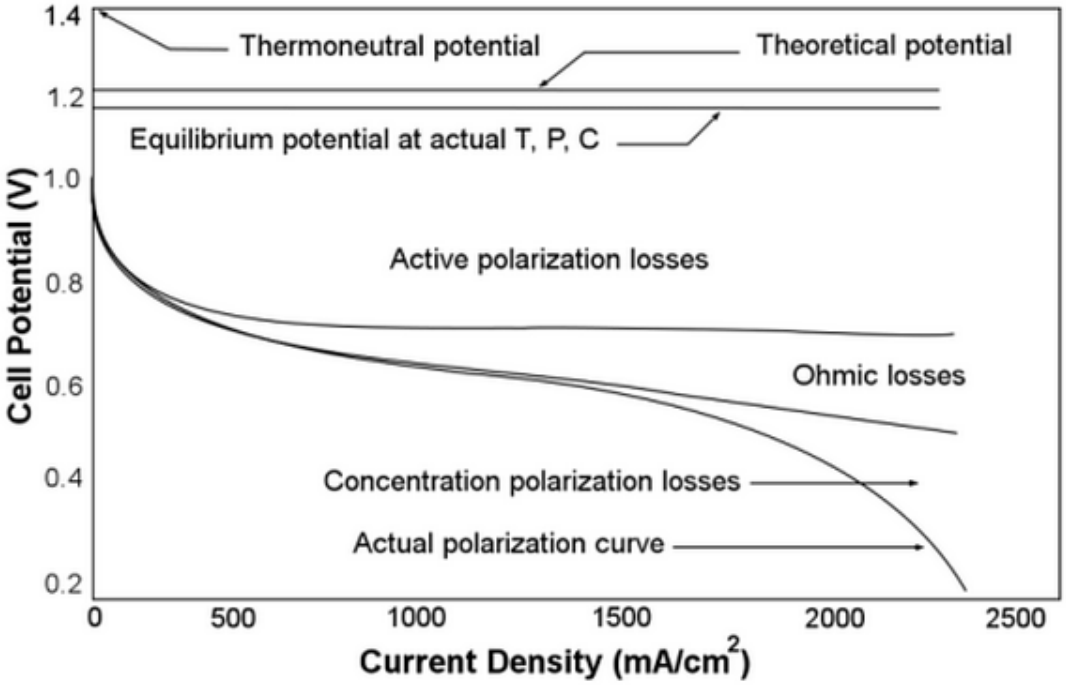

Figure 3: Potential-Current curve (polarization curve) illustrating the additive losses as well as the three loss domains (Yuan et al., 2010)

The cell losses stated above are now further discussed.

1.2.2. Activation Losses

As stated earlier (section 1.1.2), the reaction rate (especially at the cathode) in low temperature PEMFCs is slow and during operation at low current density, the voltage overpotential required to overcome the energy barrier for the electrochemical reaction to occur is known as the activation polarization. The catalyst reduces the overall energy barrier but due to the slow oxygen reaction kinetics at the cathode, the voltage loss remains (Spiegel, 2008). The activation overpotential of the ORR is much larger in magnitude than that of the hydrogen oxidation reaction (HOR) and so the anode activation overpotential can be neglected (Barbir, 2005).

1.2.3. Ohmic Losses

Ohmic losses are experienced due to charge transfer resistance in the PEMFC during operation. Every material has an intrinsic resistance to charge flow and therefore all the components that make up a PEMFC contribute to the voltage losses due to ohmic resistance (Srinivasan, 2006). The ohmic resistance is made up of the electronic resistance and the ionic resistance. The ionic resistance is created due to the electrolyte while the electronic resistance consists of the total electrical resistance of all the other conductive components that make up the PEMFC (Barbir, 2005; Spiegel, 2008). The ionic resistance is much greater than the electronic resistance as ionic transport is more difficult than electronic transport (Spiegel, 2008) and therefore the electronic resistance is neglected. The potential drop varies linearly across the resistance (as seen in Figure 3) with the amount of current passing through it (Srinivasan, 2006).

1.2.4. Concentration Losses

The third type of voltage loss is caused due to the depletion of reactants. At high operating current densities, the reaction rate is larger than the rate of mass transfer and therefore the reactant species is depleted leading to a performance drop in the cell. This type of voltage loss is defined as concentration losses. At the point where concentration at the reactant surface drops to zero (i.e. rate of reaction equals the rate of diffusion of reactant species to the active sites), the achievable current density is known as the limiting current density (i_L).

1.2.5. Crossover and Internal Current Losses

The final type of loss that occurs during cell operating is caused by hydrogen fuel crossover, whereby hydrogen diffuses through the membrane and reacts with oxygen without doing any "useful work", some electrons also pass through the membrane causing an electronic short, the electronic short causes an internal current (few mA) which in turn causes an overall loss of current in the cell (Zhang, 2008). The reaction between the permeated hydrogen and oxygen causes the cathode to become "depolarized" leading to a drop in the cathode potential and therefore an overall drop in the cell potential (Barbir, 2005).

During normal cell operating conditions, these losses are insignificant as the rate of hydrogen permeation is several orders of magnitude lower than the rate of hydrogen consumption at the anode; this is because the hydrogen concentration is depleted during operation hence reducing the driving force for permeation through the membrane (Barbir, 2005). However, at low current operation or at OCV conditions these losses do contribute significantly as a source of current inefficiency.

1.3. Fuel Cell Technology – Closing Remarks

FC technology is a large research field with multiple areas of study including more efficient catalyst utilization, cell diagnostics, water management as well as membrane and GDL design. More effective designs can be aided by modelling the various components and simulating performance. A detailed understanding of the complex interactions between mass transport, reaction and rate kinetics is also required to better understand more intricate concepts such as loss mechanisms and water management, this can be achieved by the development of FC models to simulate performance at various operating conditions and investigate phenomena difficult to measure experimentally (such as mass transport in the cell).

2. LITERATURE REVIEW – FUEL CELL MODELLING

FCs are still not economical and the state space for the design variables needs to be explored rigorously. This is time-consuming and expensive to do only experimentally, and building a model would help reduce that time and expense as multiple variables can be studied (depending on the detail of the model developed).

2.1. What is a Fuel Cell Model

A FC model uses either empirical or mathematical equations in order to model the behaviour of a desired FC system. In the case of the mathematical equations, FC models can be classified into one of three categories, namely analytical, semi-empirical or mechanistic (Cheddie & Munroe, 2005; Siegel, 2008). The type of model used depends on the focus of study which in turn is often dependent upon on the system boundaries that define the area of interest.

2.1.1. Analytical Models

While all the fundamental processes that occur within a PEMFC (mass, energy, momentum and species transport) are normally considered to be complex areas of study that can be expressed mathematically using the conservation laws, these equations can often be reduced to create a simple mathematical model depending on the required level of complexity of the system of interest (Das, 2010). An analytical model is one where many simplified assumptions are made when concerning the variables in the cell (Standaert et al., 1996).

One of the first analytical fuel cell models was developed by Standaert et al. (1996) and focused on the development of a voltage-current relationship for cell operation under isothermal conditions. The developed model relationship was only accurate when the fuel utilization was high, however, Kulikovsky (2002) developed a more accurate model for the above relationship by accounting for the limiting cases of both large and small currents and fitting the data obtained in an equation based on exact mathematical formulas to obtain a polarization voltage-current relationship that agreed quite well with experimental data.

While these models do give an initial understanding of the system (prediction of the voltage losses and water management requirements), they are approximate and therefore accurate insight into the transport processes that take place within the cell cannot be obtained (Cheddie & Munroe, 2005). Analytical models are useful for simple systems when quick calculations are required.

2.1.2. Semi-empirical and Empirical Models

Semi-empirical models combine theoretical differential and algebraic equations with empirical data or relationships. This type of model is useful when the physical phenomena of the system cannot be modelled and when the governing theories are not well understood. There are several advantages to using a semi-empirical approach including readily available, semi-validated

experimentally determined parameters for a set range of operating conditions (Haraldsson & Wipke, 2004). However, because a semi-empirical relationship is developed for a specific set of operating conditions, the obtained data acquired from these relationships is often only valid over a narrow range of fuel cell performance (Cheddie & Munroe, 2005) leading to a lack of accuracy of the model (i.e. they only correlate the output with the input).

To account for this, several attempts have been made to model fuel cell performance by the development of empirical models to predict polarization curves by using experimentally obtainable cell parameters such as temperature (Parthasarathy et al., 1992) with temperature dependent empirical relationships being developed for exchange current densities and charge transfer coefficients.

2.1.3. Mechanistic Models

Mechanistic models are the most accurate of the three types of FC models. In mechanistic modelling differential and algebraic equations are derived based on the physics and electrochemistry that govern the performance of the cell (Das, 2010). These equations are then solved using computational techniques. Two types of mechanistic models exist, single domain and multi-domain models. Further discussion of these models is carried out in sections 2.1.3.1 and 2.1.3.2.

2.1.3.1. Single Domain Models

The single domain approach combines all the regions of interest into one domain. The equations for mass, momentum and energy are defined over the entire domain and the differences in each region are accounted for by source and sink terms (Cheddie & Munroe, 2005). All the equations are written in a generic convection-diffusion form; the effect on the computational solver is that no internal boundary conditions need to be defined and the solution can be obtained using known computation fluid dynamics (CFD) methods.

2.1.3.2. Multi-domain Models

Separate sets of equations for each of the different layers in the FC (the anode/cathode GDLs, the anode/cathode flow channels, the membrane and the catalyst layers) are developed and solved separately and simultaneously when employing a multi-domain mechanistic modelling approach (Cheddie & Munroe, 2005).

Table 1: Different aspects of FC modelling and model type required for each aspect (modified from Cheddie & Munroe, 2005)

	Model type	Analytical	Semi-empirical	Mechanistic
Polarization		√	√	√
Transport Phenomena				√
Thermal effects				√
Water Management				√
Concentration effects			√	√
CO kinetics			√	√
Catalyst utilisation				√
Flow Field Effects				√
Membrane Conductivity			√	
FC stacks			√	√

Table 1 shows the different aspects of FC modelling that have been studied using modelling, the required models to test each aspect are also shown. The only aspect studied extensively using analytical modelling are the voltage losses due to polarization within the FC (discussed in section 1.2), this is because while analytical models are effective at predicting performance of a typical PEMFC, they are unable to model the more complex phenomena such as transport and thermal effects. It must be noted that the effect of two-phase water on cell performance has been investigated by Loo et al. (2011) using an analytical model. The model predicts cell performance during normal (single phase) as well as flooding conditions (two-phase) and drastically reduces the computational time required to solve the model (Loo et al., 2011).

While most of the aspects have been investigated using a Mechanistic approach, it must be noted that most of the studies conducted focused on the polarization, transport phenomena and flow field effects (Cheddie & Munroe, 2005). Past models focused on the cathode side of the PEMFC, the reason for this is that the largest source of inefficiency in FC performance is due to the cathode activation overpotential (voltage losses due to the catalyst layers) (Siegel et al., 2003). The key equations used to model the above aspects are the Nernst-Planck equation for species transport (derivation in Appendix A.2), the Butler-Volmer equation to model the electrochemical behaviour of the cell as well as performance (derivation in Appendix A.2), the Maxwell-Stefan equations or Fick's law for gaseous species transport (discussed in section 2.2) and Darcy's equation for liquid water transport as well as transport through porous media (Bernardi & Verbrugge, 1991).

While many models have been developed using each of the approaches outlined above, a comparison of different approaches is rarely done and therefore this is one area of potential improvement in the study of FC modelling.

2.2. Gaseous Species Transport in Diffusion Media in a PEMFC

The gaseous species present in the GDL of a PEMFC are typically hydrogen and water vapour on the anode side and oxygen, nitrogen, and water vapour on the cathode side. The more complex process to model mathematically is the cathode transport due to the production of water as well as the higher number of species present.

The two methods used to model gaseous species diffusion are Fick's Law and multi-component Maxwell-Stefan equations. The two methods are discussed below.

$$N_j = -D_j\left(\frac{\delta C_j}{\delta z}\right) \tag{2.1}$$

(2.1) describes Fick's Law of diffusion. The symbol N_j refers to the molecular diffusive flux per unit area of component *j*, C_j refers to the concentration of component *j*, and D_j refers to the diffusivity of component *j* and *z* refers to the direction of the concentration gradient.

The concentration of component *j* in a binary system is directly proportional to the negative of the concentration gradient of component *j* whereas in multi-component diffusion, other types of diffusion may be observed. Therefore the Maxwell-Stefan equations are a more comprehensive relationship for diffusion in multicomponent flows having both bulk and diffusive fluxes (Bird et al., 2002). The Maxwell-Stefan equation is valid for any number of species and allows for interaction among the species rather than assuming each species only interacts with the primary substance in the mixture.

$$\nabla x_j = \sum_{i=1}^{N} \frac{y_j y_i\left(\vec{u_j} - \vec{u_i}\right)}{D_{ji}} \tag{2.2}$$

(2.2) shows the generalised Maxwell-Stefan equation, where N is the number of species in the system, y_i and y_j are the mole fractions of species *i* and *j* respectively, D_{ji} is the binary diffusion coefficient and $\vec{u_i}$ and $\vec{u_j}$ are the velocity vectors of species *i* and *j* respectively (Taylor & Krishna, 1993).

When convection is present along with migration (with respect to ions), equation 1 is extended to create the Nernst-Planck equation (Bard & Faulkner, 2001). While Bird (2002) states that the Maxwell-Stefan equation is more comprehensive than Fick's Law for a multicomponent mixture, for a PEMFC, it has been found that both equations lead to approximately the same solution provided the appropriate diffusion coefficient is used (Kulikovsky, 2003; Suh & Park, 2011).

2.3. Developments in PEMFC Modelling

As shown in Table 1, a PEMFC has several processes that occur within it during operation; however, three key processes have the greatest impact on its performance. These processes are the electro-chemical reactions in the catalyst layers, proton migration in the PEM layer (membrane conductivity) and the mass transport through all the layers of the PEMFC (Baschuk & Li, 2004). These processes can be modelled using the mathematical techniques discussed in section 2.1. The accuracy of the model depends on the simplicity of the assumptions made in developing them.

While many models have been developed to account for the three aspects above, they have been developed based on the following models and therefore use similar assumptions, equations and solving tools.

2.3.1. Catalyst Utilisation

The earliest mechanistic approach to PEMFC modelling was conducted by Bernardi & Verbrugge (1991). The model developed was a 1-D, steady state and isothermal and was used to describe the reactant gases and product water transport and ohmic and activation overpotentials (Bernardi & Verbrugge, 1991; Dinçer & Rosen, 2007). The main assumptions made in developing the model was a fully hydrated membrane as well as constant water content in the membrane, therefore the water calculations (input and removal requirements) were done based on this assumption (i.e. the water transport was governed by electro-osmotic drag) (Bernardi & Verbrugge, 1991). This model provided valuable information about the physics of the electrochemical reactions and transport phenomena in these regions of the PEMFC.

2.3.2. Membrane Conductivity

Verbrugge and Hill (1990) were one of the first to investigate proton conductivity in a fully hydrated membrane, however, since the cathodic reactions produce water, the water content of the membrane is not constant and since proton migration is strongly coupled with water transport in the FC, due to the polymer electrolyte being permeable to water (Baschuk & Li, 2004) a more accurate model was needed.

To determine the relationship between the PEMFC performance and membrane hydration, Springer et al. (1991) developed a semi-empirical model that assumed a partially hydrated membrane and empirically determined the relationship between membrane conductivity and electrode porosity with water content assuming that the membrane used was Nafion^{TM} (Springer et al., 1991). They developed a steady state, isothermal 1-D model that was used to describe the water transport within the membrane as well as membrane conductivity. This model was the first to account for a partially dehumidified membrane. To account for partial dehumidification, the water content within the membrane was experimentally determined and a correlation was developed between the membrane conductivity and water content of the membrane. The model also

considered water transport through electro-osmotic drag and diffusion, however due to the model being 1-D; pressure driven water transport was neglected (Baschuk & Li, 2004).

Several models have been developed that assume a constant value for the membrane conductivity rather than applying the empirical relationship developed by Springer et al. (1991). Two such models were developed by Liu et al. (2006) and Al-Baghdadi and Al-Janabi (2007). Liu et. al (2006) studied mass transfer limitations at varying current densities while Al-Baghdadi and Al-Janabi (2007) investigated fuel cell performance at various cell operating conditions.

2.3.3. Mass Transport Phenomena

Gurau et al. (1998) developed a two-dimensional (2-D) model for a PEMFC to determine the species concentrations within the cell. The effect of temperature, air flow rates and porosity of the GDL on PEMFC performance was also tested. The reactant flow was modelled through the gas flow channels, GDL, catalyst layer and membrane, therefore the approach used was a multi-domain mechanistic approach.

The major assumptions made in the development of the model were perfect and incompressible gas mixtures, negligible liquid water in the gas flow channels, laminar flow through the cell and steady state conditions (Gurau et al., 1998).

Um et al. (2000) advanced on the work carried out by Gurau et al. (1998) by developing a model that simulated transient operation in the FC. The model developed was 2-D and made similar assumptions to Gurau et al. (1998) with the modelling unsteady state operation. Unlike Gurau et al. (1998), a single domain approach was adopted in developing the model (Um et al., 2000; Cheddie & Munroe, 2005). The model investigated the effect of hydrogen dilution along the anode gas flow channel and found that mass transport limitations are present on the anode side during high current densities due to an increase in the rate of hydrogen consumption (Um et al., 2000).

Lum and McGuirk (2005) developed a 3-D steady state, single phase PEMFC model to investigate mass transport phenomena at different current densities validating the results with experimental data obtained from Shimpalee et al. (1999). The results showed good agreement with the experimental data for low and intermediate current densities. This model was developed further by Dawes et al. (2009) to account for liquid water formation and flooding effects (this model is discussed in section 2.4.3).

Suh and Park (2011) also developed a model to investigate the transport phenomena in a PEMFC as well as the overpotential distribution in the MEA. The model was a steady state, 1-D non-isothermal system that included two-phase flow. Other assumptions in developing the model include negligible pressure drop in the GDL leading to reactant gas transport being a diffusion driven process and liquid water being removal is achieved by the capillary effect (Suh & Park,

2011). It was found that at high current densities (low output voltages), the assumption of negligible anode activation overpotential (see section 1.2.2) was inaccurate as the ratio of cathode to anode activation overpotentials were approximately equal.

Channel design has also been investigated using modelling to study its effects on mass transport and overall performance improvement. Examples of such research include that conducted by Peng and Lee (2006) where a single phase high temperature non-isothermal PEMFC model was developed in order to optimise the channel width and equivalent land area of the gas flow channels. Another recent study by Hashemi et al. (2012) investigated the performance differences obtained when using straight rather than serpentine channels.

All the models discussed above were developed around single phase flow where liquid water formation and transport was not considered. However, two phase flow has been an important area of study in PEMFC modelling and is therefore discussed in the following sections even though this specific study does not investigate two phase flow phenomena.

2.4. Two-Phase Flow and Water Management

While numerous models to simulate PEMFC operation have been developed and many key aspects of the PEMFC design have been aided by these models, most of the models were built around the assumption of single phase flow whereby all the species inside the PEMFC are gaseous. While some models do focus on water transport phenomena, water vapour and liquid were considered two different species with condensation and evaporation rates having no effect on the flow (van Bussel et al., 1998; Okada et al., 1998; Chen et al., 2004).

The research into two-phase water formation and transport is ever growing as water management is critical in achieving high performance in PEMFCs (Wang et al., 2001). Two-phase water models can assist fuel cell manufacture by improving membrane and GDL designs.

2.4.1. What is Two-Phase Flow?

During PEMFC operation, the reduction of oxygen at the cathode side of the cell produces water, at low current densities, the water produced exists as vapour, however, as current densities increase (water formation rate increases), the water produced begins to condense due to a high accumulation rate (water is produced faster than it can be transported out) (Wang et al., 2001; Koido et al., 2008). Wang et al. (2001) found that the threshold current density whereby condensation of product water occurs is 1.35 A/cm^2 however, it should be noted that this value is based on specific model parameters used by Wang et al. (2001).

2.4.2. Why is Water Management Important?

The amount of water within each region of the PEMFC is directly proportional to the overall performance of the cell, the efficiency and the durability (McCain et al., 2010). Some of the effects

of two-phase water on performance of the PEMFC are flooding, gas dilution and membrane dehydration (Koido et al., 2008). To achieve a high ionic conductivity, the PEM requires sufficient water (Wang et al., 2010); however, an excess amount of liquid water in the cathode catalyst layer has been experimentally proven to be the cause of output voltage degradation (McCain et al., 2010).

The liquid-gas two-phase flow in the GDL is one of the many issues in water management in a PEMFC as it affects the amount of water in the catalyst layer and membrane, the reactant transport from the gas channels to the catalyst layer is also affected (Koido et al., 2008; McCain et al., 2010). Liquid water that exits the GDL on either side of the PEMFC accumulates in the gas flow channel and impedes the flow of reactants to the GDL and membrane therefore reducing the performance of the cell by decreasing the cell voltage. In modelling, two phase flow is important as it allows for a more accurate simulation of high current density operation as it provides a better representation of the mass transport limitations caused by liquid water (Dawes et al., 2009).

2.4.3. Modelling Two-Phase Flow

When modelling two-phase flow in the GDL, the major concern is accurately simulating the pore blockage by liquid water commonly referred to as saturation. The movement of liquid water in the GDL depends on the local liquid pressure as well as the gas pressure and the characteristics of the GDL (porosity, tortuosity etc.). The capillary pressure is defined as the pressure difference between the vapour and liquid phase (Dullien, 1979). The liquid transport is highly dependent on the saturation and capillary pressure. Assuming laminar flow, Darcy's law can be modified to account for flows driven by saturation gradients.

Two-phase flow can be modelled in one of two ways. The first method is called the multicomponent mixture (MM) model (MMM); this method makes use of a single conservation equation to define the entire system (liquid and vapour). The interaction of each phase with the other is calculated using advection correction factors (Berning & and Djilali, 2003) which are used to modify the velocity of the phase of interest. To define the volumes of each phase present, an equilibrium condition is used. One of the first formulations using the MM model was carried out by Wang and Cheng (1996) and it models the liquid phase pressure as the pressure difference between the capillary and gas phase pressures. The MM model has also been widely implemented in studying coupled liquid and gas transport in PEMFCs with the most notable model being developed by Wang et al. (2001). The model developed by Wang et al. (2001) focuses on the flow channels and GDL neglecting the membrane and defines the GDL to be a hydrophilic layer with the catalyst layer being an interface. Water transport inside the GDL is described by viscous drag as well as capillary pressure with the capillary pressure being described by the Leverett function for hydrophilic substances. Condensation and evaporation are modelled using an isothermal assumption. The relative humidity in the cell is calculated in the entire domain and if it is 100%,

condensation occurs and if it is below 100% in the presence of water, evaporation occurs (Wang et al., 2001; Berning, 2002).

The second method is called multi-fluid modelling (MFM) which makes use of a momentum equation for both the vapour and liquid phases. A common method of simplification is to apply the unsaturated flow theory (UFT) which assumes that the pressure gradient of the vapour phase is negligible in comparison to the liquid phase (Faghri & and Zhang, 2006). This assumption cancels out the vapour phase momentum equation thereby simplifying the solving process. Berning and Djilali (2003) developed a 3-D model using UFT assuming that the gas pressure in the GDL is uniform while He et al. (2000) used the UFT approach to develop a model to investigate performance at the cathode side of a PEMFC by considering the catalyst layer to be an interface (boundary condition) and modelling liquid water flow through a fully wetted GDL by coupled shear (from gas flow) and capillary effects (Das, 2010).

A lot of research has been conducted using the above methods, the work conducted by Nam et al. (2003) which investigated the liquid and vapour transport in a 1-D PEMFC model is quite interesting. The model applied the UFT approach in order to simplify the set of equations and assumed that all the product water is formed in the gas phase and condenses if the partial pressure of the water vapour is greater than or equal to the saturation pressure of water. The model also assumes high current density operation and therefore the evaporation of liquid water is neglected due to the high levels of saturation present in the GDL.

As discussed briefly in section 2.3.3, Dawes et al. (2009) developed a model which improved upon that developed by Lum and McGuirk (2005) by investigating liquid water flooding on gas diffusion at high current densities. This was done by considering effective diffusivity models that account for the tortuosity and relative water saturation of the porous fuel cell electrodes. The models were derived using percolation theory and were coupled with the developed CFD model (Dawes et al., 2009). Just as with the model developed by Lum and McGuirk (2005), the results of Dawes et al. (2009) were also validated with the experimental and simulated data from Shimpalee et al. (1999). Unlike the work done by Lum and McGuirk (2005), Dawes et al. (2009) found a good agreement with the both model predictions and experimental data from Shimpalee et al. (1999) at low and medium current densities as well as for a wide range of relative humidity conditions. The authors state a slight discrepancy between the two models is due to the use of Fick's law rather than the Maxwell-Stefan equations though the close agreement between the two models as well as the experimental data suggest that Fick’s law is a reasonable assumption for gaseous species transport.

2.5. Model Accuracy

As stated in section 2.1, the type of model used depends on the outcome required, however, most of the models developed since the early work by Bernardi and Verbrugge (1991) have become more

complex with intricate details being studied such as two-phase flow, pore network modelling (for better understanding of the operating behaviour through the GDL), high current density operation and current distribution. These intricacies have significantly improved model accuracy, however, they have also vastly increased simulation time. The question is therefore raised as to how inaccurate a lower dimension model such as a 1-D system is in comparison to a higher dimension one such as a 3-D CFD based simulation.

Very little research has been conducted into the direct comparison between lower and higher dimension models to determine the accuracy when modelling mass transport phenomena. One such comparison was done by Falcao et al. (2011) who found a close comparison with 1-D and 3-D simulations, however, a polarization curve obtained from each model was used to prove the close comparison with no direct concentration profile or mole fraction comparison between the two models being done. Mole fraction distributions for various species were provided for the 1-D simulation in a previous publication (Falcao et al., 2009), however, the 3-D model mole fraction data was provided as 2-D contour plots leading to a difficult individual comparison of the two models.

2.6. Fuel Cell Modelling – Closing Remarks

Experimental research in the area of PEMFCs focuses on the commercialisation of the technology by the improvement of cell performance specifically studying areas such as catalyst utilization, membrane durability and reaction rate kinetics. However, a detailed experimental understanding of the mass transport of species within the cell is limited due to the size constraints of typical PEMFCs. Several processes that cannot be measured well experimentally are fluid mechanics within the channel, species transport, water management and current distribution. While fuel cell modelling provides a better understanding of mass transport phenomena, uncertainty is associated with model accuracy as discussed above. Further insight into model accuracy can be achieved by detailed comparison between a lower and higher dimension mathematical PEMFC model.

3. THESIS OBJECTIVES

Further development in fuel cell design is hampered by the lack of fundamental models which reveal the physical and chemical interactions. While computational fluid dynamics simulations are available, the timeframe for solving these simulations renders them unfeasible in any rigorous FC design optimisation. The objective of the present investigation is to determine the minimum dimension of a mathematical model that can accurately simulate processes occurring within the PEMFC. This is done to speed up not only the simulation process but also the development and simulation of the model to aid in better design and testing of various PEMFC component properties (porosity, conductivity, layer thickness etc.).

To this end, 1-D (directional axis perpendicular to the membrane) and 3-D steady state isothermal mathematical models were developed and simulated in order to investigate the transport of reactant species through the various layers of the cell at the anode side. The 1-D model was developed using Fick's Law and the control volume approach to model mass transfer in the cell. The rates of hydrogen oxidation and oxygen reduction were modelled using the Butler-Volmer equation. An assumption was made that the pressure gradient through the GDL is negligible, leading to the transport process in the GDL being modelled as a diffusion-driven process. To simulate the catalyst layer in the 1-D system, an interfacial model was proposed whereby the reactants are consumed at the surface of the catalyst layer.

The 3-D model was developed using a complete Navier-Stokes approach. To model the catalyst and gas diffusion layers accurately, several parameters such as porosity and permeability needed to be accounted for. That was achieved by modelling each of the two layers as continua and developing a momentum sink term based on Darcy's law for each layer in all three directions of interest. To simulate the rate of hydrogen oxidation, a species sink term was developed based on current density for the catalyst layer continuum outlined above.

The reason for investigating the anode side rather than the entire cell was that the obtained results from each model for the anode were thought to be sufficient to perform a comparative analysis in acquiring a better understanding on the model accuracy. For a single phase system, this assumption was not restricted to the anode only and allowed the accuracy of the model to be extended to the cathode side. Investigating only the anode rather than the entire cell also significantly reduced the simulation time.

The value of an accurate 1-D solver was illustrated by the development of a 3-D whole-cell simulation. This was done to determine a better understanding of simulation time required for a CFD simulation as well as the significant concentration gradient axis/axes (i.e. the axis in which the highest gradient is seen) and model fuel cell performance. The fuel cell performance result from the 3-D simulation was used to validate the model by comparing the result with experimental data obtained from the

University of Cape Town (UCT) HySA/Catalysis fuel cell laboratory run under the same operating conditions as the model.

Conclusions drawn from the 1-D and 3-D half-cell model comparisons as well the 3-D whole-cell simulation allowed additions/improvements to the simplified 1-D model to be identified.

The 1-D model was simulated using *MATLAB* while the 3-D model geometry was developed using the meshing program *GAMBIT* and the model was simulated using the CFD solver *FLUENT*.

Based on the above objectives, the following hypothesis can be postulated stating that a 1-D model can accurately predict the concentration profiles of the reactant species in a PEMFC with a significant reduction in computation time when compared to a higher dimension model.

1) Do the concentration profiles along the z-axis for each model follow the same path in each of the individual layers of the cell (flow channel, catalyst layer and GDL)?
2) In the 3-D model, are the concentration gradients along the x- and y- axes within the porous media (axes parallel to the MEA) negligible when compared with the concentration change along the z-axis (axis perpendicular to the MEA) within the porous medium?
3) What is the computational expense of simulating the 1-D model as compared with to the 3-D model?
4) Do the 3-D and 1-D models compare well with the experimental data provided by the UCT laboratory?

4. METHODOLOGY

The comparison of a comprehensive 3-D single phase model with a 1-D model is the focus of this study. The following chapter discusses the development of both models in detail.

4.1. 1-D Model Development

In this section, the 1-D model domain selection and geometry are discussed together with the assumptions made in developing the 1-D model. The governing equations for 1-D PEMFC modelling are also presented. The parameters and constants used are then illustrated along with the boundary conditions.

4.1.1. Computational Domain and Geometry

A typical single cell PEMFC geometry is illustrated in Figure 4. The cell includes the gas flow channels, GDLs, catalyst layers and the PEM. The modelling domain for the 1-D system considers only the anode side. The reason behind investigating the anode side rather than the entire cell would be that the obtained results from the 1-D and 3-D models for the anode will be sufficient in order to perform a comparative analysis in order to acquire a better understanding on the model accuracy. For a single phase system, this assumption will not be restricted to the anode only and will allow the accuracy of the model to be extended to the cathode side. Investigating only the anode rather than the entire cell also significantly reduces the simulation time. The z-axis is the chosen dimension to model as it is assumed the significant concentration changes in the PEMFC occur in this direction. This assumption is supported by the work carried out by Yi and Nguyen (1998) and Dutta et al. (2000) where it was shown that that the concentration and current density vary slowly along the axes parallel to the PEM within the MEA. This allows the fluxes of gases and currents in the porous media (GDL and catalyst layers) in the axes parallel to the PEM to be neglected when compared with the fluxes perpendicular to the PEM (i.e. the z-axis w.r.t to Figure 4) (Kornyshev & Kulikovsky, 2001).

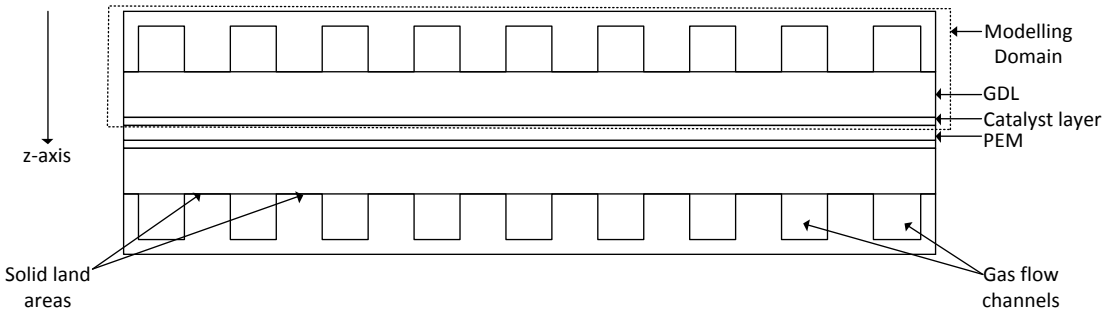

Figure 4: Modelling Domain of 1-D System

Table 2: 1-D Geometry dimensions

PEMFC layer	Thickness (z-axis direction) (mm)
Flow channel	1
GDL	0.4375
Catalyst Layer	0.0625

The different layer thicknesses of each of the individual layers are illustrated in table 1 and were obtained from a study conducted by Dawes et al. (2009).

4.1.2. 1-D Modelling Assumptions

In setting up and solving the 1-D model, several assumptions were made, these are stated below:

- The model is developed for steady state, isothermal fuel cell operation and only considers the anode side mass transport
- Reactant gas mixtures are modelled as ideal gases
- Diffusion dominates in the GDL region, i.e. convection is negligible
- Reaction only takes place in the catalyst layer and therefore is set to zero in the flow channel and GDL

4.1.3. 1-D Modelling Governing Equations

The equations used to model mass transport for the 1-D model are discussed below, first principles are used to derive the equations.

Using a control volume approach, (4.1) is obtained considering only the flux in the z-direction where N_j refers to the molecular flux per unit area of component *j*, r is the reaction rate C_j refers to the concentration of component *j* and Δy, Δx and Δz are the lengths of each side of the differential element.

$$-\left(N_{j,z} - N_{j,z+\Delta z}\right)\Delta y\Delta x\Delta t + r\Delta y\Delta x\Delta t = \left(N_{j,z} - N_{j,z+\Delta z}\right)\Delta y\Delta x\Delta z \qquad (4.1)$$

Divide (4.1) by $\Delta y\Delta x\Delta z\Delta t$ and taking the limit of the result as the volume tends to zero, (4.2) is obtained which illustrates the differential form of the mass balance equation.

$$-\frac{\delta N_j}{\delta z} + r = \frac{\delta C_j}{\delta t} \qquad (4.2)$$

To account for the molecular flux due to diffusion and convection, N_j is replaced by (4.3) where the first term on the right hand side in the equation accounts for diffusive flux and is illustrated by Fick's law as shown in (2.1) while the second term accounts for convective flux where u_j defines the velocity of species *j*. The result of the substitution is shown in (4.4).

$$N_j = -D_j\left(\frac{\delta C_j}{\delta z}\right) + u_j C_j \tag{4.3}$$

$$D_j\left(\frac{\delta^2 C_j}{\delta z^2}\right) - u_j\frac{\delta C_j}{\delta z} + r = \frac{\delta C_j}{\delta t} \tag{4.4}$$

At steady state, (4.4), the accumulation term on the right hand side of the equation falls away, leaving (4.5), which is the differential equation that will be solved in each of the three zones of interest in the fuel cell anode (flow channel, GDL and catalyst layer).

$$D_j\left(\frac{\delta^2 C_j}{\delta z^2}\right) - u_j\frac{\delta C_j}{\delta z} + r = 0 \tag{4.5}$$

In each zone, (4.5) is modified appropriately based on the processes occurring in that zone. Table 3 illustrates this. The reaction only occurs in the catalyst layer, therefore the reactive term is set to zero in the flow channel and GDL, while diffusion is the dominates over convection in the GDL and catalyst layer leading to the convection term being negligible in these two zones.

Table 3: Terms present in each layer of the PEMFC

	Flow channel	GDL	Catalyst layer
Diffusion	Yes	Yes	Yes
Convection	Yes	No	No
Reaction	No	No	Yes

The reaction rate is defined by the anode hydrogen source term as illustrated in (4.6), where i is the current density, *A* is the area of the MEA, *F* is Faraday's constant and M_{H_2} is the molar mass of hydrogen.

$$S_{H_2} = -\frac{iA}{2F}M_{H_2} \tag{4.6}$$

4.1.4. 1-D Modelling Boundary Conditions

Two types of boundary conditions can be used to solve the 1-D model, namely the Neumann and Dirichlet types. The Neumann type condition specifies the value/values of the derivative of the state variable on the boundary while the Dirichlet type condition specifies the value/values of the state variable on the boundary. The following model makes use of Dirichlet boundary type where the concentration at each interface is used.

A study by Oliveira et al. (2011) developed a 1-D model for a direct methanol fuel cell (DMFC) that modelled the concentration at the interfaces between zones (flow channel, GDL and catalyst layer) by assuming local equilibrium and modelled a linear relationship between the concentration in the previous zone and an assumed equilibrium partition coefficient for each zone of the cell. This is shown in (4.7) where K represents the equilibrium partition coefficient and C_i is the concentration of species at zone *i* in the cell.

$$C_{i+1} = K_i C_i \tag{4.7}$$

While this method makes theoretical sense, an area of concern was the methodology used to obtain the partition coefficients used in the model. The methodology was not provided and no references were used to obtain the equilibrium partition coefficient value used.

A similar approach to Oliveira et al. (2011) is adopted in solving the 1-D model with an assumption being made that the concentration gradient is linear through each of the zones, this is done as a first estimate to obtain the concentrations at each of the interfaces (C_0 and C_1 as shown in Figure 5). Using Figure 5, the concentration for each zone interface will be derived.

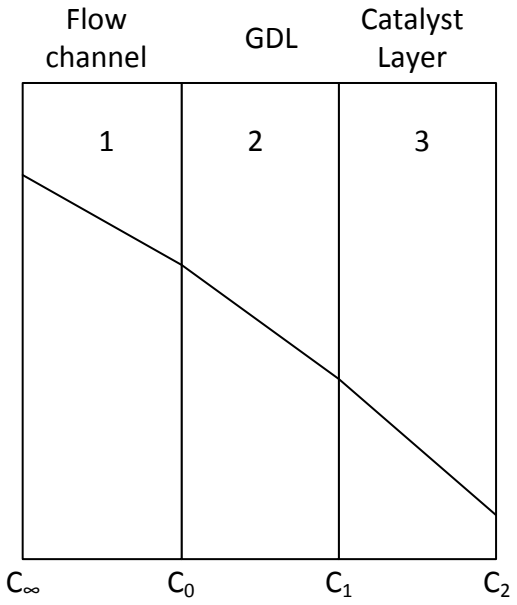

Figure 5: Illustration of linear concentration gradient assumption and model zones and interfaces

The general transport can be described using (4.8) for any given zone where N_i is the molecular flux per unit area in zone *i* and h_i is the mass transfer coefficient in zone *i*.

$$N_i = h_i\left(C_i - C_{i-1}\right) \tag{4.8}$$

Applying (4.8) to the 1-D model using Figure 5 and assuming fluxes are equal, the following relationship is obtained.

$$N_1 = N_2 = N_3 \tag{4.9}$$

$$h_1\left(C_\infty - C_0\right) = h_2\left(C_0 - C_1\right) = h_3\left(C_1 - C_2\right) \tag{4.10}$$

Eliminate C_2 from (4.10) by realising that C_2 is the initial concentration minus the amount consumed in the catalyst layer. This is shown in (4.11).

$$h_3\left(C_1 - C_2\right) = h_3\left(C_1 - \left(h_1 C_\infty + S_{H_2}\right)\right) \tag{4.11}$$

Replacing (4.11) in (4.10) and solving for C_0, we obtain the following equations:

$$\left(C_0 - C_1\right) = \frac{h_1}{h_2}\left(C_\infty - C_0\right) \tag{4.12}$$

$$\left(C_1-\left(h_1C_\infty+S_{H_2}\right)\right)=\frac{h_1}{h_3}\left(C_\infty-C_0\right) \tag{4.13}$$

Summing (4.12) and (4.13) and rearranging the obtained result so that C_0 is the subject, (4.14) is the result.

$$C_0=\frac{C_\infty\left(h_1\left(\frac{1}{h_2}+\frac{1}{h_3}\right)+h_1\right)+S_{H_2}}{1+h_1\left(\frac{1}{h_2}+\frac{1}{h_3}\right)} \tag{4.14}$$

A similar process is done to obtain the equation for C_1. Summing (4.15) and (4.16) and rearranging the obtained result so that C_0 is the subject, (4.17) is the result.

$$\left(C_\infty-C_0\right)=\frac{h_2}{h_1}\left(C_0-C_1\right) \tag{4.15}$$

$$\left(C_1-\left(h_1C_\infty+S_{H_2}\right)\right)=\frac{h_2}{h_3}\left(C_0-C_1\right) \tag{4.16}$$

$$C_1=\frac{C_0\left(1+h_2\left(\frac{1}{h_1}+\frac{1}{h_3}\right)\right)+C_\infty\left(h_1-1\right)+S_{H_2}}{1+h_2\left(\frac{1}{h_1}+\frac{1}{h_3}\right)} \tag{4.17}$$

The mass transfer coefficients for the different zones are obtained using Sherwood number (*Sh*) correlations similar to those used in Oliveira et al. (2011). The expression is shown in (4.18), Ra is the Rayleigh number, Sc is the Schmidt number, L is the length of the active are and D is the diffusivity. The equations for the Rayleigh, Schmidt and Grashof (*Gr*) numbers are shown in (4.19)-(4.21) where ν is the kinematic viscosity, g is the acceleration due to gravity and C_j is the concentration of species *j* at the relevant zone of the cell (Oliveira et al., 2011).

$$Sh=\frac{h_iL}{D_{ij}}=\left(0.825+\frac{0.387Ra^{\frac{1}{6}}}{\left(1+\left(\frac{0.492}{Sc}\right)^{\frac{9}{16}}\right)^{\frac{8}{27}}}\right)^2 \tag{4.18}$$

$$Ra = Gr \cdot Sc \tag{4.19}$$

$$Sc = \frac{\nu}{D_{ij}} \tag{4.20}$$

$$Gr = \frac{g \Delta C_j L^3}{C_j \nu^2} \tag{4.21}$$

4.1.5. 1-D Modelling Computational Procedure

The 1-D model was set up and solved using *MATLAB* with an ODE45 solver being used to solve the differential equation for each zone. These equations are presented in section 4.1.3 and the modifications for the various zones are shown in Table 3. The solution algorithm is shown in Figure 6, the dotted box shows the solving procedure used in the ODE45 function and is known as the 5th order Runge-Kutta technique.

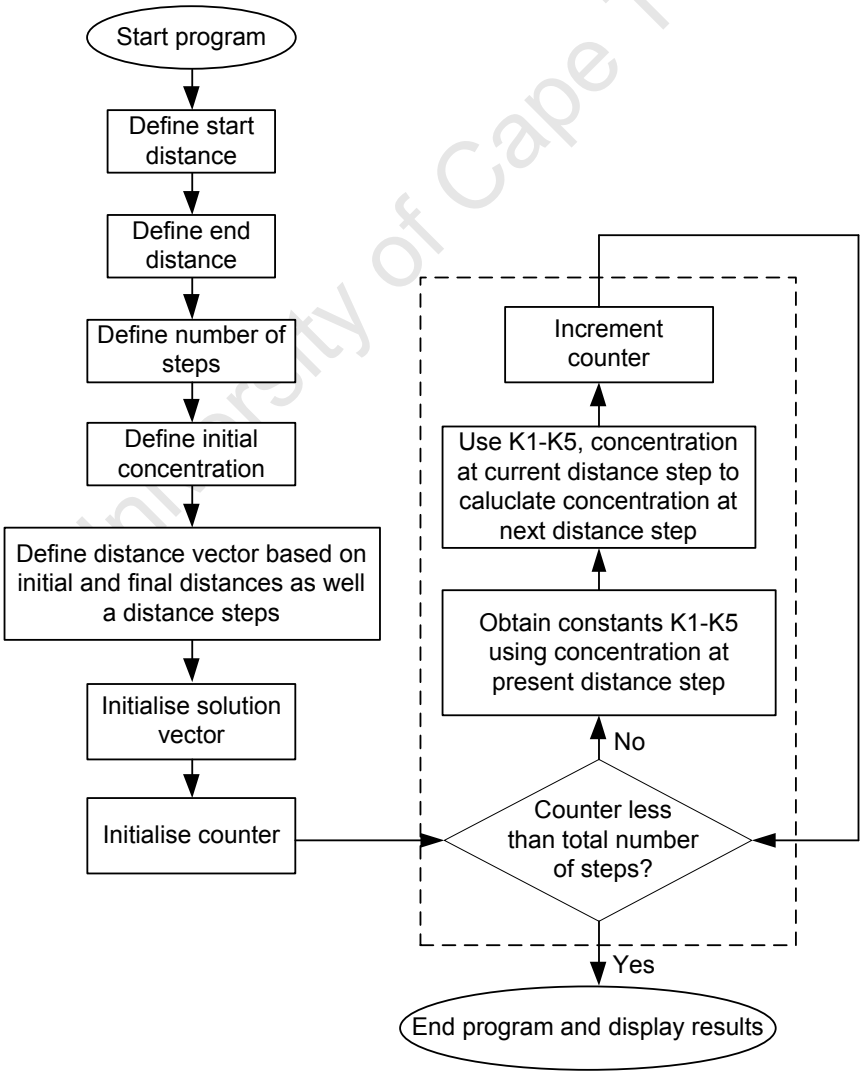

Figure 6: 1-D model solution algorithm

4.2. 3-D Model Development

In this section, the computational domain selection and geometry design for the 3-D model are discussed along with the governing equations for 3-D PEMFC modelling and the auxiliary equations that are used to model PEMFC performance. The source terms used for the mass, momentum and species equations for each layer in the cell are also shown. The parameters and constants used are then illustrated along with the boundary conditions. Finally the computational procedure used and numerical solution algorithm is provided with a brief discussion of user defined function (UDF) development.

4.2.1. Computational Domain and Geometry

The modelling domain for the 3-D system is shown in Figure 7. The modelling domain consists of a single anode and cathode gas flow channel, the anode and cathode GDLs, catalyst layers and the PEM. The reason for considering just one channel rather than the entire flow-field is to take advantage of the geometric periodicity of the flow channels (Berning et al., 2002) and thereby significantly reduce the geometry design step as well as the computational solving time.

The Geometry was designed and meshed using GAMBIT using the dimensions shown in Table 4. All the dimensions used were obtained from the study conducted by Dawes et al. (2009).

Table 4: 3-D Geometry dimensions

PEMFC layer	Length (x-axis direction) (mm)	Width (y-axis direction) (mm)	Thickness (z-axis direction) (mm)
Flow channel	34	0.8	1
GDL	34	1.6	0.4375
Catalyst Layer	34	1.6	0.0625
PEM	34	1.6	0.127

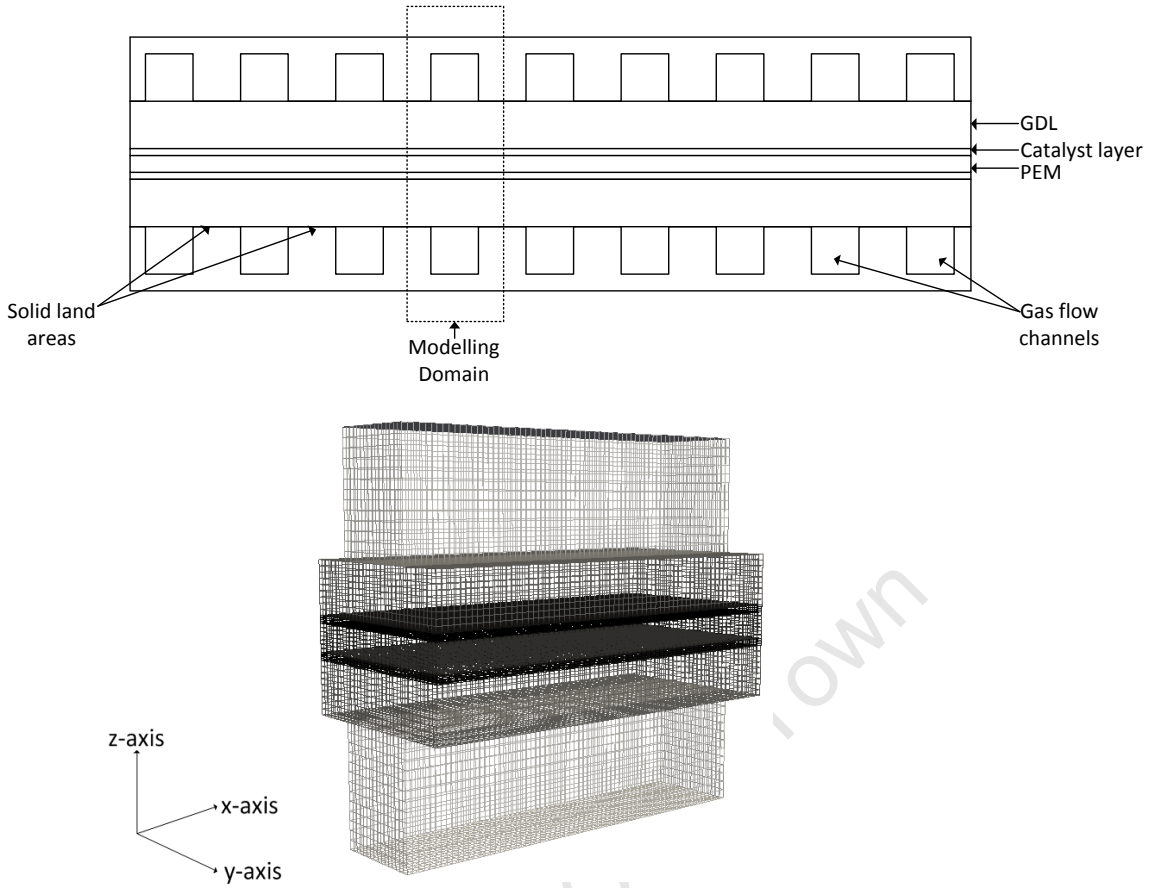

Figure 7: Typical PEMFC illustrating modelling domain

4.2.2. 3-D Modelling Assumptions

In setting up and solving the 3-D model, several assumptions were made, these are stated below:

- The model is developed for steady state, isothermal fuel cell operation
- Reactant gas mixtures are modelled as ideal gases
- The membrane is modelled as a solid phase which means the reactant gases are impermeable through the membrane
- Electric resistance is negligible compared to ionic resistance

4.2.3. 3-D Modelling Governing Equations

The Navier-Stokes (NVS) equations are the governing equations for fluid flow, they include the mass, momentum, species and energy equations. For the case of a PEM fuel cell operating under steady state and isothermal conditions, the governing equations are the conservation of mass, momentum and species. The energy equation is not considered for this work as the model developed is isothermal. A thorough framework (derivations are provided in the relevant appendix) of the governing equations is provided in the following section, from which the rest of the modelling discussion will draw.

The conservation of mass maybe expressed in the form illustrated in (4.22) where ρ is the fluid density, $\vec{u}$ defines the velocity vector field and S_{mass} is the mass source term. The derivation is shown in Appendix A.1.

$$\nabla \cdot \left(\rho \vec{u} \right) = S_{mass} \tag{4.22}$$

In the case where the fluid is incompressible, (4.22) reduces to the continuity equation because of the constant fluid density.

The momentum balance for a steady state system is shown in (4.23). The term on the left hand side of equation the equation represent the rate of change of momentum, the term defines the non-linear convective term which describes the variation of velocity over a position in space. The terms on the right hand side of equation represent the forces acting on the fluid. The first term represents the pressure force while the second the viscous force where μ is the fluid viscosity, the third term is the momentum source term. A detailed derivation from first principles can be found in Appendix A.1.

$$\rho \vec{u} \cdot \nabla \vec{u} = -\nabla P + \nabla \cdot \left(\mu \nabla \vec{u} \right) + S_{mom} \tag{4.23}$$

In porous media such as the GDLs and catalyst layers, the momentum source term is made of two terms, namely the viscous and inertial resistance terms. Viscosity is the property of a fluid to resist flow when an external force is applied on it while inertia is the property of an object to remain at a constant velocity unless an external force acts on it. Therefore inertia is the influence that tends to keep the fluid in motion while viscosity tends to retard it.

For low Reynolds number values (creeping flow), the viscous and pressure forces are dominant and the inertial resistance term is negligible in comparison (a linear relationship between pressure drop and velocity). This linear relationship is known as Darcy's law. However, when Reynolds numbers are large, the deviation from Darcy's law rises due to the increased contribution to the source term from the inertial resistance term. This can be explained by understanding that the cause of inertia of fluid flows are the non-linear interactions associated with the flow field which can result in instabilities in the flow leading to turbulence. Turbulent flow is defined by large Reynolds numbers and therefore when Reynolds numbers are large inertial effects dominate.

The Reynolds number for the flow in the fuel cell was found to be 21 which classifies the flow inside the cell as laminar, therefore the momentum source term is defined by (4.24). (4.24) defines Darcy's law where *K* is the permeability through the porous media and it is used to describe the flow of a fluid through a porous medium.

$$S_{mom} = -\frac{\mu \vec{u}}{K} \tag{4.24}$$

The species conservation equation is the final governing equation used. This equation is illustrated in (4.25) where $\vec{y}$ are the mole fraction scalar fields and the subscript *j* defines the different species (hydrogen, water, oxygen and nitrogen), D_j^{eff} is the effective diffusivity of the species *j* corrected for porosity of the medium using the Bruggemann correction factor (Berning et al., 2002). The diffusivity correction equation and application of the Bruggemann correction is shown in (4.26) where D_j is the diffusivity of species *j* and $\varepsilon_{material}$ is the porosity of the porous material.

$$\nabla \cdot \left(\rho \vec{u} \vec{y}_j \right) = \nabla \cdot (D_j^{eff} \rho \nabla \vec{y}_j) + S_j \tag{4.25}$$

$$D_j^{eff} = D_j \varepsilon_{material}^{1.5} \tag{4.26}$$

The species source terms are defined only in the reactive zone of the cell (anode and cathode catalyst layers). The source terms for the individual layers are discussed below.

The anode hydrogen source term was discussed in section 4.1.3 and shown in (4.6). The cathode oxygen source term is illustrated in (4.27), where i is the current density, *A* is the area of the MEA, *F* is Faraday's constant and M_{O_2} is the molar mass of oxygen.

$$S_{O_2} = -\frac{iA}{4F} M_{O_2} \tag{4.27}$$

Table 5 shows a summary of the source terms used in each layer of the model.

Table 5: Summary of source terms for mass, momentum and species equations in 3-D model

Source Terms	Flow Channels	GDLs	Catalyst Layers	PEM
S_{mass}	None	None	Anode side: $S_{H_2} = -\frac{iA}{2F} M_{H_2}$ $S_{H_2O\_a} = -\frac{\alpha iA}{F} M_{H_2O}$ Cathode side: $S_{O_2} = -\frac{iA}{4F} M_{O_2}$ $S_{H_2O\_c} = \frac{[1+2\alpha]iA}{2F} M_{H_2O}$	None
S_{mom}	None	Anode and Cathode: $S_{mom} = -\frac{\mu \vec{u}}{K_{GDL}}$	Anode and Cathode: $S_{mom} = -\frac{\mu \vec{u}}{K_{CL}}$	None
S_k	None	None	Anode side: $S_{H_2} = -\frac{iA}{2F} M_{H_2}$ $S_{H_2O\_a} = -\frac{\alpha iA}{F} M_{H_2O}$ Cathode side: $S_{O_2} = -\frac{iA}{4F} M_{O_2}$ $S_{H_2O\_c} = \frac{[1+2\alpha]iA}{2F} M_{H_2O}$	None

4.2.4. 3-D Modelling Auxiliary Equations

The auxiliary equations of the fuel cell are used to obtain parameters such as the net water transport coefficient, electro-osmotic drag coefficient, water activity and water concentration. These parameters are all vital in determining the water transport within the cell as well as its performance and hence 3-D model validation. These equations were obtained from Berning et al. (2002), Lum and McGuirk (2005) and Dawes et al. (2009). Many previous studies in fuel cell modelling have used these relationships and validated the results obtained and therefore they are thought to be sufficient to obtain the required parameters for the 3-D model.

Net Water Transport Coefficient

The net water transport coefficient (α) is used to determine water vapour transport through the membrane. This is done by considering electro-osmotic drag (n_d) which is determined using (4.29) and back diffusion of water which is determined from the second term on the right hand side of (4.28). $C_{H_2O,c}$ and $C_{H_2O,a}$ are the water concentrations at the anode and cathode respectively, i is the current density and $t_{Membrane}$ is the membrane thickness.

$$\alpha = n_d - \frac{F \cdot D_{H_2O}(C_{H_2O,c} - C_{H_2O,a})}{i \cdot t_{Membrane}} \tag{4.28}$$

Electro-osmotic Drag Coefficient and Water Activity

The electro-osmotic drag coefficient is used to determine the amount of water transported from the anode to the cathode through the membrane, the relationship used to determine the coefficient is empirical and based on the water activity. (4.29) shows the empirical relationship used to obtain the electro-osmotic drag where a_a is the water activity at the anode and is determined using the water vapour saturation pressure. The water activity is defined by (4.30) where $P_{Sat}(T)$ is the water vapour saturation pressure which can be obtained using the Antoine equation, P_{cell} is the cell operating pressure, and the subscript *i* describes a specific zone in the cell (anode or cathode).

$$\begin{aligned} n_d &= 0.0049 + 2.02a_a - 4.53a_a^2 + 4.09a_a^3 \Big\} \text{if } a_a \le 1 \\ n_d &= 1.59 + 0.159(a_a - 1) \Big\} \text{if } a_a > 1 \end{aligned} \tag{4.29}$$

$$a_i = \frac{y_{H_2O,i} P_{cell}}{P_{Sat}(T)} \tag{4.30}$$

Water Diffusion Coefficient and Water Concentration

The final two terms that need to be defined are the water diffusion coefficient and the water concentrations at the anode and cathode. The water diffusion coefficient, shown in (4.31), is a function of the electro-osmotic drag and is therefore also dependent on the water activity. The water concentration for either the anode or cathode, shown in (4.32), is also a function of the water activity as well as the dry density ($\rho_{Membrane,dry}$) and dry molar mass ($M_{Membrane,dry}$) of the membrane.

$$D_{H_2O} = \left(5.5 \cdot 10^{-11}\right) n_d \exp\left(2416\left(\frac{1}{303} - \frac{1}{T}\right)\right) \tag{4.31}$$

$$\begin{aligned} C_{H_2O,i} &= \frac{\rho_{Membrane,dry}}{M_{Membrane,dry}}\left(0.0043 + 17.8a_i - 39.8a_i^2 + 36.0a_k^3\right) \Big\} \text{if } a_i \le 1 \\ C_{H_2O,i} &= \frac{\rho_{Membrane,dry}}{M_{Membrane,dry}}\left(14 + 1.4\left(a_i - 1\right)\right) \Big\} \text{if } a_a > 1 \end{aligned} \tag{4.32}$$

4.2.5. Modelling Fuel Cell Loss Mechanisms – Polarization

As discussed in section 1.2, the fuel cell performance is affected by several loss mechanisms, namely these are the activation, ohmic and concentration losses. Modelling of these mechanisms is important as the most common way of validating a fuel cell model is the comparison of the performance curves obtained from the models against experimental performance data. The following section discusses the equations used to model each of these mechanisms. The bulk of the assumptions made in this section were based on the work by Min (2009).

Activation Losses

The activation losses can be modelled using the Butler-Volmer equation shown in (4.33) and (4.34), a full derivation of the Butler-Volmer equation as well as the limiting cases is presented in Appendix A.2. These equations make an assumption that the charge transfer coefficient for the anode and cathode, α_a and α_c is 0.5 (Min, 2009). The other terms in the equations are $i_{a,0}$ and $i_{c,0}$ which define the exchange current densities for the anode and cathode respectively, $C_{H_2,ref}$ and $C_{O_2,ref}$ which define the reference concentrations of hydrogen and oxygen, n_a and n_c which indicate the number of electrons taking part in the anode and cathode reactions respectively and η_a and η_c which define the activation overpotential for the anode and cathode respectively.

$$i_a = 2i_{a,0}\left(\frac{C_{H_2}}{C_{H_2,ref}}\right)^{0.5}\sinh\left(\frac{\alpha_a\eta_a F n_a}{RT}\right) \tag{4.33}$$

$$i_c = 2i_{c,0}\left(\frac{C_{O_2}}{C_{O_2,ref}}\right)\sinh\left(\frac{\alpha_c\eta_c F n_c}{RT}\right) \tag{4.34}$$

Ohmic Losses

The ohmic losses are observed due to resistance to proton and electron transfer within the cell. The losses can be modelled as shown by (4.35) where $\eta_{Ohmic\_protons}$ is the loss due to proton transfer and $\eta_{Ohmic\_electrons}$ is the loss due to electron transfer. Min (2009) defined the resistance to electron transfer as 0.1 Ωcm^2 and the resistance to proton transfer can be found using (4.36) where $t_{Membrane}$ is the membrane thickness and $k_{Membrane}$ is the membrane conductivity found using (4.37).

$$\eta_{Ohmic\_total} = \eta_{Ohmic\_electrons} + \eta_{Ohmic\_protons} = i\left(R_{electrons} + R_{protons}\right) \tag{4.35}$$

$$R_{protons} = \frac{t_{Membrane}}{k_{Membrane}} \tag{4.36}$$

$$k_{Membrane} = 100\left(0.00514\left(\frac{M_{Membrane,dry}}{\rho_{Membrane,dry}}\right)C_{H_2O,a} - 0.00326\right)\exp\left(1268\left(\frac{1}{303} - \frac{1}{T}\right)\right) \quad (4.37)$$

Concentration Losses

The concentration losses are seen at higher current densities due to diffusion limitations within the cell. These losses can be modelled as follows using (4.38). the limiting current density (i_L) is defined using (4.39) where the subscript *i* defines the zone (anode or cathode), the subscript *j* defines the species, t_{GDL} defines the GDL thickness, $D_{j,i}$ is the effective diffusivity of species *j* through the porous media in zone *i*, $C_{j,i}$ is the concentration of species *j* in zone *i*.

$$\eta_{concentration} = \frac{RT}{nF}\ln\left(1 - \frac{i}{i_L}\right) \quad (4.38)$$

$$i_L = \frac{nFD_{j,i}C_{j,i}RT}{t_{GDL}} \quad (4.39)$$

4.2.6. 3-D Modelling Boundary Conditions

As stated in section 4.1.4, the two main types of boundary conditions used to solve differential equations are Neumann and Dirichlet conditions, these are commonly used in CFD modelling.

For this study, the cathode and anode inlet parameters are used as the boundary conditions with the Dirichlet boundary type being applied to the inlet of the anode and cathode gas flow channel. The inlet velocities, gas feed species mass fractions and temperatures are specified. (4.40) and (4.41) shows the equations used to calculate the inlet velocity of the anode and cathode feed gas stream respectively where the subscripts *a* and *c* denote the anode and cathode respectively, ζ is the stoichiometric flow ratio, *i* is the average current density, A_{MEA} is the MEA crossectional area, R is the universal gas constant, T_{in} is the inlet temperature, P_{in} is the inlet pressure and $A_{Channel}$ is the cross-sectional area of the flow channel. A detailed derivation of these equations is provided in Appendix A.2. The outlet of the gas channel is defined as a pressure outlet while the no-slip boundary (zero velocity) condition is applied to the walls.

$$u_{in,a} = \zeta_a \frac{i}{2F} A_{MEA} \frac{1}{y_{H_2,in}} \frac{RT_{in,a}}{P_{a,in}} \frac{1}{A_{Channel}} \quad (4.40)$$

$$u_{in,c} = \zeta_c \frac{i}{4F} A_{MEA} \frac{1}{y_{O_2,in}} \frac{RT_{in,c}}{P_{c,in}} \frac{1}{A_{Channel}} \quad (4.41)$$

4.2.7. Model Parameters

Table 6 illustrates the parameters used in the model development and simulation as well as operating conditions.

Table 6: Modelling Parameters

Parameters	Value	Reference
Geometry Dimensions		
Flow channel width (y-axis) (m)	8×10^{-4}	(Dawes et al., 2009)
Flow channel height (z-axis) (m)	1×10^{-3}	(Dawes et al., 2009)
Flow channel Length (x-axis) (m)	3.4×10^{-3}	(Dawes et al., 2009)
Channel land width (y-axis) (m)	8×10^{-4}	(Dawes et al., 2009)
GDL thickness (m)	4.375×10^{-4}	(Dawes et al., 2009)
Catalyst layer thickness (m)	6.25×10^{-5}	(Dawes et al., 2009)
PEM thickness (m)	1.27×10^{-4}	(Dawes et al., 2009)
GDL/Catalyst layer properties		
GDL porosity	0.4	(Berning et al., 2002)
Catalyst layer porosity	0.4	(Berning et al., 2002)
GDL Permeability (m^2)	5×10^{-11}	(Dawes et al., 2009)
CL Permeability (m^2)	1.76×10^{-11}	(Min, 2010)
Cell operating conditions (University of Cape Town Fuel Cell Lab, 2012)		
Anode and cathode operating pressure (bar)	2 bar	
Anode and cathode operating Temperature (K)	353	
Relative humidity at anode (%)	100	
Relative humidity at cathode (%)	50	
Stoichiometric feed ratio at anode	1.5	
Stoichiometric feed ratio at cathode	2	
anode inlet mass fractions		
x_H_2	0.3218	
x_H_2O	0.6782	
cathode inlet mass fractions		
x_O_2	0.215	
x_N_2	0.7075	
x_H_2O	0.0775	
General		
Faradays constant (C/mol)	96485	
number of electrons at anode	2	
number of electrons at cathode	4	
anode and cathode transfer coefficient	0.5	

Diffusion coefficients		
$D_{H2\text{-}H20}$ @ 307.1 K (m^2/sec)	9.15 x 10^{-5}	(Berning et al., 2002)
$D_{O2\text{-}N2}$ @ 293.2 K (m^2/sec)	2.20 x 10^{-5}	(Berning et al., 2002)

4.2.8. 3-D Modelling Computational Procedure

A mesh dependent solution has several limitations on the results obtained and often implies the solution is incorrect. The major limitation is the use of the results in practical situations due to the poor accuracy, with a crude solution being obtained. Mesh independence is a key factor in determining an accurate solution to the system. A Mesh independent solution is one that is independent of the specified mesh size.

When meshing the system, each zone (channels, GDLs, catalyst layers and PEM) was meshed independently using a different mesh size to ensure the mesh independence by providing adequate resolution in each zone over which the governing equations may be solved.

Initially, a mesh size was selected based on the number of elements obtained in each zone along the height (z-axis) as shown in Figure 8. The simulation results are then analysed by checking the uniformity of the hydrogen concentration obtained, the concentration data is imported from the CFD solver and compared with coarser and more refined mesh sizes. To obtain the more refined mesh size, the current mesh size in each zone is multiplied by a factor of 0.75 and vice versa for a coarser mesh size, in both cases the simulations are re-run to obtain the new results.

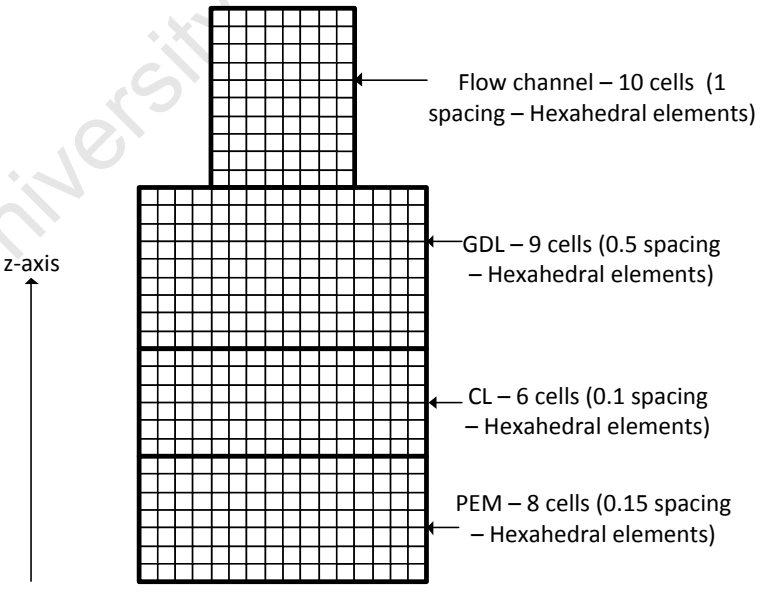

Figure 8: Initial guess of number of elements in each zone (element sizes in figure are not to scale)

Table 7 shows the mesh size selection for the mesh independent solution for each zone and the number of elements obtained along the height for each selection as well as the total number of elements in each volume.

Table 7: Summary of initial mesh size selection

Zone	Mesh type	Mesh size	No. of elements in z-axis	Total elements in volume
Anode flow channel	Hexahedral	1	10	4320
Anode GDL	Hexahedral	0.5	9	7344
Anode Catalyst layer	Hexahedral	0.1	6	4896
PEM	Hexahedral	0.15	8	6528
Cathode flow channel	Hexahedral	1	10	4320
Cathode GDL	Hexahedral	0.5	9	7344
Cathode Catalyst layer	Hexahedral	0.1	6	4896
Total elements in geometry				39648

The SIMPLE algorithm was chosen for the pressure-velocity coupling while the momentum and species equations were discretized using a second and first order upwind scheme respectively. UDFs were written using C++ to create the source terms for the mass, momentum and species equations outlined in Table 5 as well as the velocity inlet boundary conditions, the UDFs were interpreted using the interpreter in FLUENT for use in the simulation. The convergence requirements were set to absolute criteria of 10^{-16} for all the equations being solved. 1000 iterations were done with the solution converging after approximately 600 iterations. The solution algorithm is provided in Figure 9.

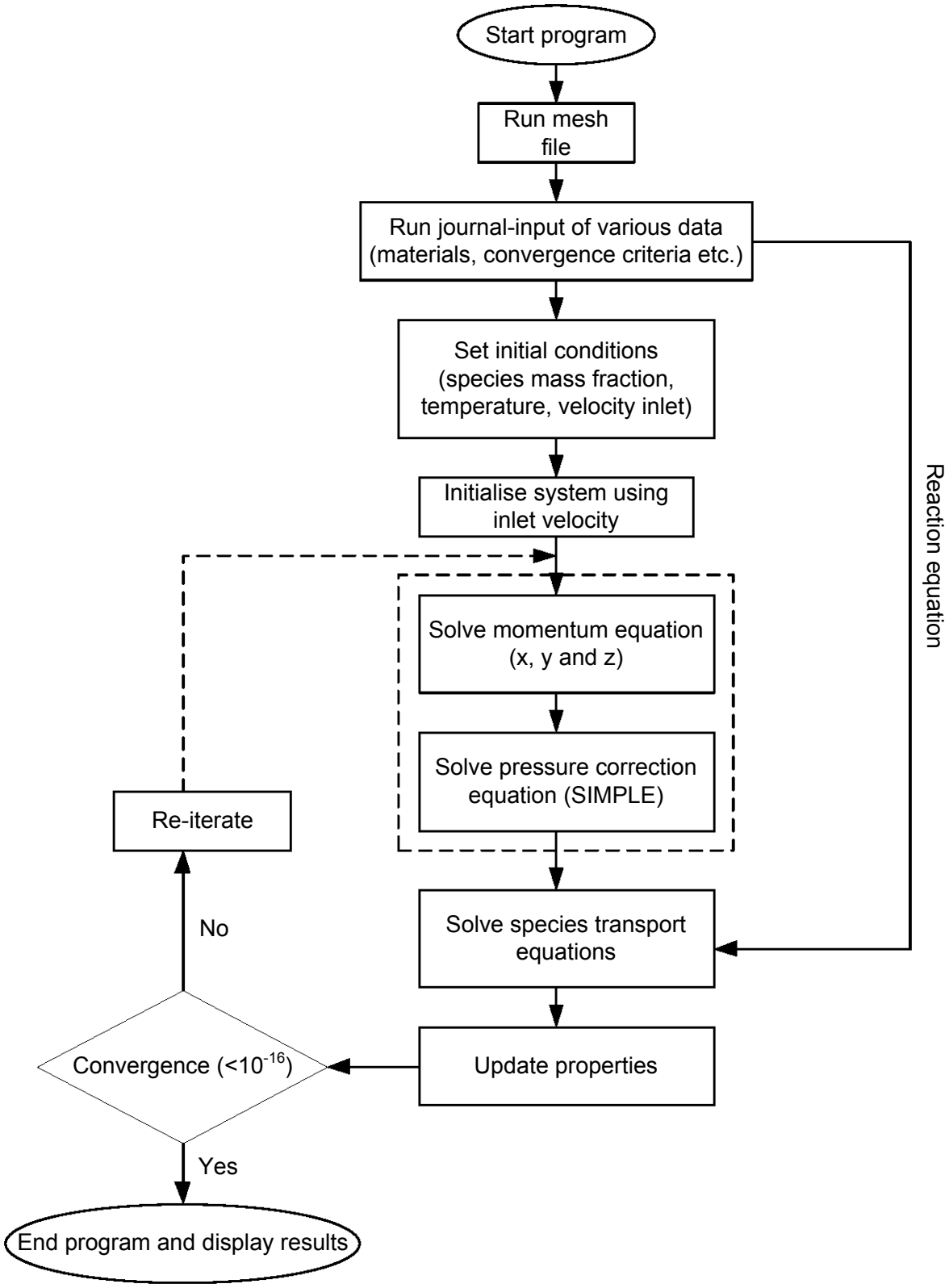

Figure 9: 3-D model solution algorithm

4.2.9. User Defined Functions

Before a discussion into the UDFs is provided, it must be noted that all macros used were pre-defined in the *FLUENT* package.

Inlet velocities are defined using the DEFINE_PROFILE macro with the relevant parameters outlined in section 4.2.7 defined. The DEFINE_SOURCE macro is used to calculate all source terms (momentum and species). For momentum, a source term is defined for each of the porous zones (anode and cathode GDL and catalyst layers) in each of the 3-axes of interest (x-,y- and z-axis). For species consumption, hydrogen and oxygen consumption terms are defined at the anode and cathode catalyst layers respectively. The UDFs for anode and cathode overpotentials are defined using the DEFINE_ADJUST macro. The UDF code written is presented in Appendix B.

5. RESULTS AND DISCUSSION

The following chapter presents and discusses the results of both models developed in section 4 and compares the concentration results of the anode side of the two models. Before the concentration profiles are presented, the 3-D model validation method and procedure is discussed and the validation results shown. Contour plots shown were obtained using the open source animation program *PARAVIEW*.

5.1. 3-D Model Validation

Ideally, to validate the 3-D fuel cell model developed in this study, experimental measurements of concentration through the fuel cell are needed. The compact size of a typical lab fuel cell however, creates difficulty in obtaining a substantial amount of measurements at various points through the cell leading to uncertain experimental concentration profiles. Therefore, the most commonly used method of validating fuel cell models are performance curves, more specifically polarization curves. Experimental polarization curves are normally compared with those obtained from the mathematical models, though in some cases, polarization curves from different models are compared with each other.

While polarization curves do allow an adequate comparison between the model and experimental work, it must be noted that they are purely a means of validation (Berning et al., 2002) and it is difficult to obtain informative data from this result as model data can show good comparison with experimental data provided the correct equations are used to model the curve (see sections 4.2.4 and 4.2.5).

The present 3-D model was validated using experimental in-house performance data from the University of Cape Town (UCT) fuel cell laboratory. The experimental fuel cell was operated at a temperature of 80 °C and a pressure of 2 bar. Feed conditions to the cell were as follows, the stoichiometric ratio used on the anode side was 1.5 while the relative humidity was set to 80%, the cathode side stoichiometric feed ratio used was 2 while the relative humidity was set to 50%. To get an accurate comparison of the model result with the experimental data, all the operating parameters of the model were set to the exact values used in the experimental cell. These operating conditions are summarised at the bottom of Figure 10. The membrane thickness was also changed to a quarter of the value of the standard thickness used in order to match the experimental PEMFC used.

Comparing the model polarization curve with the experimental one shown in Figure 10, a good agreement is seen for low and moderate current densities (0 – 1 A/cm^2), however, a slight deviation is seen for current densities greater than 1 A/cm^2, this is due to liquid water being produced in the fuel cell which cannot be accounted for in a single phase model. The liquid water produced in the cell limits diffusion to the catalyst layer and therefore lowers the output voltage. Therefore from the validated results of the 3-D model it can be concluded that the model shows good fit for the lower to

moderate values of current density in the range of experimental data and a moderate fit for the higher values in the range. From this conclusion all concentration plots used will be for current densities in the 0 – 1 A/cm^2 range.

Since the 3-D model has also been validated for the lower to moderate current density range, concentration profiles from this model for the anode can be used to compare the concentration profiles for the anode obtained from the 1-D model.

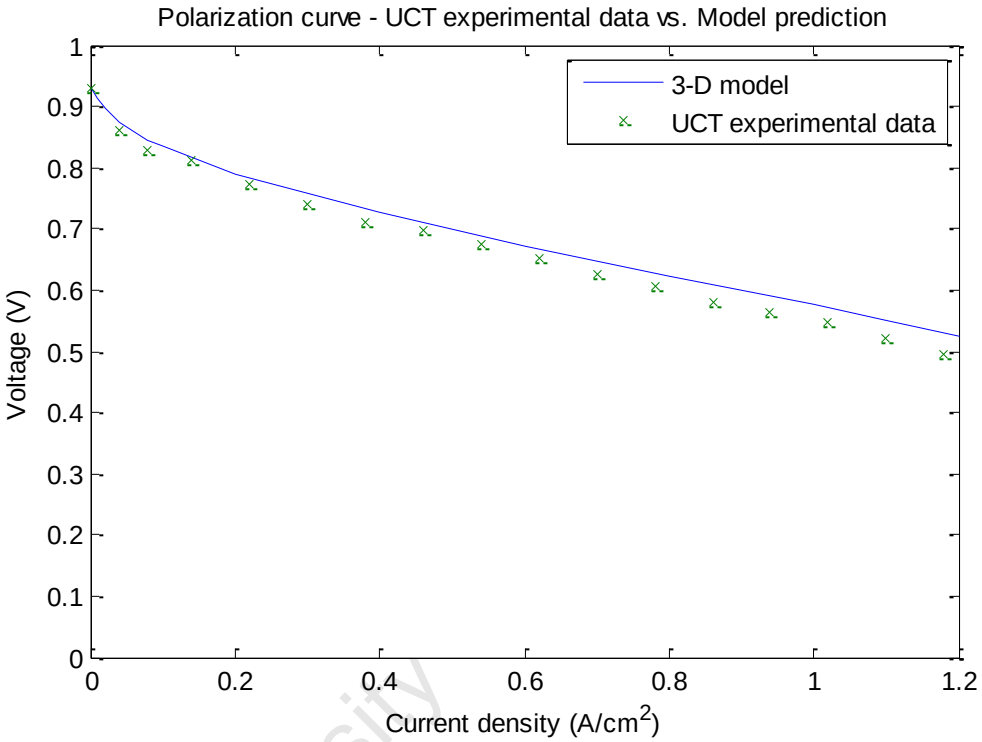

T = 80 ^{O}C, P = 2 Bar, s_{anode} = 1.5, $s_{cathode}$ = 2, RH_{anode} = 80 %, $RH_{cathode}$ = 50 %

Figure 10: 3-D model validation

5.2. 3-D Model Contour Plots and Concentration Profiles – Anode

The anode contour plots were obtained at 0.5 A/cm^2 and 1 A/cm^2 as shown in Figure 11 a) and b) respectively. As expected, the increase in current density causes more hydrogen to be consumed therefore lowering the concentration when comparing the initial and final values shown on the colour map for each plot. As can be seen from the figures, the hydrogen diffuses in an outward fashion from the flow channel into the GDL towards the solid land areas. The pattern of diffusion suggests that the concentration under the land areas is lower than under the channel areas and this effect becomes more visible at higher current densities. These observations agree with the results obtained by Berning et al. (2002) and Dawes et al. (2009) who both show similar concentration contour plot trends. Another observation is the significant drop in concentration along the length of the channel from the inlet. The two observations outlined above suggest that the concentration along the axes parallel to the membrane (x- and y-axis) are significant. This goes against the work

of Yi and Nguyen (1998) and Dutta et al. (2000) who showed that the concentration and current density vary slowly along the axes parallel to the PEM within the MEA. The implication of this result is that the assumption made in the development of the 1-D model of negligible concentrations along the x- and y- axis (see section 4.1.2) does not hold true.

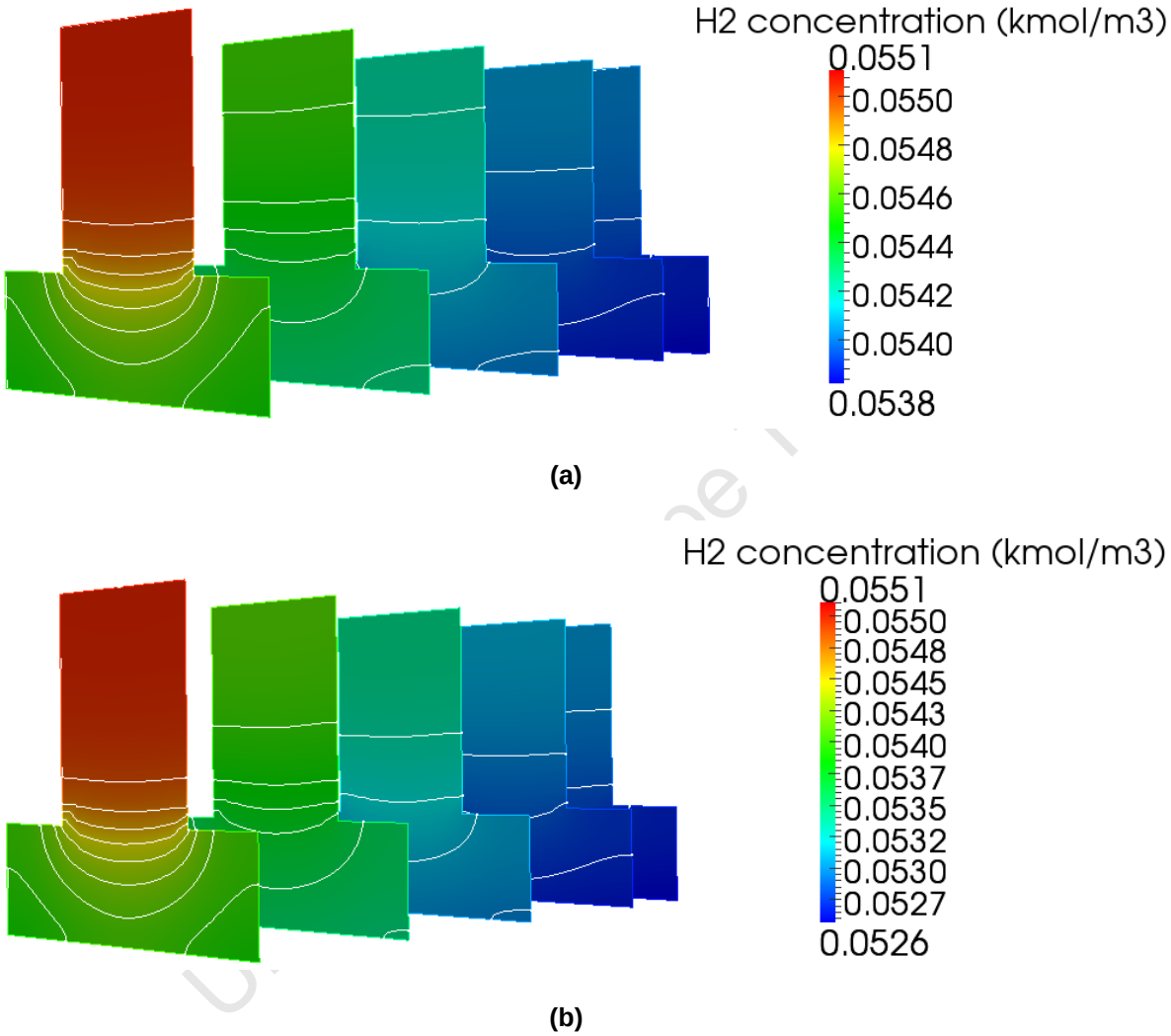

Figure 11: Hydrogen contour plots at the anode for a) 0.5 A/cm^2, b) 1 A/cm^2 current densities

Even though authors such as Falcao et al. (2011) have attempted to compare 1-D and 3-D models, the 3-D model results were illustrated as contour plots. Contour plots are a useful tool in analysing diffusion and depletion of reactants in terms of a spatial position in the cell, however, they are insufficient for comparing the 1-D and 3-D models. For this purpose, a plot of concentration against distance (z-axis) is required from the 3-D result in order to compare the two models adequately. It must be noted that the following procedure is only employed for a direct comparison between the two models. As such, most research conducted around 3-D CFD PEMFC simulations present results in the form of contour plots rather than x-y plots.

The domain to obtain the concentration against distance plot along the z-axis is that of a typical contour (slice) as shown in Figure 12. The height (z-axis distance) of the contour is incremented as shown in Figure 12. For each incremental height value, a concentration exists at each y-axis position, these concentrations are averaged over all nodes along the y-axis at a given incremental height to obtain an average concentration at a given incremental height. These data points are then graphed to obtain a plot of concentration vs. perpendicular distance from the membrane (z-axis) that can be used to perform a comparison between the 1- and 3-D models. The equation used to obtain the average concentration is shown in (5.1) where $\overline{C}_z$ is the average concentration at a given z increment, C_y is the concentration at a given y-axial position and N is the total number of nodes on the y-axis.

$$\overline{C}_z = \frac{\sum_{y=0}^{N} C_y}{N} \tag{5.1}$$

It must be noted that Figure 12 is just for illustrative purposes and in the actual results presented, the increments used along the z-axis are much smaller leading to a more accurate depiction of the concentration profile.

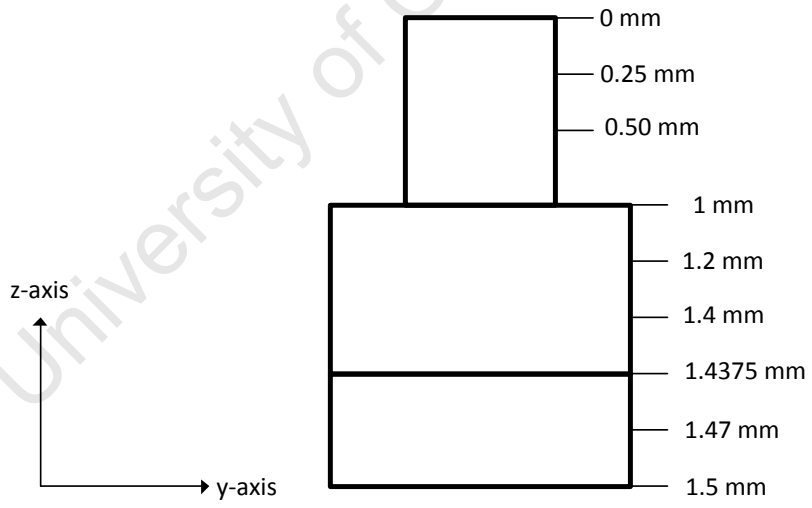

Figure 12: Typical contour from 3-D model showning y- and z-axes. (Note: increments are for illustrative purposes and are not to scale)

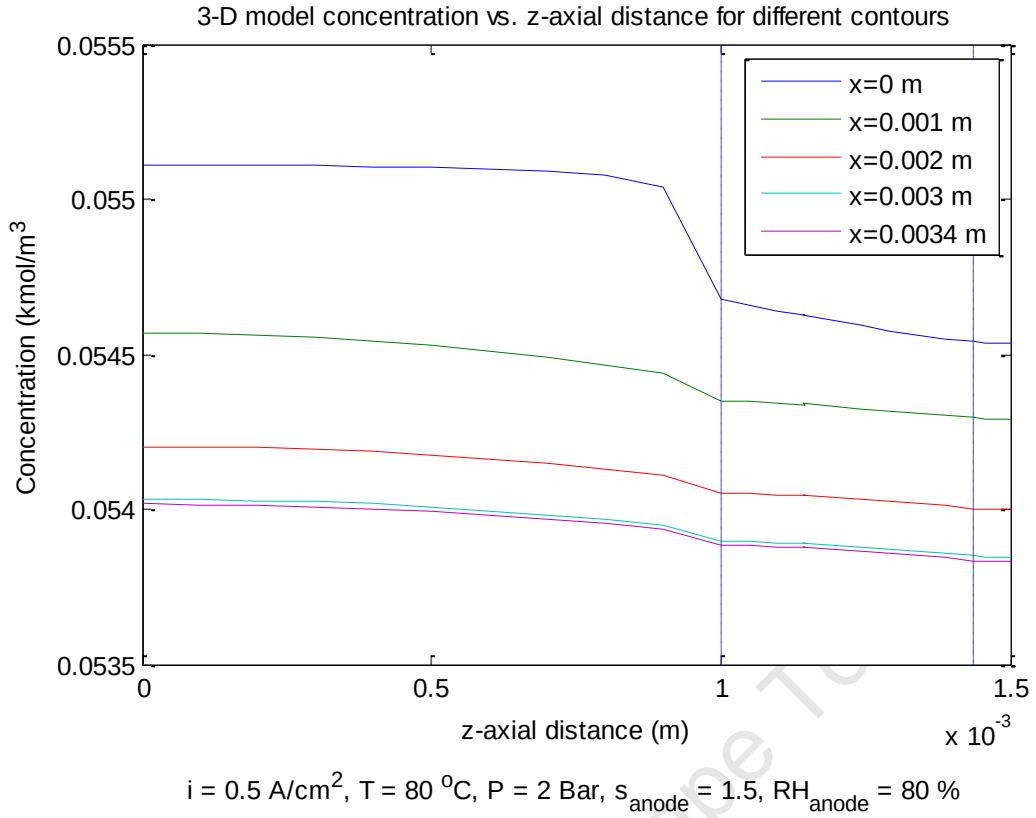

Figure 13: Concentration vs. z-axis distance for 3-D model at different contours for i = 0.5 A/cm^2

Figure 13 shows the 3-D model concentration profiles for the anode side of a PEMFC for the five contours presented in Figure 11 a). The vertical dashed lines separate the flow channel, GDL and catalyst layer. The drop seen in concentration in the flow channel at the interface between the channel and the GDL is due to the GDL being a porous medium. The profile for the first contour (x=0) shows a higher interfacial drop than the following contours, this can be explained considering that the concentration gradient in the flow channel in the first contour is much lower than the following contours leading to a higher interfacial drop. Referring to Figure 13, the profiles for the hydrogen concentration for the different contours decreases due to diffusion and convection in the flow channels. A further decrease in concentration due to predominantly diffusion is observed in the GDL. The change in the concentration gradient between the GDL and catalyst layer is negligible suggesting that diffusion is still dominating in the catalyst regime in the z-axis.

Looking more closely at the flow channel regime in Figure 13, the change in concentration in the z-axis in the flow channel is very low; this is expected as the major concentration gradient in the flow channels should be seen in the x-axis (parallel to the MEA) as this is the direction of flow. This is confirmed in Figure 14 which shows the change in concentration along the flow channel in the x-axis.

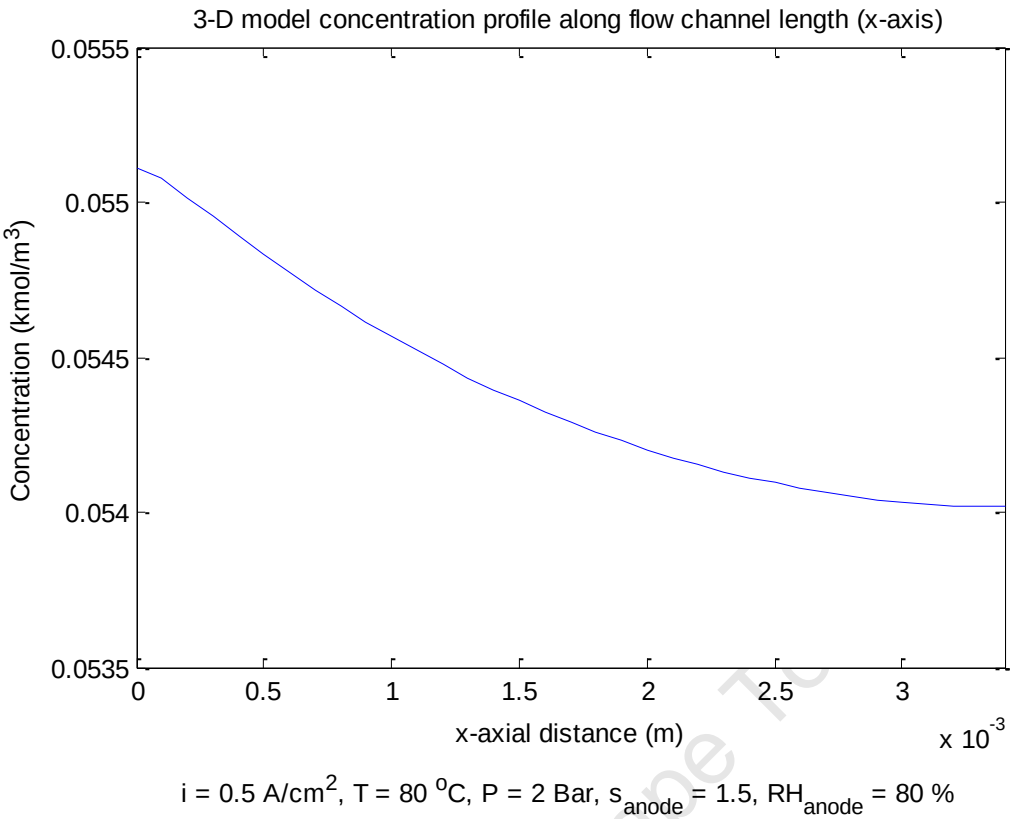

Figure 14: Concentration profile along the flow channel (x-axis) for 3-D model

For a proper comparison between the two models developed, the concentration values are normalised with the initial value on each of the contours (at z=0). This is also done to observe the effects along the channel to investigate the 1-D model assumption of negligible concentration gradients in the axis parallel to MEA within the porous medium when compared to those perpendicular to the MEA (refer to section 4.1.1). A normalised 3-D model concentration plot is shown in Figure 15. If the assumption made in the 1-D model regarding negligible concentration gradients parallel to the MEA holds true than the normalised profiles for each of the contours should be mapped one on top of the other when plotted. However, as can be seen from Figure 15, the normalised concentration plots from each contour do not map over one another suggesting that the gradients parallel to the MEA are significant. This strengthens the statement that the assumption made in the development of the 1-D model of negligible concentrations along the x- and y- axis does not hold true. Figure 15 also suggests that the reaction is higher at the initial parts of the cell closer to the inlet (considering profiles for x=0 m and x=0.001 m) when comparing those toward the end of the channel (x=0.003 m and x=0.0034 m). Figure 15 also suggest that at the regimes closer to the channel inlet, effects along the x-axis and y-axis are more significant as compared to the end of the channel. This can be seen graphically when comparing profiles for x=0.003 m and x=0.0034 m and observing that the two plots map one on top of the other.

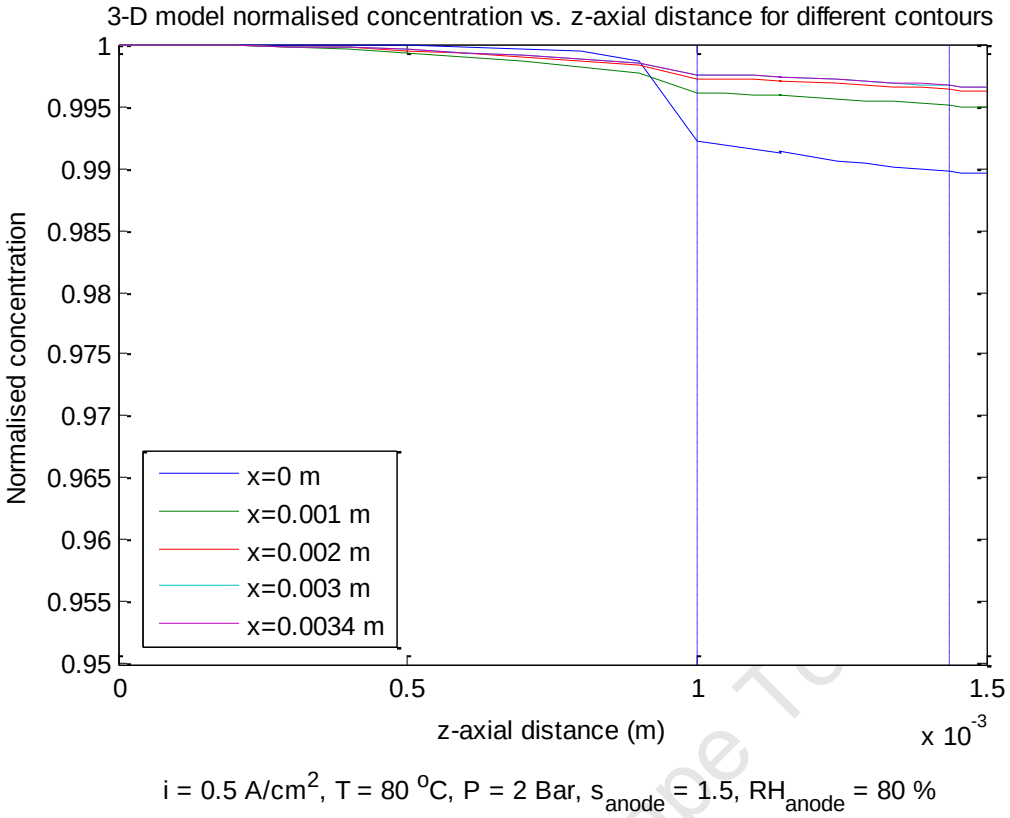

Figure 15: Normalised concentration vs. z-axis distance for 3-D model at different contours

5.3. 1-D and 3-D Model Comparison – Anode Side

The 1-D model concentration profile is plotted on the same axis used for the 3-D model profile for a current density of 0.5 A/cm^2 as shown in Figure 16. It is difficult to achieve a direct comparison for the reasons stated in the previous section, chief among which is the normalised concentration plots from the 3-D model for each contour do not map over one another suggesting that the gradients parallel to the MEA are significant. However, as can be seen from Figure 13, the trends of the profiles for each of the 3-D model contours follow the same pattern and therefore this section will compare the trend seen in the 1-D model with that of the 3-D model.

Looking at Figure 16, the 1-D and 3-D model calculate the same final value at the catalyst layer (at z = 1.5 x 10^{-3} m). This is a very important observation as it brings up a potential flaw in the use of polarization curves to validate fuel cell models. This method has been used extensively over the last 20 years by noted authors such as Dutta et al. (2000), Berning et al. (2002), Dawes et al. (2009) and Loo et al. (2011) to name but a few and has also been applied in the present work. Referring to the auxiliary equations in section 4.2.5 used to model the voltage losses, it is immediately clear that these equations only use the final concentration in the calayst layer for a specific current density to obtain the overpotentials at each of the loss regimes. This implies that the polarization curve is independent of the concentration profile through the various layers leading to the incorrect conclusion in many publications that lower dimension and higher dimension models are in good

agreement with each other because of validated polarization curve agreement between them. Therefore for a better comparison, the 1-D and 3-D model concentration profiles are directly compared.

As can be seen from Figure 16, the 1-D model shows a similar trend to the 3-D model in the flow channel with an almost negligible concentration gradient in the z-axis. Comparing the profiles in the GDL, we see that the gradients for both 1-D and 3-D models follow a linear pattern though the gradient for the 1-D model shows a more steep slope than the 3-D model contours. This can be explained by considering that each contour in the 3-D model only illustrates a portion (slice) of the entire cell whereas the 1-D model considers the entire domain leading a steeper gradient. If an average concentration in the GDL along the z-axis is considered, the result would yield a gradient similar to that of the 1-D model. The 1-D model predicts a much steeper slope than that of the GDL which is expected as the catalyst layer was modelled considering both diffusion and reaction for the 1-D model. However, when comparing the catalyst layer trends for both models, it is clear that quite a significant difference is observed with the 3-D model showing very little/no change in gradient from the GDL to the catalyst layer which was explained in section 5.2. The reason for this was found to be that the reaction was dominant along the x-axis rather than in the z-axis as shown in Figure 17 which illustrates the concentration change in the catalyst layer along the x-axis.

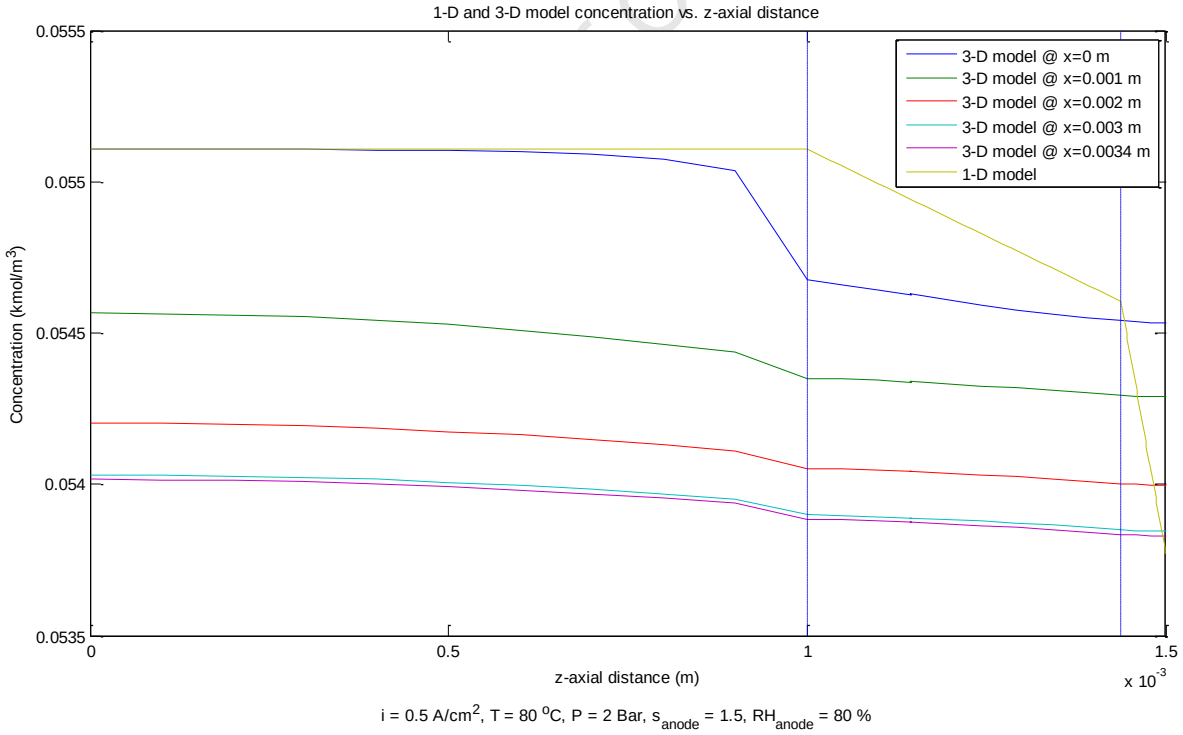

Figure 16: 1-D and 3-D model concentration vs. z-axis distance at i = 0.5 A/cm2

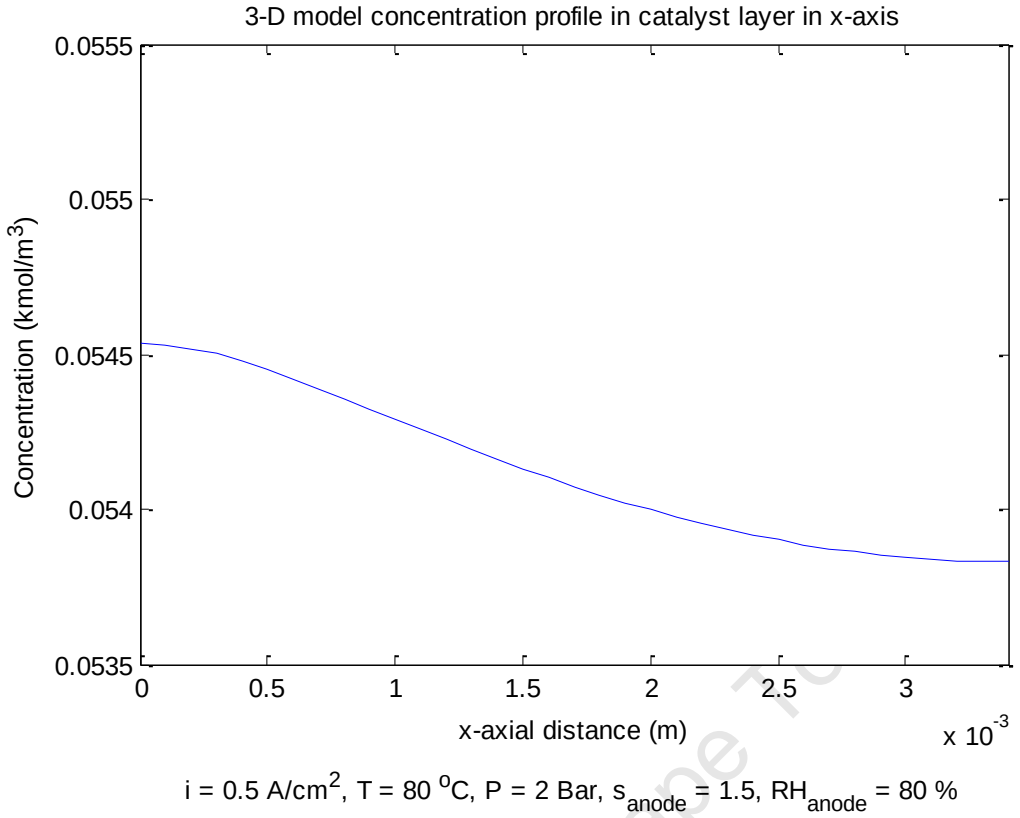

Figure 17: 3-D model concentration profile in catalyst layer along x-axis

5.4. 3-D Model Contour Plots - Cathode

While the anode has been investigated in quite some detail, the oxygen distribution in the cathode side of the cell is also of importance. Water is produced as the by-product of the reaction and even though this model is a single phase system, the water distribution in the cathode side of the cell is investigated.

Figure 18 illustrates the oxygen contour plots at 0.5 A/cm^2 (top) and 1 A/cm^2 (bottom). Oxygen diffuses from the flow channel into the GDL in an outward fashion towards the solid land areas of the cell. The concentration decreases significantly as the reactant gas diffuses into the GDL. The effect of the land areas also becomes more pronounced at higher current densities with a higher rate of oxygen depletion being seen. The latter observation makes senses since at higher current densities, the gas feed is being consumed at a higher rate. The oxygen concentration decreases along the channel as well which can be seen in Figure 18 by the decrease of the initial concentration on each of the contours. These obseravations are agreeable with those seen by Berning et al. (2002). However, since the model developed by Berning et al. (2002) modelled liquid water formation, the observations seen at higher current densities vary slightly due to the lack of liquid water being present in the current model. Liquid water causes oxygen transport inhibition therefore lowering the concentration of oxygen in the GDL and catalyst layers.

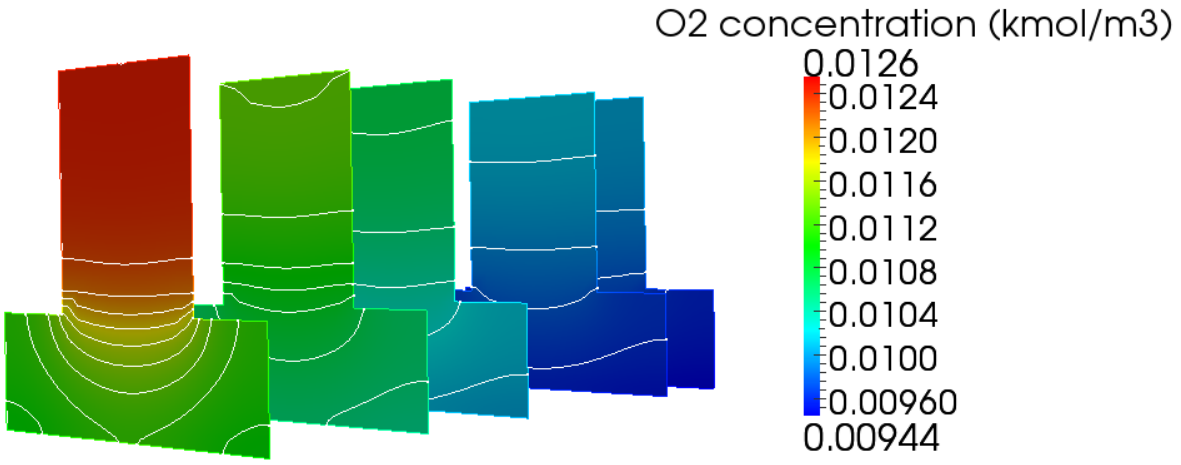

(a)

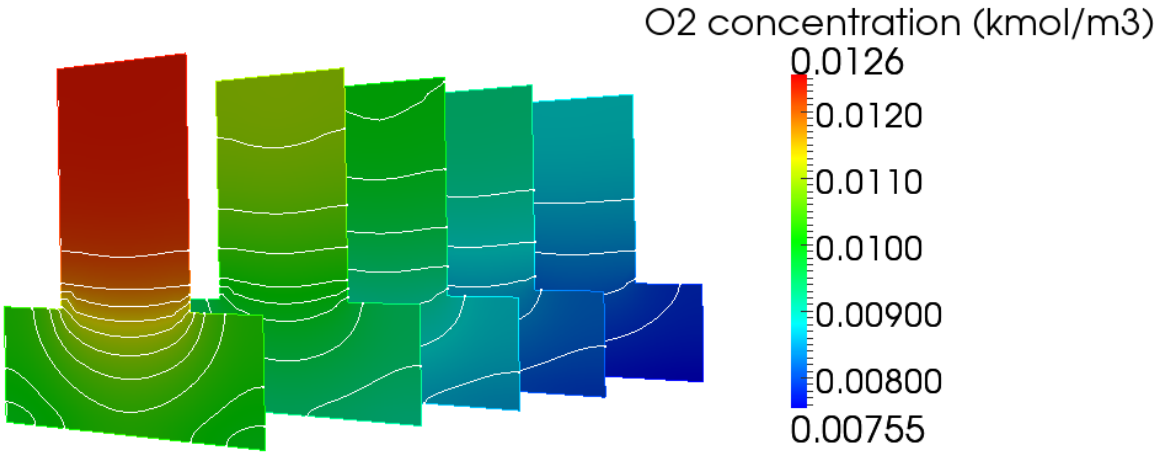

(b)

Figure 18: Oxygen contour plots at the cathode for a) 0.5 A/cm^2, b) 1 A/cm^2 current densities

Finally, we consider the water distribution on the cathode side. Since the 3-D model is a single phase system, the distribution obtained is only of water vapour but this will still allow for a general idea of where in the cathode side liquid water has the highest chance of forming.

The water vapour distribution at current densities of 0.5 A/cm^2 (top) and 1 A/cm^2 (bottom) is presented in Figure 19, similar to those presented for hydrogen and oxygen. As expected, the water vapour concentration increases along the channel due to oxygen depletion (due to reaction) and water transport from the anode to the cathode through the membrane. Comparing Figure 19 a) and b), the water concentration increases with increasing current density, this is expected as, more water is formed due to an increased reaction rate as well as a higher water transport from the anode to the cathode by electro-osmotic drag through the membrane. At higher current densities, the increased rate of water transport from the anode to the cathode will cause the resistance to proton transfer through the membrane to increase due to a depleted water concentration at the anode side

of the membrane. This increase resistance to protonic conductivity will in turn increase the ohmic losses discussed earlier.

As can be seen from the figure, most of the water is seen under the solid land areas of the channel within the GDL and catalyst layers, this suggests that condensation of water vapour might occur in these areas, a two-phase flow model is required in order to confirm this.

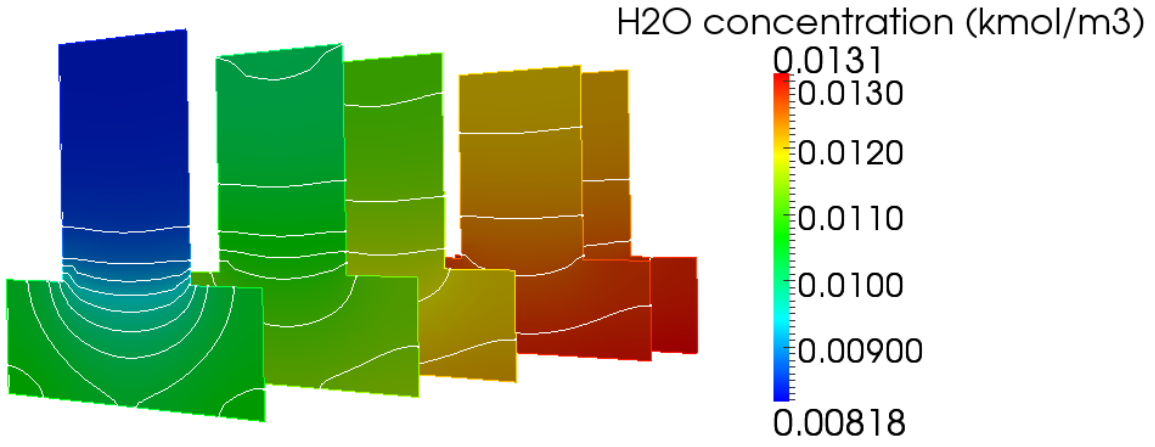

(a)

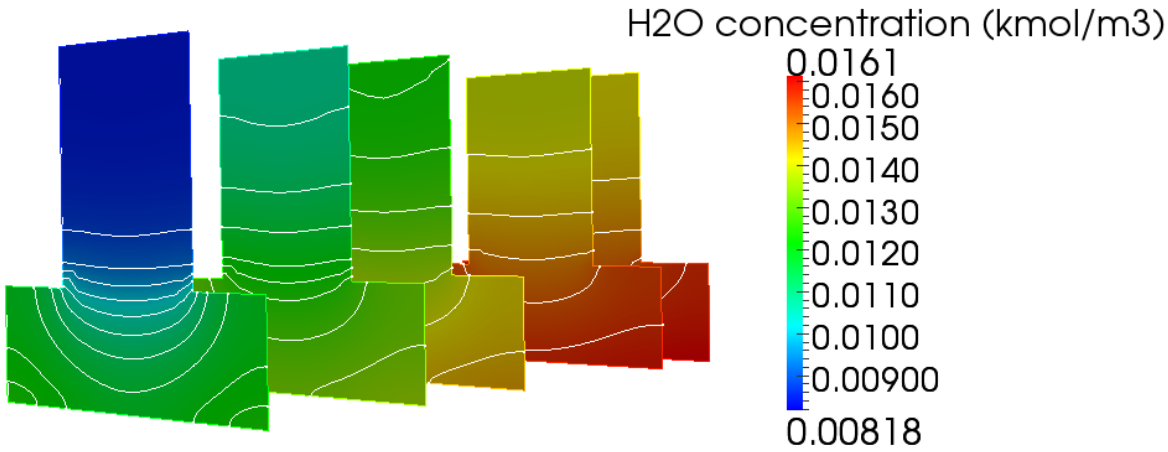

(b)

Figure 19: Water vapour contour plots at the cathode for a) 0.5 A/cm2, b) 1 A/cm2 current densities

6. CONCLUSIONS AND RECOMMENDATIONS

Fuel cell technology has the potential to reduce the global demand for fossil fuels and by extension the global carbon footprint. However, further research is required to make this technology commercially viable. Modelling allows phenomena difficult to study experimentally, such as species transport, to be investigated. It also allows parameters such as GDL thickness, porosity, membrane conductivity and flow channel dimensions to be tested in a cost effective manner. While fuel cell modelling provides a better understanding of the complex phenomena within the cell during operation, uncertainty is associated with model accuracy. Complex CFD models are available but tend to have large simulation times rendering them unfeasible in any rigorous fuel cell design optimisation. Further insight into model accuracy can be achieved by detailed comparison between a lower and higher dimension mathematical PEMFC model.

The objective of the present investigation was to determine the minimum dimension of a mathematical model that can accurately simulate processes occurring within a proton exchange membrane fuel cell (PEMFC). To this end, a comprehensive 3-D steady state, single phase, isothermal full cell PEMFC model was developed along with a simple 1-D steady state, single phase, isothermal anode side model. A successful study involved the proof of assumptions made in the development of the 1-D model by comparing its results with that of the 3-D model as well as a significant saving when comparing the simulation times of the two models.

When comparing the simulation time of the two models, the estimated simulation time for the 3-D model was 10-20 minutes depending on processor power while the 1-D model took less than one minute to run. This provides a 95% time saved when the 1-D model is used instead of the 3-D model. The 3-D model results were validated using experimental data obtained from the UCT HySA/Catalysis fuel cell laboratory. The model showed good agreement with the experimental data for low and moderate current densities (0 – 1 A/cm^2), however, a slight deviation is seen for current densities greater than 1 A/cm^2, this is due to liquid water being produced in the fuel cell which cannot be accounted for in a single phase model. The implication of this is that the results obtained by the variation of different parameters are only reliable in the low to moderate current density range. Therefore, to get accurate data at higher current densities, the model must be further developed to account for two-phase flow by modelling the liquid water saturation in the catalyst layers and GDL.

Based on the above results from validation, the current density range that was used to compare the two models was chosen between the low and moderate range. The results of the normalised 3-D model concentration profiles for hydrogen at the anode showed that, in contrast with several papers in the literature, concentration through the GDL and catalyst layer in x- and y-axis were significant. This was proved when considering the concentration of hydrogen in the anode catalyst layer. A much more significant decrease in concentration due to reactant consumption was seen along the x-axis than along the z-axis which showed a negligible change in concentration gradient from the GDL to the

catalyst layer. This is a key finding as it questions the validity of 1-D models for rigorous fuel cell parameter testing. This is because concentration gradients are significant in at least two of the three dimensions while the 1-D model only assumes negligible concentration gradients in all but one dimension.

When comparing the results of the 1-D and 3-D model concentration profiles, it was noted that both models predict the same final concentration at the catalyst layer which brought up a flaw in the use of polarization curves to validate and compare different fuel cell models as the predicted polarization curves are independent of the concentration profile through the cell. However, because the intermediate concentrations in the two models differ, the 1-D model cannot be fully trusted and therefore alternatives must be developed to account for transport along the channel (x-axis) as well as perpendicular to the membrane (z-axis).

While the developed 1-D model provided a 95% saving in simulation time, results from the 3-D model showed concentration gradients to be significant along the x-axis. The implication of this result is that the 1-D model alone is not sufficient to accurately model phenomena within a PEMFC during operation. This is because the 1-D model makes the assumption that the concentration gradient is only significant in one of the three axes of interest. The 3-D model was also validated over a low to moderate current density range due to the model being single phase and not accounting for liquid water formation. The result of this is data obtained from the model is only valid in this range of current densities. Therefore, future work in fuel cell modelling must focus on the development of a more accurate 1-D model to account for transport along the channel (x-axis) as well as perpendicular to the membrane (z-axis). Such a model is known as a 1-D + 1-D model. This model will allow a more accurate representation of the transport phenomena within a PEMFC during operation and will be more comparable to a 3-D model. The 1-D and 3-D model must also be built upon to account for two-phase flow to obtain accurate data at high current densities.

REFERENCES

Al-Baghdadi, M.A.R.S. & Al-Janabi, H.A.K.S., 2007. Parametric and optimization study of a PEM fuel cell performance using three-dimenisonal computational fluid dynamics model. *Renewable Energy*, 32(7), pp.1077-101.

Barbir, F., 2005. *PEM Fuel Cells: Theory and Practice*. 1st ed. New York: Elsevier Academic Press.

Barbir, F., 2006. PEM fuel cells. In N. Sammes, ed. *Fuel Cell Technology - Reaching towards commercialization*. 1st ed. London: Springer-Verlag. pp.31-25.

Bard, A. & Faulkner, L., 2001. *Electrochemical Methods. Fundamentals and Applications*. 2nd ed. New York, NY.: John Wiley and Sons.

Baschuk, J.J. & Li, X., 2004. A general formulation for a mathematical PEM fuel cell model. *Journal of Power Sources*, 142, pp.134-53.

Benziger, J. et al., 2005. Water flow in the gas diffusion layer of PEM fuel cells. *Journal of Membrane Science*, 261, pp.98-106.

Bernardi, D.M. & Verbrugge, M.W., 1991. Mathematical model of a gas diffusion electrode bonded to a polymer electrolyte. *AIChE Journal*, 37(8), pp.1151-63.

Berning, T., 2002. *Three-Dimensional computational analysis of transport phenomena in a PEM fuel cell*. Doctoral Thesis. Victoria: University of Victoria University of Victoria.

Berning, T. & and Djilali, N., 2003. A 3D, Multiphase, Multicomponent Model of the Cathode and Anode of a PEM Fuel Cell. *Journal of the Electrochemical Society*, 150(12), pp.A1589-98.

Berning, T., Lu, D.M. & Djilali, N., 2002. Three-dimensional computational analysis of transport phenomena in a PEM fuel cell. *Journal of Power Sources*, 106, pp.284-94.

Bird, R.B., Stewart, W.E. & and Lightfoot, E.N., 2002. *Transport Phenomena*. 2nd ed. New York, NY.: John Wiley and Sons Inc.

Caillard, A. et al., 2005. Deposition and diffusion of platinum nanoparticles in porous carbon assisted by plasma sputtering. *Surface & Coatings Technology*, 200, pp.391-94.

Cheddie, D. & Munroe, N., 2005. Review and comparison of approaches to proton exchange membrane fuel cell modeling. *Journal of Power Sources*, 147, pp.72-84.

Chen, F. et al., 2004. Transient behavior of water transport in the membrane of a PEM fuel cell. *Journal of Electroanalytical Chemistry*, 566, pp.85-93.

Das, P.K., 2010. *Transport phenomena in cathode catalyst layer of PEM fuel cells*. Doctoral thesis. Ontario: University of Waterloo University of Waterloo.

Dawes, J.E., Hanspal, N.S., Family, O.A. & Turan, A., 2009. Three-dimensional CFD modelling of PEM fuel cells: An investigation into the effects of water flooding. *Chemical Engineering Science*, 64, pp.2781-94.

Dinçer, İ. & Rosen, M.A., 2007. Exergy Analysis of Fuel Cell Systems. In *Exergy: energy, environment, and sustainable development*. 1st ed. Elsevier. p.306.

Dullien, F.A.L., 1979. *Porous Media, Fluid Transport and Pore Structure*. London: Academic Press Inc.

Dutta, S., Shimpalee, S. & Van Zee, J.W., 2000. Three-dimensional numerical simulation of straight channel PEM fuel cells. *Journal of Applied Electrochemistry*, 30, p.135.

Faghri, A. & and Zhang, Y., 2006. *Transport Phenomena in Multiphase Systems*. Elsevier, Academic Press.

Falcao, D.S. et al., 2009. Water transport through a PEM fuel cell: a one-dimensional model with heat transfer effects. *Chemical Engineering Science*, 64(9), pp.2216-25.

Falcao, D.S. et al., 2011. 1D and 3D numerical simulations in PEM fuel cells. *International Journal of Hydrogen Energy*, 36, pp.12486-98.

Geankoplis, C.J., 2003. *Transport Processes and Separation Process Principles*. 4th ed. New Jersey: Prentice Hall.

Gurau, V., Hongtan, L. & Kakaç, S., 1998. Two-dimensional model for proton exchange memberane fuel cells. *AIChE Journal*, 44(11), pp.2410-22.

Haraldsson, K. & Wipke, K., 2004. Evaluating PEM fuel cell system models. *Journal of Power Sources*, 126, pp.88-97.

Hashemi, F., Rowshanzamir, S. & Rezakazemi, M., 2012. CFD simulations of PEMF fuel cell performance: Effect of straight and serpentine flow fields. *Mathematical and Computer Modelling*, 55, pp.1540-57.

He, W., Yi, J. & Nguyen, T.V., 2000. Two-phase flow model of the cathode of PEM fuel uusing interdigitated flow fields. *AIChE Journal*, 46(10), p.2053–2064.

IEA, 2011. *Key world energy statistics*. Annual report. Paris: International Energy Agency International Energy Agency.

J., P. & Lee, S.J., 2006. Numerical simulation of proton of proton exchange membrane fuel cells at high operating temperature. *Journal of Power Sources*, 162, pp.1182-91.

Koido, T., Furusawa, T. & Moriyama, K., 2008. An approach to modeling two-phase transport in the gas diffusion layer of a proton exchange membrane fuel cell. *Journal of Power Sources*, 175, pp.127-36.

Kornyshev, A.A. & Kulikovsky, A.A., 2001. Characteristic length of fuel and oxygen consumption in feed channels of polymer electrolyte fuel cells. *Electrochimica Acta*, 46, p.4389–4395.

Kornyshev, A.A., Kuznetsov, A.M., Spohr, A.M. & Ulstrop, J., 2003. Kinetics of proton transport in water. *The Journal of Physical Chemisty B*, 107(15), pp.3351-66.

Kreuer, K.D., Rabenau, A. & Weppner, W., 1982. Vehicle mechanism, a new model for the interpretation of the conductivity of fast proton conductors. *Angew Chemie International Edition*, 21(3), pp.208-09.

Kulikovsky, A.A., 2002. The voltage-current curve of a polymer electrolyte fuel cell: Exact and fitting equations. *Electrochemistry Communications*, 4(11), pp.845-52.

Kulikovsky, A.A., 2003. Quasi-3D modeling of water transport in polymer electrolyte fuel cells. *Journal of Electrochemical Society*, 150(11), pp.A1423-39.

Liu, X., Tao, W., Li, Z. & He, Y., 2006. Three-dimensional transport model of PEM fuel cell with straight flow channels. *Journal of Power Sources*, 158, pp.25-35.

Loo, K.H. et al., 2011. Derivation of a fast mathematical nodel of PEM fuel cell with two-phase water transport. *IEEE Transactions on Energy Conversion*, 26(1), pp.216-26.

Lum, K.W. & McGuirk, J.J., 2005. Three-dimensional model of a complete polymer electrolyte membrane fuel cell-model formulation, validation and parametric studies. *Journal of Power Sources*, 143, pp.103-24.

McCain, B.A., Stefanopoulou, A.G. & Siegel, J.B., 2010. Controllability and observability analysis of the liquid water distribution inside the fas diffusion layer of a unit fuel cell model. *Jornal of Dynamic Systems, Measurement, and Control*, 132, pp.1-8.

McMahon, A.M., 2009. *Modelling the flow behaviour of gas bubbles in a bubble column*. MSc (Eng.) Thesis Project. Cape Town: University of Cape Town University of Cape Town.

Mehta, V. & Cooper, J.S., 2003. Review and analysis of PEM fuel cell design and manufacturing. *Journal of Power Sources*, 114, pp.32- 36.

Min, C.H., 2009. Performance of a proton exchange membrane fuel cell with stepped flow field design. *Journal of Power Sources*, 186, pp.370-76.

Min, C.H., 2010. A novel three-dimensional, two-phase and non-isothermal numerical model for proton exchange membrane fuel cell. *Journal of Power Sources*, 195, pp.1880-87.

Moudgil, H.K., 2010. *Textbook of Physical Chemistry*. New Delhi: PHI Learning Private Limited.

Mukherjee, P.P. & Wang, C.Y., 2007. Direct numerical simulation modeling of bilayer cathode catalyst layers in polymer electrolyte fuel cells. *Journal of Electrochemical Society*, 154(11), pp.B1121-31.

Nam, J.H. & Kaviany, M., 2003. Effective Diffusivity and Water-Saturation Distribution in Single- and Two-Layer PEMFC Diffusion Medium. *International Journal of Heat and Mass Transfer*, 46(24), pp.4595-611.

Okada, T., Xie, G. & Meeg, M., 1998. Simulation for water management in membranes for polymer electrolyte fuel cells. *Electrochimica Acta*, 43, pp.2141-55.

Oliveira, V.B., Rangel, C.M. & Pinto, A.M.F.R., 2011. One-dimensional and non-isothermal model for a passive DMFC. *Journal of Power Sources*, 196, p.8973– 8982.

Parthasarathy, A., Srinivasan, S., Appleby, A. & Martin, C., 1992. Temperature-dependence of the electrode-kinetics of oxygen reduction at the platinum nafion interface - A microelectrode investigation. *Journal of the Electrochemical Society*, 139, p.2530–2537.

Pollet, B.G., 2010. The use of ultrasound for the fabrication of fuel cell materials. *International Journal of Hydrogen Energy*, 74, pp.324-36.

Schmickler, W., 1996. *Interfacial Electrochemistry*. New York: Oxford University Press.

Shimpalee, S., Dutta, S., Lee, W.K. & Van Zee, J.W., 1999. Effect of humidity on PEM fuel cell performance Part II: Numerical simulation.. *ASME-Publications-HTD*, 364(1), pp.367-74.

Siegel, C., 2008. Review of heat and mass transfer modeling in polymer-electrolyte-membrane (PEM) fuel cells. *Energy*, 33, pp.1331-52.

Siegel, N.P., Ellis, M.W., Nelson, D.J. & M.R., v.S., 2003. Single domain PEMFC model based on agglomerate catalyst geometry. *Journal of Power Sources*, 115, pp.81-89.

Spiegel, C., 2008. *PEM fuel cell modeling and simulation using MATLAB*. Elsevier, Academic Press.

Springer, T.E., Zawodzinski, T.A. & Gottesfeld, S., 1991. Polymer Electrolyte Fuel Cell Model. *Journal of the Electrochemical Society*, 138(8), pp.2334-42.

Srinivasan, S., 2006. *Fuel Cells: From Fundamentals to Applications*. New York: Springer.

Standaert, F., Hemmes, L. & Woudstra, N., 1996. Analytical fuel cell modeling. *Journal of Power Sources*, 63, pp.212-34.

Suh, D. & Park, S., 2011. Transport phenomena in proton exchange membrane fuel cells and over-potential distribution of membrane electrode assembly. *International Journal of Thermal Sciences*, 51, pp.31-41.

Taylor, R. & Krishna, R., 1993. *Multicomponent Mass Transfer*. John Wiley & Sons.

Um, S., Wang, C.Y. & Chen, K.S., 2000. Computational fluid dynamics of proton exchange membrane fuel cells. *Journal of Electrochemical Society*, 147(12), pp.4485-93.

University of Cape Town Fuel Cell Lab, U., 2012. *PEMFC preparation and testing methods*. Internal document. Cape Town: University of Cape Town.

van Bussel, H., Koene, F. & Mallant, R., 1998. Dynamic model of solid polymer fuel cell water management. *Journal of Power Sources*, 71, pp.218-22.

Verbrugge, M.W., 1994. Selective Electrodeposition of Catalyst within Membrane-Electrode Structures. *Joural of Electrochmistry*, 141(1), pp.46-53.

Verbrugge, M. & Hill, R., 1990. Ion and solvent transport in ion-exchange membranes. 1. A Macrohomogeneous Mathematical Model. *Journal of the Electrochemical Society*, 137(3), pp.886-93.

Wang, C.Y. & Cheng, P., 1996. A multiphase mixture model for multiphase, multicomponent transport in capillary porous media. 1. Model development. *International Journal of Heat and Mass Transfer*, 39(17), pp.3607-18.

Wang, Y. et al., 2010. A review of polymer electrolyte membrane fuel cells: Technology, applications, and needs on fundamental research. *Applied Energy*, 88, pp.981-1007.

Wang, Z.H., Wang, C.Y. & Chen, K.S., 2001. Twp-phase flow and transport in the air cathode of proton exchange membrane fuel cells. *Journal of Power Sources*, 94, pp.40-50.

Yi, J.S. & Nguyen, T.V., 1998. An along-the-channel model for proton exchange membrane fuel cells. *Journal of Electrochemical Society*, 145(4), p.1149.

Yuan, X.-Z., Song, C., Wang, H. & Zhang, J., 2010. *Electrochemical Impedance Spectroscopy in PEM Fuel Cells: Fundamentals and Applications*. London: Springer.

Zhang, J., 2008. *PEM Fuel Cell Electrocatalysts and Catalyst Layers: Fundamentals and Applications*. London: Springer.

APPENDICES

APPENDIX A – DERIVATIONS

A.1. Navier Stokes Equations

In the following appendix, the mass and momentum balances are derived from first principles for incompressible fluid flow for a 3-D system. Derivations were adapted and modified from McMahon (2009) and Geankoplis (2003).

Continuity Equation

A typical fluid element is shown in Figure A 1, the derivation of the continuity equation will be based on this figure. The law of conservation of mass states:

(rate of mass into fluid element) - (rate of mass out of fluid element) = (accumulation of mass in fluid element) (A.1)

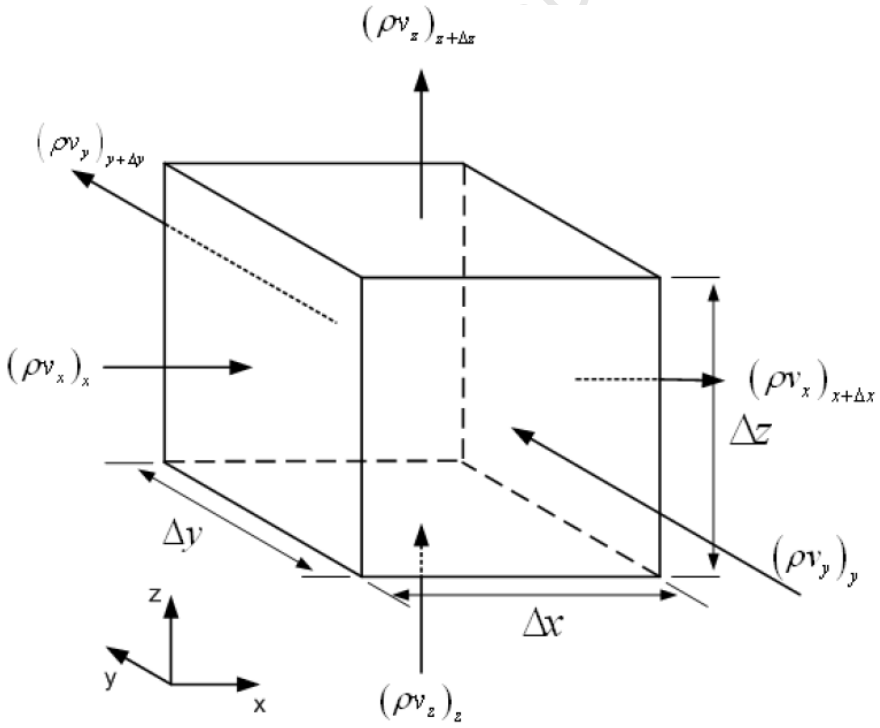

Figure A 1: Mass flux in and out of a standard cubic fluid element

Considering the x-direction, the terms in (A.1) above are defined as follows:

Rate of mass into fluid element = $(\rho u_x)_x \Delta y \Delta z$

Rate of mass out of fluid element = $(\rho u_x)_{x+\Delta x} \Delta y \Delta z$

Accumulation of mass in fluid element = $\frac{\delta\rho}{\delta t}\Delta x\Delta y\Delta z$

The terms for the y- and z-directions are obtained in a similar fashion using Figure A 1. Summation of all the expressions and dividing through by $\Delta x\Delta y\Delta z$ leads to (A.2).

$$\frac{(\rho u_x)_x-(\rho u_x)_{x+\Delta x}}{\Delta x}+\frac{(\rho u_y)_y-(\rho u_y)_{y+\Delta y}}{\Delta y}+\frac{(\rho u_z)_z-(\rho u_z)_{z+\Delta z}}{\Delta z}=\frac{\delta\rho}{\delta t} \qquad \text{(A.2)}$$

Taking the limit of (A.2) as Δx , Δy and Δz approach zero yields the general mass balance equation shown in (A.3).

$$\frac{\delta\rho}{\delta t}=-\left[\frac{\delta(\rho u_x)}{\delta x}+\frac{\delta(\rho u_y)}{\delta y}+\frac{\delta(\rho u_z)}{\delta z}\right]=-\left(\nabla\cdot\rho\vec{u}\right) \qquad \text{(A.3)}$$

(A.3) can be simplified further if the fluid is incompressible (constant density) and the system of interest is at steady state as illustrated in (A.4). (A.4) defines the continuity equation.

$$\left[\frac{\delta u_x}{\delta x}+\frac{\delta u_y}{\delta y}+\frac{\delta u_z}{\delta z}\right]=\nabla\cdot\vec{u}=0 \qquad \text{(A.4)}$$

Momentum Balance

Newton's second law - "Sum of the forces acting on a fluid element equals he rate of change of momentum of that fluid element."

Newton's second law is the starting point of the momentum balance derivation, the law is defined above and is defined as in equation as shown in (A.5). This can also be defined as shown in (A.6).

(rate of momentum into fluid element) - (rate of momentum out of fluid element) + (sum of forces acting on system) = (accumulation of momentum in fluid element) (A.5)

$$\sum\vec{F}=\frac{d\vec{P}}{dt} \qquad \text{(A.6)}$$

Considering just the x-axis, the terms in (A.5) are defined as follows:

Rate of momentum into element = $\left(\rho u_x u_x\right)_x\Delta y\Delta z+\left(\rho u_y u_x\right)_y\Delta x\Delta z+\left(\rho u_z u_x\right)_z\Delta x\Delta y$

Rate of momentum out of element = $\left(\rho u_x u_x\right)_{x+\Delta x}\Delta y\Delta z+\left(\rho u_y u_x\right)_{y+\Delta y}\Delta x\Delta z+\left(\rho u_z u_x\right)_{z+\Delta z}\Delta x\Delta y$

Accumulation of mass in element = $\frac{\delta(\rho u_x)}{\delta t}\Delta x\Delta y\Delta z$

Replacing the terms into (A.5) and dividing through by $\Delta x\Delta y\Delta z$ and taking the limit as Δx, Δy and Δz approach zero yields (A.7), the term in square brackets defines the net momentum flow in the x-direction.

$$\frac{\delta(\rho u_x)}{\delta t} = -\left[\frac{\delta(\rho u_x u_x)}{\delta x} + \frac{\delta(\rho u_y u_x)}{\delta y} + \frac{\delta(\rho u_z u_x)}{\delta z}\right] + \sum F_x \tag{A.7}$$

Applying the product rule to (A.7) gives us its expanded form.

$$\begin{aligned}\rho\frac{\delta u_x}{\delta t} + u_x\frac{\delta \rho}{\delta t} = &-\left[\left(u_x\frac{\delta(\rho u_x)}{\delta x} + \rho u_x\frac{\delta u_x}{\delta x}\right)\right] \\ &-\left[\left(u_x\frac{\delta(\rho u_y)}{\delta y} + \rho u_y\frac{\delta u_x}{\delta y}\right) + \left(u_x\frac{\delta(\rho u_z)}{\delta y} + \rho u_z\frac{\delta u_x}{\delta y}\right)\right] + \sum F_x\end{aligned} \tag{A.8}$$

Multiplying (A.3) by the velocity in the x-direction (u_x) and substituting the resulting equation into (A.8) and rearranging gives the sum of the forces acting on the fluid in the x-direction as shown in (A.9).

$$\rho\left(\frac{\delta u_x}{\delta t} + u_x\frac{\delta u_x}{\delta x} + u_y\frac{\delta u_x}{\delta y} + u_z\frac{\delta u_x}{\delta z}\right) = \sum F_x \tag{A.9}$$

Applying the definition of the total derivative to (A.9) gives us (A.10).

$$\rho\frac{Du_x}{Dt} = \sum F_x \tag{A.10}$$

In a similar fashion, the sum of the forces acting on the fluid in the y and z-directions can be obtained, the results of which are shown in (A.11) and (A.12).

$$\rho\frac{Du_y}{Dt} = \sum F_y \tag{A.11}$$

$$\rho\frac{Du_z}{Dt} = \sum F_z \tag{A.12}$$

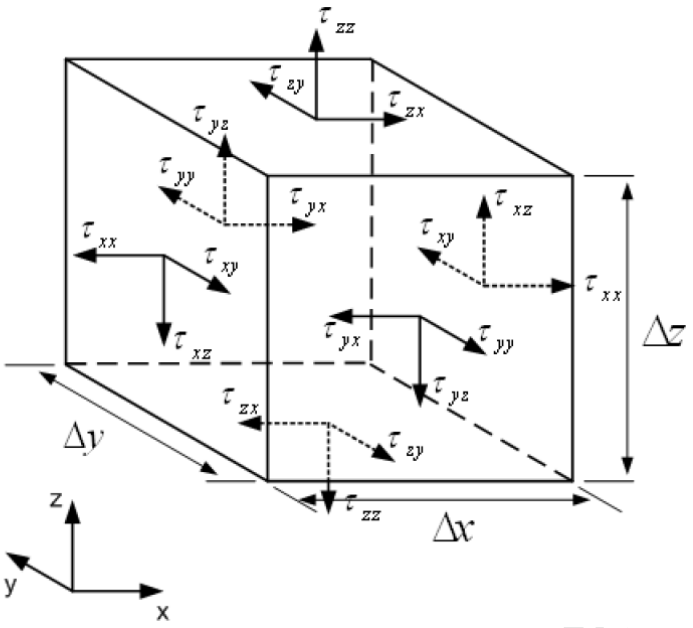

Figure A 2: Stress components on a standard cubic fluid element

Two types of forces act on a fluid element; these are surface and body forces. Surface forces include pressure and viscous forces while body forces include centrifugal, gravitational, Coriolis and electromagnetic forces.

Referring to Figure A 2, τ_{ij} is the viscous stress where the subscript *i* denotes the surface normal and the subscript *j* denotes the stress direction. The term τ_{ii} defines the total normal stress excluding pressure.

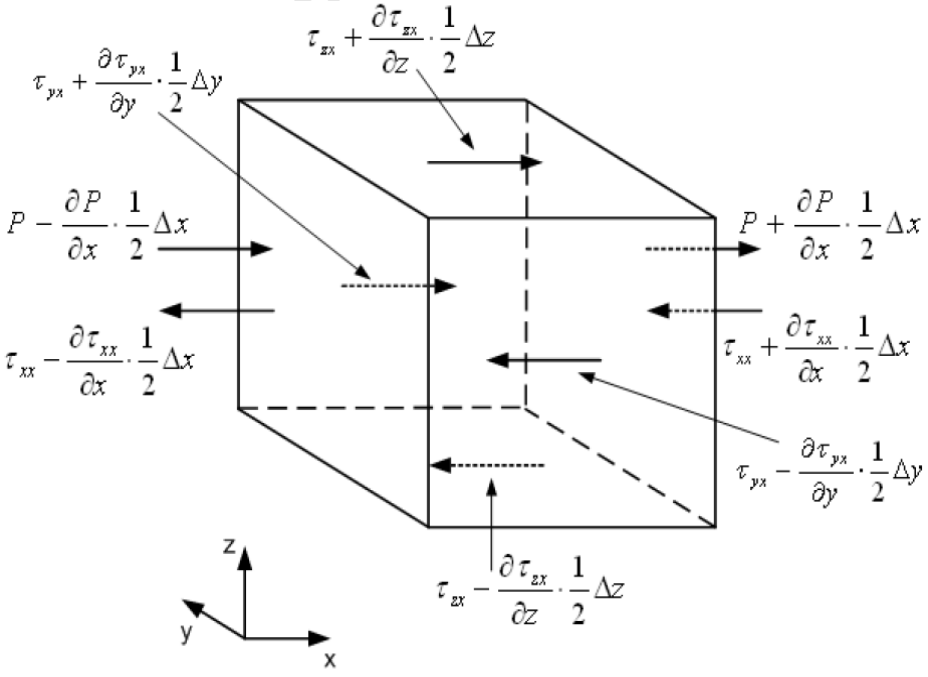

Figure A 3: Stress and pressure components on a standard cubic fluid element in the x-direction

Figure A 3 shows the stress and pressure terns for the x-direction on each of the faces at their centers. The figure can be used to find the net forces in the different directions of interest.

The net force for the faces with area $\Delta x\Delta z$ can be found using:

$$-\left(\tau_{yx}-\frac{\delta\tau_{yx}}{\delta y}\frac{1}{2}\Delta y\right)\Delta x\Delta z+\left(\tau_{yx}+\frac{\delta\tau_{yx}}{\delta y}\frac{1}{2}\Delta y\right)\Delta x\Delta z$$

The net force for the faces with area $\Delta y\Delta z$ can be found using:

$$\left[\left(P-\frac{\delta P}{\delta x}\frac{1}{2}\Delta x\right)-\left(\tau_{xx}-\frac{\delta\tau_{xx}}{\delta x}\frac{1}{2}\Delta x\right)\right]\Delta y\Delta z+\left[-\left(P+\frac{\delta P}{\delta x}\frac{1}{2}\Delta x\right)-\left(\tau_{xx}+\frac{\delta\tau_{xx}}{\delta x}\frac{1}{2}\Delta x\right)\right]\Delta y\Delta z$$

The net force for the faces with area $\Delta x\Delta y$ can be found using:

$$-\left(\tau_{zx}-\frac{\delta\tau_{zx}}{\delta z}\frac{1}{2}\Delta z\right)\Delta x\Delta y+\left(\tau_{zx}+\frac{\delta\tau_{zx}}{\delta z}\frac{1}{2}\Delta z\right)\Delta x\Delta y$$

The net force due to surface stress can be found by the summation of the three net force expressions shown above and dividing through by $\Delta x\Delta y\Delta z$.

$$\frac{\delta\left(-P+\tau_{xx}\right)}{\delta x}+\frac{\delta\tau_{yx}}{\delta y}+\frac{\delta\tau_{zx}}{\delta z} \qquad \text{(A.13)}$$

Equating (A.13) and a momentum source term in the x-direction with (A.10), the rate of change of momentum in the x-direction gives (A.14).

$$\rho\frac{Du_x}{Dt}=\frac{\delta\left(-P+\tau_{xx}\right)}{\delta x}+\frac{\delta\tau_{yx}}{\delta y}+\frac{\delta\tau_{zx}}{\delta z}+S_x \qquad \text{(A.14)}$$

In a similar fashion, the relationship derived in (A.14) for the x-direction maybe derived for the y- and z-directions as shown in (A.15) and (A.16) respectively.

$$\rho\frac{Du_y}{Dt}=\frac{\delta\tau_{xy}}{\delta x}+\frac{\delta\left(-P+\tau_{yy}\right)}{\delta y}+\frac{\delta\tau_{zy}}{\delta z}+S_y \qquad \text{(A.15)}$$

$$\rho\frac{Du_z}{Dt}=\frac{\delta\tau_{xz}}{\delta x}+\frac{\delta\tau_{yz}}{\delta y}+\frac{\delta\left(-P+\tau_{zz}\right)}{\delta z}+S_z \qquad \text{(A.16)}$$

Viscous stress

For Newtonian fluids, the viscous stress terms are proportional to the rates of deformation; such deformations are illustrated in Figure A 4. The viscous stress can be defined using (A.17) where μ is the dynamic viscosity.

$$\tau = \mu \frac{du_x}{dy} \tag{A.17}$$

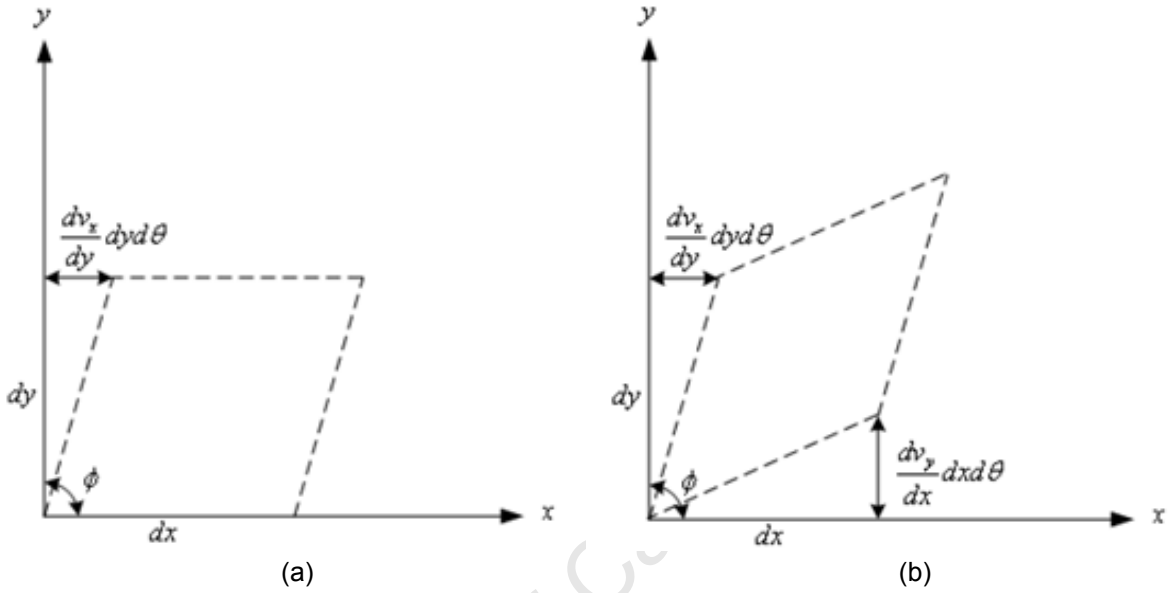

Figure A 4: Deformation of a 2-D square fluid element in (a) the x-direction and (b) x- and y-directions due to shear

Using Figure A 4(a) as a starting point, consider that the element deforms by an angle $d\phi$ over a set time $d\theta$ as shown in the figure which can be expressed as follows using (A.18).

$$d\phi = -\frac{\frac{du_x}{dy} dy d\theta}{dy} \tag{A.18}$$

Re-arranging (A.18) and substituting the result into(A.17) gives us alternative relationship for viscous stress in terms of the deformation angle and time.

$$\tau = -\mu \frac{d\phi}{d\theta} \tag{A.19}$$

Now consider that the element deformation in both the x- and y-directions as shown in Figure A 4(b), the deformation angle per time can be defined as shown in (A.20). Rearranging (A.20) and substituting the result into (A.19) gives us the viscous stress component in the x-y direction as shown in (A.21). The general form of (A.21) is defined by (A.22), if i=j, then (A.22) simplifies to (A.23).

$$d\phi = -\frac{\frac{du_x}{dy}dyd\theta}{dy} - \frac{\frac{du_y}{dx}dxd\theta}{dx} \tag{A.20}$$

$$\tau_{xy} = \tau_{yx} = \mu\left(\frac{\delta u_x}{\delta y} + \frac{\delta u_y}{\delta x}\right) \tag{A.21}$$

$$\tau_{ij} = \tau_{ji} = \mu\left(\frac{\delta u_i}{\delta j} + \frac{\delta u_j}{\delta i}\right) \tag{A.22}$$

$$\tau_{ii} = \mu\left(\frac{\delta u_i}{\delta i} + \frac{\delta u_i}{\delta i}\right) = 2\frac{\delta u_i}{\delta i} \tag{A.23}$$

Using (A.22) and (A.23), we can define the viscous stress components for a 3-D cubic fluid element are shown in (A.24) - (A.29). The two terms in (A.24) - (A.26) relate to the linear deformation and the volumetric deformation, however, for an incompressible fluid, the $\nabla \cdot \vec{u}$ = 0 (as shown in (A.4)) and therefore the volumetric deformation term can be neglected.

$$\tau_{xx} = 2\mu\rho\frac{\delta u_x}{\delta x} + \lambda\left(\nabla \cdot \vec{u}\right) \tag{A.24}$$

$$\tau_{yy} = 2\mu\rho\frac{\delta u_y}{\delta y} + \lambda\left(\nabla \cdot \vec{u}\right) \tag{A.25}$$

$$\tau_{zz} = 2\mu\rho\frac{\delta u_z}{\delta z} + \lambda\left(\nabla \cdot \vec{u}\right) \tag{A.26}$$

$$\tau_{xy} = \tau_{yx} = \mu\left(\frac{\delta u_x}{\delta y} + \frac{\delta u_y}{\delta x}\right) \tag{A.27}$$

$$\tau_{xz} = \tau_{zx} = \mu\left(\frac{\delta u_x}{\delta z} + \frac{\delta u_z}{\delta x}\right) \tag{A.28}$$

$$\tau_{yz} = \tau_{zy} = \mu\left(\frac{\delta u_y}{\delta z} + \frac{\delta u_z}{\delta y}\right) \tag{A.29}$$

Substituting (A.24),(A.27) and (A.28) into (A.14) and expanding the result gives (A.30) and realising that the continuity equation can be substituted into (A.30) yields (A.31) which is the conservation of momentum in the x-direction.

$$\rho\frac{Du_x}{Dt} = -\frac{\delta P}{\delta x} + \mu\frac{\delta^2 u_x}{\delta x^2} + \mu\frac{\delta^2 u_x}{\delta y^2} + \mu\frac{\delta^2 u_x}{\delta z^2} + \mu\frac{\delta}{\delta x}\left(\frac{\delta u_x}{\delta x} + \frac{\delta u_y}{\delta y} + \frac{\delta u_z}{\delta z}\right) + S_x \qquad \text{(A.30)}$$

$$\rho\frac{Du_x}{Dt} = -\frac{\delta P}{\delta x} + \nabla\cdot\left(\mu\nabla u_x\right) + S_x \qquad \text{(A.31)}$$

If we apply the same formulation for the y- and z-directions using (A.15) and (A.16) respectively, (A.32) and (A.33) can be obtained.

$$\rho\frac{Du_y}{Dt} = -\frac{\delta P}{\delta y} + \nabla\cdot\left(\mu\nabla u_y\right) + S_y \qquad \text{(A.32)}$$

$$\rho\frac{Du_z}{Dt} = -\frac{\delta P}{\delta z} + \nabla\cdot\left(\mu\nabla u_z\right) + S_z \qquad \text{(A.33)}$$

The general conservation of momentum equation can be representing as follows using (A.34) where S_{mom} defines the momentum source term in all 3 directions.

$$\rho\frac{D\vec{u}}{Dt} = -\frac{\delta P}{\delta y} + \nabla\cdot\left(\mu\nabla\vec{u}\right) + S_{mom} \qquad \text{(A.34)}$$

Applying (A.34) to the PEMFC model, gives the equation outlined in the model development section (4.23). Expanding the total derivative provides the outcome shown in (A.35), realising that the system is at steady state, (A.35) simplifies to (A.36).

$$\rho\frac{\delta\vec{u}}{\delta t} + \rho\vec{u}\cdot\nabla\vec{u} = -\frac{\delta P}{\delta y} + \nabla\cdot\left(\mu\nabla\vec{u}\right) + S_{mom} \qquad \text{(A.35)}$$

$$\rho\vec{u}\cdot\nabla\vec{u} = -\frac{\delta P}{\delta y} + \nabla\cdot\left(\mu\nabla\vec{u}\right) + S_{mom} \qquad \text{(A.36)}$$

A.2. Fuel Cell Equations

3-D Model Boundary Conditions

The derivations of the boundary conditions shown in section 4.2.5 are provided in this appendix. For either the anode or cathode the total mass flow in can be defined by (A.37) where ρ_{in} is the density

of the feed mixture, u_{in} is the inlet velocity and $A_{channel}$ is the channel cross-sectional area. Considering first the anode side, the moles of hydrogen fed in at the anode can be defined by (A.38) where ζ_a is the stoichiometric flow ratio for the anode feed, *i* is the average current density, A_{MEA} is the MEA and F is Faraday's constant.

$$\dot{m}_{in} = \rho_{in} u_{in} A_{channel} \tag{A.37}$$

$$\dot{n}_{H_2,in} = \zeta_a \frac{iA_{MEA}}{2F} \tag{A.38}$$

The anode hydrogen is normally fed with some water vapour which is expressed as a relative humidity (RH) value, therefore the total number of moles fed in at the anode can be expressed using (A.39). To calculate the mole fraction of water in the anode feed based on the RH value, Dalton's law can be applied as shown in (A.40) where $P_{sat}(T)$ is the saturation pressure which can be found using Antoine's equation with the relevant coefficients being applied for a given temperature and P_{in} is the total inlet pressure.

$$\dot{n}_{Total,in} = \dot{n}_{H_2,in} + \dot{n}_{H_2O,in} \tag{A.39}$$

$$y_{H_2O,a,in} = \frac{\dot{n}_{H_2O,in}}{\dot{n}_{H_2,in} + \dot{n}_{H_2O,in}} = \frac{P_{H_2O,in}}{P_{in}} = RH_a \frac{P_{sat}(T)}{P_{in}} \tag{A.40}$$

The inlet density for both anode and cathode can be determined using the ideal gas assumption stated in section 4.2.2 as shown in (A.41) where R is the universal gas constant, T is the temperature and M_{in} is the molar mass of the feed mixture.

$$\rho_{in} = \frac{P_{in}}{RT} M_{in} \tag{A.41}$$

Rearranging (A.37) to make the inlet velocity the subject of the equation as shown in (A.42) and substituting (A.41) into (A.42) gives (A.43) which is applicable to both anode and cathode.

$$u_{in} = \frac{\dot{m}_{in}}{\rho_{in} A_{channel}} = \frac{\dot{n}_{in} M_{in}}{\rho_{in} A_{channel}} \tag{A.42}$$

$$u_{in} = \frac{\dot{n}_{in} RT}{P_{in} A_{channel}} \tag{A.43}$$

For the anode, realising that $\dot{n}_{in}$ can be expressed in terms of $\dot{n}_{H_2,in}$ and substituting (A.38) into the result yields (A.44).

$$\dot{n}_{in} = \frac{\zeta_a \frac{iA_{MEA}}{2F}}{1 - y_{H_2O,a,in}} = \frac{\zeta_a \frac{iA_{MEA}}{2F}}{y_{H_2,in}} \tag{A.44}$$

Substituting (A.44) into (A.43) and rearranging the result yields the final equation used for the anode fuel cell boundary condition as shown in (A.45).

$$u_{in,a} = \zeta_a \frac{i}{2F} A_{MEA} \frac{1}{y_{H_2,in}} \frac{RT_{in,a}}{P_{a,in}} \frac{1}{A_{Channel}} \tag{A.45}$$

A similar process is used to obtain the inlet velocity for the cathode side, the moles of oxygen fed into the cathode is defined by (A.46) while the total moles fed at the cathode and the mole fraction of water fed in at the cathode are defined by (A.47) and (A.48).

$$\dot{n}_{O_2,in} = \zeta_c \frac{iA_{MEA}}{4F} \tag{A.46}$$

$$\dot{n}_{Total,in} = \dot{n}_{O_2,in} + \dot{n}_{N_2,in} + \dot{n}_{H_2O,in} \tag{A.47}$$

$$y_{H_2O,c,in} = \frac{\dot{n}_{H_2O,in}}{\dot{n}_{O_2,in} + \dot{n}_{N_2,in} + \dot{n}_{H_2O,in}} = \frac{P_{H_2O,in}}{P_{in}} = RH_c \frac{P_{sat}(T)}{P_{in}} \tag{A.48}$$

For the cathode, realising that $\dot{n}_{in}$ can be expressed in terms of $\dot{n}_{O_2,in}$ and substituting (A.46) into the result yields (A.49).

$$\dot{n}_{in} = \frac{\zeta_c \frac{iA_{MEA}}{4F}}{1 - y_{H_2O,c,in} - y_{N_2,in}} = \frac{\zeta_c \frac{iA_{MEA}}{4F}}{y_{O_2,in}} \tag{A.49}$$

Substituting (A.49) into (A.43) and rearranging the result yields the final equation used for the cathode fuel cell boundary condition as shown in (A.50).

$$u_{in,c} = \zeta_c \frac{i}{4F} A_{MEA} \frac{1}{y_{O_2,in}} \frac{RT_{in,c}}{P_{c,in}} \frac{1}{A_{Channel}} \tag{A.50}$$

Derivation of Fuel Cell Key Equations

The derivations of the Nernst-Planck equation as well as the Butler-Volmer equation are presented in this appendix along with the limiting cases of the Butler-Volmer equation.

Nernst-Planck Equation

The Nernst-Planck equation builds on the equations derived in section 4.1 by considering the migration of ions as well as convection and diffusion and convection of species.

The Nernst-Planck equation can be broken down into three individual molar fluxes, namely these are the flux due to diffusion, convection and electrophoretic effects. The equation for each of the fluxes is shown below.

Diffusion – The molar diffusive flux is illustrated by Fick's law as shown in (2.1) in section 2.3.3.

Convection – (A.51) describes the general convection equation which accounts for the convective flux where u_j defines the velocity of species *j*.

$$N_j = \frac{QC_j}{A} = u_j C_j \tag{A.51}$$

Flux due to electrophoretic effects – the flux due to electrophoretic effects describes the relationship between the ionic mobility (u) and the electric potential (ϕ) as shown in (A.52).

$$N_j = -uC_j\left(\frac{\delta\phi}{\delta z}\right) \tag{A.52}$$

The ionic mobility (u) can be further defined as a function of the Diffusivity (D_j) and can be written as shown in (A.53). This relation is called the Nernst-Einstein relationship where F is Faraday's constant, n_i is the number of electrons involved in the reaction in region *i* (either the anode or cathode reaction), R is the universal gas constant and T is the temperature of the cell.

$$u = \frac{D_j n_i F}{RT} \tag{A.53}$$

Replacing (A.53) in (A.52) and realising fluxes are additive (summing (2.1),(A.51) and (A.52)), the Nernst-Planck equation is obtained as shown in (A.54).

$$N_j = -D_j\left(\frac{\delta C_j}{\delta z}\right) + u_j C_j - \frac{D_j n_i F}{RT} C_j\left(\frac{\delta\phi}{\delta z}\right) \tag{A.54}$$

Butler-Volmer Equation

The Butler-Volmer equation is derived from first principles in this section. The following derivation has been interpreted from the book by Schmickler (1996).

First, an understanding of the relationship between current and electrode potential must be gained, in electrochemical reactions, the rate of reaction is a function of the electrode potential (ϕ), the Butler-Volmer equation is a model that relates the current density of a system as a function of potential and concentration.

A typical electron-transfer reaction can be quite a complicated process with processes such as bond breakage or formation occurring as well as absorbance on specific catalysts (Schmickler, 1996). However, if we consider a simple transfer reaction called the outer sphere electron-transfer reaction, in which nothing happens but the exchange of one electron, no bonds are broken or formed, the reactants are not specifically adsorbed, and catalysts play no role (Schmickler, 1996). It must be noted that if one of the above conditions is not met, the pathway is known as an inner-sphere pathway.

For this derivation, let us consider a simple one electron reaction system as shown in (A.55) where O is the oxidated species, R is the reduced species and n is the number of electrons taking part in the reaction. The rates of forward and reverse (backward) reaction as well as the net rate of reaction are shown in (A.56).

$$R \rightleftarrows O + ne^{-} \tag{A.55}$$

$$r_f = k_{ox} C_{red}$$

$$r_b = k_{red} C_{ox} \tag{A.56}$$

$$r_{net} = k_{ox} C_{red} - k_{red} C_{ox}$$

Considering a system in equilibrium as shown in (A.55), the net rate of reaction is zero and the equilibrium rate of reaction r_{eq} can be defined as shown in (A.57). The units of the rate of reaction are $\frac{mols}{Area \cdot Time}$.

$$r_{eq} = k_{red} C_{ox}^{eq} = k_{ox} C_{red}^{eq} \tag{A.57}$$

Now, an understanding of Faraday's law must be gained to understand the relationship between charge and moles. Faraday's law describes cell "work" as the rate at which charge passes through an external circuit, knowing this, the number of moles reacted can be expressed in terms of charge (

Q) as shown in (A.58). Considering a differential form of the rate as shown in (A.59), an equation for the rate as a function of current density is obtained.

$$N = \frac{Q}{nF} \tag{A.58}$$

$$r = \frac{1}{A}\frac{dN}{dt} = \frac{1}{A}\frac{d}{dt}\left(\frac{Q}{nF}\right) = \frac{1}{nAF}\frac{dQ}{dt} = \frac{I}{nAF} = \frac{i}{nF} \tag{A.59}$$

Applying absolute rate theory, the rate constants can be return in the form shown in (A.60) and (A.61) where $\Delta G_{oxidation}(\phi)$ and $\Delta G_{reduction}(\phi)$ are the activation energies of the oxidation and reduction reactions respectively and are functions of the electrode potential.

$$k_{ox} = A\exp\left(-\frac{\Delta G_{oxidation}(\phi)}{RT}\right) \tag{A.60}$$

$$k_{red} = A\exp\left(-\frac{\Delta G_{reduction}(\phi)}{RT}\right) \tag{A.61}$$

Expanding $\Delta G_{oxidation}(\phi)$ and $\Delta G_{reduction}(\phi)$ till the first order term about the standard equilibrium potential ($\phi_{eq,std}$), the following relationships are obtained as shown in (A.62) and (A.63) where the terms α and β are the anodic and cathodic charge transfer coefficients (explained further on in the derivation) and A is the pre-exponential factor. The relationships used to define the transfer coefficients are shown in (A.64) and (A.65).

$$\Delta G_{oxidation}(\phi) = \Delta G_{oxidation}(\phi_{eq,std}) - \alpha nF(\phi - \phi_{eq,std}) \tag{A.62}$$

$$\Delta G_{reduction}(\phi) = \Delta G_{reduction}(\phi_{eq,std}) + \beta nF(\phi - \phi_{eq,std}) \tag{A.63}$$

$$\alpha = -\frac{1}{nF}\frac{\delta\left(\Delta G_{oxidation}(\phi)\right)}{\delta\phi}\bigg|_{\phi_{eq,std}} \tag{A.64}$$

$$\beta = \frac{1}{nF}\frac{\delta\left(\Delta G_{reduction}(\phi)\right)}{\delta\phi}\bigg|_{\phi_{eq,std}} \tag{A.65}$$

The Gibbs energies of activation are correlated to the molar Gibbs energies of the oxidised and reduced states using (A.66).

$$\Delta G_{oxidation}(\phi) - \Delta G_{reduction}(\phi) = G_{oxidation} - G_{reduction} \tag{A.66}$$

Consider that when the electrode potential is changed from the standard equilibrium state ($\phi_{eq,std}$) to another value (ϕ), the Gibbs energy of the electrons on the electrode is lowered by an amount defined by the expression shown in (A.67) and so is the energy of the oxidized state. Assuming an outer sphere electron transfer reaction as stated in (A.55) in which the electrostatic energy of the reactants is not significantly affected by a change in the electrode potential (due to the reactants are far from the metal surface) then the change in the Gibbs energy of reaction is defined by (A.68).

$$-nF\left(\phi - \phi_{eq,std}\right) \tag{A.67}$$

$$\Delta G_{oxidation}(\phi) - \Delta G_{reduction}(\phi) = -nF\left(\phi - \phi_{eq,std}\right) \tag{A.68}$$

Summing the relationships for the anode and cathode transfer coefficients ((A.64) and (A.65))), replacing (A.68) in the sum, we obtain the following relationship shown in (A.69). Rearranging (A.69) and differentiating the result, we obtain a relationship for the cathode transfer coefficient in terms of the anode transfer coefficient as shown in (A.70).

$$\alpha + \beta = \frac{1}{F}\left(-\frac{\delta\left(\Delta G_{oxidation}(\phi)\right)}{\delta\phi}\bigg|_{\phi_{eq,std}} + \frac{\delta\left(\Delta G_{oxidation}(\phi) + nF\left(\phi - \phi_{eq,std}\right)\right)}{\delta\phi}\bigg|_{\phi_{eq,std}} \right) \tag{A.69}$$

$$\beta = 1 - \alpha \tag{A.70}$$

Returning now to the equations outlined in (A.56) and remembering that the current is related to the rate of reaction as shown in (A.59) and replacing the values for the rate constants with the expressions above yields the following equation as shown in (A.71) where the term k_0 is defined as the value of the reaction rate constant at the standard equilibrium potential and is shown in (A.72).

$$i_{net} = nFk_0\left[C_{red}\exp\left(\frac{\alpha nF}{RT}\left(\phi - \phi_{eq,std}\right)\right) - C_{ox}\exp\left(-\frac{(1-\alpha)nF}{RT}\left(\phi - \phi_{eq,std}\right)\right)\right] \tag{A.71}$$

$$k_0 = A\exp\left(-\frac{\Delta G\left(\phi_{eq,std}\right)}{RT}\right) \tag{A.72}$$

In a system going to equilibrium, the equilibrium potential (ϕ_{eq}) is defined in terms of the standarad equilibrium potential ($\phi_{eq,std}$) by the Nernst equation shown in (A.73) where a_{ox} and a_{red} are the activities of the oxidised and reduced species.

$$\phi_{eq} = \phi_{eq,std} + \frac{RT}{nF}\ln\frac{a_{ox}}{a_{red}} = \phi_{eq,std} + \frac{RT}{nF}\ln\frac{\gamma_{ox}C_{ox}}{\gamma_{red}C_{red}} = \phi_{eq,std} + \frac{RT}{nF}\ln\frac{\gamma_{ox}}{\gamma_{red}} + \frac{RT}{nF}\ln\frac{C_{ox}}{C_{red}} \qquad \text{(A.73)}$$

Now considering equilibrium, the following applies where $\phi_{eq,\,formal}$ is defined as the formal potential.

$$C_{ox} = C_{red} \rightarrow \phi_{eq} = \phi_{eq,std} + \frac{RT}{nF}\ln\frac{\gamma_{red}}{\gamma_{ox}} = \phi_{eq,\,formal} \qquad \text{(A.74)}$$

Introducing a term called the overpotential (η) which defines the deviation from the equilibrium potential ($\phi_{eq,\,formal}$) shown in (A.75).

$$\eta = \phi - \phi_{eq,\,formal} \qquad \text{(A.75)}$$

To simplify (A.71) further, a term called the exchange current density i_0 can be defined as follows using (A.76).

$$i_0 = nFk_0C_{red}^{(1-\alpha)}C_{ox}^{\alpha} \qquad \text{(A.76)}$$

Replacing (A.75) and (A.76) in (A.71) we obtain the general form of the Butler-Volmer equation as shown in (A.77).

$$i_{net} = i_0\left[\frac{C_{red}}{C_{red}^{bulk}}\exp\left(\frac{\alpha nF\eta}{RT}\right) - \frac{C_{ox}}{C_{ox}^{bulk}}\exp\left(-\frac{(1-\alpha)nF\eta}{RT}\right)\right] \qquad \text{(A.77)}$$

The transfer coefficient describes the change in the energy of activation with the Gibbs energy of reaction and is equivalent to the Broenstedt coefficient well known from ordinary chemical kinetics (Schmickler, 1996). The transfer coefficient has two purposes; the first is to determine the dependence of the current on the electrode potential. The second is to provide the variation of the Gibbs energy of activation with potential. The transfer coefficient determines the symmetry of the current-potential curves as shown in Figure A 5.

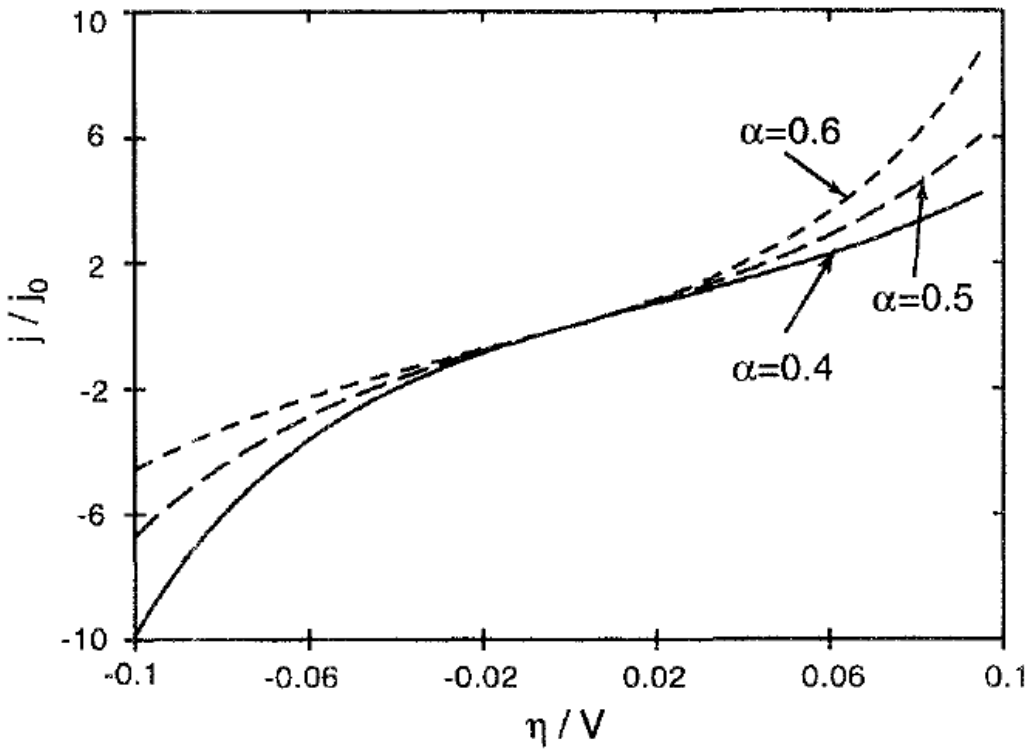

Figure A 5: Current-potential curves according to the Butler-Volmer equation with different values of α (Schmickler, 1996)

Limiting Cases of the Butler-Volmer Equation

A) Low overpotentials - Linear response (Zhang, 2008)

Assuming dilute solutions and for low overpotentials as shown in (A.78), the Butler-Volmer equation can be linearised leading to a linear approximation between current and overpotential as shown in (A.79).

$$|\eta| \ll \frac{RT}{nF} \tag{A.78}$$

$$i_{net} = i_0 \frac{nF\eta}{RT} \tag{A.79}$$

B) High overpotentials – Tafel response (Zhang, 2008)

Assuming dilute solutions and for high overpotentials as shown in (A.80), the Butler-Volmer equation reduces to a tafel type relationship as shown in (A.81). As the overpotential increases,

the Butler-Volmer predicts a linear response. The Tafel plot of $\ln|i_{net}|$ vs. η yields the a slope of $\frac{\alpha nF}{RT}$ for the anodic current and $\frac{(1-\alpha)nF}{RT}$ for the cathodic current and a *y*-intercept of $\ln|i_{net}|$.

$$|\eta| \gg \frac{RT}{nF} \tag{A.80}$$

$$i_{net} = \begin{cases} i_0 \exp\left(\frac{\alpha nF\eta}{RT}\right); & \eta \gg \frac{RT}{nF} \\ i_0 \exp\left(-\frac{(1-\alpha)nF\eta}{RT}\right); & \eta \ll -\frac{RT}{nF} \end{cases} \tag{A.81}$$

C) Symmetric electron transfer (Moudgil, 2010)

It is common to assume symmetric electron transfer in the Butler-Volmer equation where the charge transfer coefficient (α) is set as 0.5. This assumption adapts the general Butler-Volmer equation shown in (A.77) as shown in (A.82).

$$i_{net} = i_0 \left[\frac{C_{red}}{C_{red}^{bulk}} \exp\left(\frac{nF\eta}{2RT}\right) - \frac{C_{ox}}{C_{ox}^{bulk}} \exp\left(-\frac{nF\eta}{2RT}\right) \right] \tag{A.82}$$

Simplifying (A.82) by assuming a dilute solution and using (A.83) where x defines a lumped parameter and multiplying and dividing the result by 2, (A.84) is obtained.

$$x = \frac{nF\eta}{2RT} \tag{A.83}$$

$$i_{net} = 2i_0 \frac{\left[\exp(x) - \exp(-x)\right]}{2} \tag{A.84}$$

Remembering the definition of the hyperbolic sine function using (A.85), therefore the Butler-Volmer equation for dilute solutions can be expressed using the hyperbolic sine function as shown in (A.86).

$$\sinh x = \frac{\left[\exp(x) - \exp(-x)\right]}{2} \tag{A.85}$$

$$i_{net} = 2i_0 \sinh\left(\frac{\eta Fn}{2RT}\right) \tag{A.86}$$

When the solution is not dilute, (A.86) is modified for the anode and cathode as shown in (A.87) and (A.88) respectively. These are the equations shown in section 4.2.5.

$$i_a = 2i_{a,0}\left(\frac{C_{H_2}}{C_{H_2,ref}}\right)^{0.5}\sinh\left(\frac{\eta_a F n_a}{2RT}\right) \tag{A.87}$$

$$i_c = 2i_{c,0}\left(\frac{C_{O_2}}{C_{O_2,ref}}\right)\sinh\left(\frac{\eta_c F n_c}{2RT}\right) \tag{A.88}$$

APPENDIX B – UDF CODE

```
#include "udf.h"

/*****************************************************************************************************************/

/* ANODE SIDE */

/*****************************************************************************************************************/


/*****************************************************************************************************************/

/* ANODE VELCOITY PROFILE */

/*****************************************************************************************************************/

DEFINE_PROFILE(VelocityAnode_Profile, thread, position)

{

Thread *t;

cell_t c;

/* This UDF applies a parabolic velocity profile to the boundary surface hooked in Fluent */

/* This operates for 3D models in any orientation */

/*****************************/

/* The user inputs */

/*****************************/

/* the centroid of the boundary face (x0,y0,z0) */

real x0 = 0.0;

real y0 = 0.0;

real z0 = 0.0;

//Stochiometric factor

real Anode = 1.5;

real Cathode = 2;
```

```
real F = 96485.4; /* Faradays constant (C/mol) */

real R = 8.314; /* Universal gas constant (J/mol)*/

real T = 353; /* Temperature (K) */

real P_anode = 100000*2; /* Anode pressure (Pa) */

real x_H2O = 0.1897; /* water vapour mol fraction at 50% RH */

real i = 5000; /*current density (A/m2)  */

real width_channel = 0.8; /* mm */

real width_land = 0.8; /*mm*/

real length_channel = 3.4; /* mm */

real length_MEA = 3.4; /* mm */

real height_channel = 1; /*mm*/

real height_GDL = 0.4375; /*mm*/

real Achannel = height_channel*width_channel; /* Crossectional Area of channel (m2) */

real Acell = length_MEA*(width_channel+width_land); /* MEA area (m2) */


real x[ND_ND]; /* this will hold the position vector of the face/element centroid */


real VelocityAnode_Profile; /* Velocity to be written to boundary */

//face_t f; /* f the hooked boundary face in fluent */

/* This starts the main loop. As each element on the face is looped over its centroid is determined and the distance from this to the centre of the parabola. The velocity required is calculated based on this distance and applied. */

begin_c_loop(c,thread);

{

C_CENTROID(x, c, thread); /* the coordinates of the current face/element centroid accessed by F_CENTROID */

/* Write Profile in x */
```

```
VelocityAnode_Profile = (((Anode*i/(2*F))*Acell)/(1-x_H2O)/(P_anode*Achannel/(R*T)));

/* Write velocity boundary condition */

F_PROFILE(c, thread, position) = VelocityAnode_Profile; /* Apply velocity profile to selected boundary
*/

}

end_c_loop(c, thread);

}


/*****************************************************************************************************************/

/* H2 SOURCE TERM AT ANODE */

/*****************************************************************************************************************/

DEFINE_SOURCE(H2_sink,c,t,dS,eqn)

{

real x[ND_ND];


real i = 5000; /* A/m2 */

real F = 96485.4; /*Faradays constant (C/mol) */

real M_H2 = 2e-3; /* Molecular weight of Hydrogen kg/mol */

real H2_sink;

real A = 0.0625/1000; /* specific area of anode catalyst area 1/m */

if (THREAD_ID(t)== 2)

{

   H2_sink = -((i*M_H2)/(2*F*A));

   dS[eqn] = 0;

}

else
```

```
{
    H2_sink = dS[eqn] = 0;
}
return H2_sink;
}

/*****************************************************************************************************************/
/* ANODE FEED DENSITY */
/*****************************************************************************************************************/
DEFINE_PROPERTY(anodef_density, cell, thread)
{
Thread *t;
cell_t c;
real T=353;
real P0;
real anodef_density;
real M_H2;
real M_H2O;
real R;
real RH;
real A, B, C;
real P_sat, P_H2O;
real x_H2O;
real exp1;
real base1;
real n_basis;
```

```
real m_basis;

real y_H2O;

real y_H2;

real M_mix;


P0 =100000*2; /* Pa */


/* mole fraction calculation */


RH = 0.8; /* relative humidity at the anode (fraction) */

R = 8.314; /* Universal Gas constant (J/mol.K) */

/* Antoine coefficients (T in celcius) */

A = 8.10765;

B = 1750.286;

C = 235;

exp1 = (A - B/((T-273)+C));

base1= 10;

P_sat = pow(base1,exp1);

/* Saturation Pressure (mm Hg) */

P_H2O = RH*(P_sat*(101.325/760)); /* Water vapour pressure (kPa) */

x_H2O = P_H2O*1000/P0; /* x_H2O is mole fraction/y_H2O is mass fraction */


/* Density Calculation */

M_H2 = 0.002; /* kg/mol */

M_H2O = 0.018; /* kg/mol */

n_basis = 100; // moles of feed (basis)
```

```
m_basis = (x_H2O*n_basis)*18 + ((1-x_H2O)*n_basis)*2;


y_H2O = ((x_H2O*n_basis)*18)/m_basis;

y_H2 = 1-y_H2O;


M_mix  = x_H2O*M_H2O + (1-x_H2O)*M_H2;

anodef_density = ((P0/(R*T))*(1/((y_H2O/M_H2O) + ((1-y_H2O)/M_H2))));


return anodef_density;

}


/*****************************************************************************************************************/

/* ANODE MOMENTUM SOURCE TERM - X DIRECTION */

/*****************************************************************************************************************/

DEFINE_SOURCE(x_mom_anode,c,t,dS,eqn) /* anode x momentum source */

{

real x[ND_ND];

real x_mom_anode;

real mu = C_MU_L(c,t); /* viscosity (kg/m.s) */

real K; /* Porous media permeability (m2) */

K = 5e-11;

C_CENTROID(x,c,t);

x_mom_anode = -mu*C_U(c,t)/K;

dS[eqn] = -mu/K;

return x_mom_anode;

}
```

```
/*****************************************************************************************************************/
/* ANODE MOMENTUM SOURCE TERM - Y DIRECTION */
/*****************************************************************************************************************/
DEFINE_SOURCE(y_mom_anode,c,t,dS,eqn) /* anode y momentum source */
{
real x[ND_ND];
real y_mom_anode;
real mu = C_MU_L(c,t); /* viscosity (kg/m.s) */
real K; /* Porous media permeability (m2) */
K = 5e-11;
C_CENTROID(x,c,t);
y_mom_anode = -mu*C_V(c,t)/K;
dS[eqn] = -mu/K;
return y_mom_anode;
}

/*****************************************************************************************************************/
/* ANODE MOMENTUM SOURCE TERM - Z DIRECTION */
/*****************************************************************************************************************/
DEFINE_SOURCE(z_mom_anode,c,t,dS,eqn) /* anode z momentum source */
{
real x[ND_ND];
real z_mom_anode;
real mu = C_MU_L(c,t); /* viscosity (kg/m.s) */
real K; /* Porous media permeability (m2) */
```

```
K = 5e-11;

C_CENTROID(x,c,t);

z_mom_anode = -mu*C_W(c,t)/K;

dS[eqn] = -mu/K;

return z_mom_anode;

}


/************************************************************************************************************************/

/* CATHODE SIDE */

/************************************************************************************************************************/

/************************************************************************************************************************/

/* CATHODE VELCOITY PROFILE */

/************************************************************************************************************************/

DEFINE_PROFILE(VelocityCathode_Profile2, thread, position)

{

Thread *t;

cell_t c;

/* This UDF applies a parabolic velocity profile to the boundary surface hooked in Fluent */

/* This operates for 3D models in any orientation */

/*****************************/

/* The user inputs */

/*****************************/

/* the centroid of the boundary face (x0,y0,z0) */

//real x0 = 0.0;

//real y0 = 0.0;

//real z0 = 0.0;
```

```
//Stochiometric factor

real Anode = 1.5;

real Cathode = 2;

real F = 96485.4; /* Faradays constant (C/mol) */

real R = 8.314; /* Universal gas constant (J/mol)*/

real T = 353; /* Temperature (K) */

real P_cathode = 100000*2; /* Anode pressure (Pa) */

real x_O2 = 0.1851;

real x_H2O = 0.1186;/* water vapour mol fraction at 25% RH */

real i = 10000; /*(A/m2) current density */

real width_channel = 0.8; /* mm */

real width_land = 0.8; /*mm*/

real length_channel = 5.4; /* mm */

real length_MEA = 3.4; /* mm */

real height_channel = 1; /*mm*/

real height_GDL = 0.4375; /*mm*/

real Achannel = height_channel*width_channel; /* Crossectional Area of channel (m2) */

real Acell = length_MEA*(width_channel+width_land); /* MEA area (m2) */


real x[ND_ND]; /* this will hold the position vector of the face/element centroid */


real VelocityCathode_Profile2; /* Velocity to be written to boundary */

face_t f; /* f the hooked boundary face in fluent */
```

```
/* This starts the main loop. As each element on the face is looped over its centroid is determined and the distance from this to the centre of the parabola. The velocity required is calculated based on this distance and applied. */

begin_f_loop(f,thread);

{

F_CENTROID(x, f, thread); /* the coordinates of the current face/element centroid accessed by F_CENTROID */

/* Write Profile in x */

VelocityCathode_Profile2 = (((Cathode*i/(4*F))*Acell)/(x_O2)/(P_cathode*Achannel/(R*T)));


/* Write velocity boundary condition */

F_PROFILE(f, thread, position) = VelocityCathode_Profile2; /* Apply velocity profile to selected boundary */

}

end_f_loop(f, thread);

}


/*****************************************************************************************************************/

/* O2 SOURCE TERM AT CATHODE */

/*****************************************************************************************************************/

DEFINE_SOURCE(O2_sink,c,t,dS,eqn)

{

real x[ND_ND];

real volume;

real cl_volume;

real area;

real i = 10000; /* A/m2 */
```

```
real F = 96485.4; /*Faradays constant (C/mol) */

real M_O2 = 32e-3; /* Molecular weight of oxygen kg/mol */

real O2_sink;

real A = (0.0625/1000); /* specific area of anode catalyst area 1/m */


if (THREAD_ID(t)== 2)

{

   O2_sink = -((i*M_O2)/(4*F*A));

   dS[eqn] = 0;

}

else

{

   O2_sink = dS[eqn] = 0;

}

return O2_sink;

}


/*****************************************************************************************************************/

/* CATHODE FEED DENSITY */

/*****************************************************************************************************************/

DEFINE_PROPERTY(cathodef_density, cell, thread)

{

Thread *t;

cell_t c;

real P0;

real cathodef_density;
```

```
real M_N2;

real M_O2;

real R;

real RH;

real A, B, C;

real P_sat, P_H2O, x_H2O;

real M_H2O;

real x_O2 = 0.1851;

real exp1;

real base1;


P0 =100000*2; /* Pa */


/* mole fraction calculation */

RH = 0.5; /* relative humidity at the cathode (fraction) */

R = 8.314; /* Universal Gas constant (J/mol.K) */

/* Antoine coefficients (T in celcius) */

A = 8.10765;

B = 1750.286;

C = 235;

exp1 = (A - B/((C_T(c,t)-273)+C));

base1= 10;

P_sat = pow(base1,exp1);

/* Saturation Pressure (mm Hg) */

P_H2O = RH*(P_sat*(101.325/760)); /* Water vapour pressure (kPa) */

x_H2O = P_H2O*1000/P0; /* x_H2O is mole fraction/y_H2O is mass fraction */
```

```
/* Density Calculation */

M_N2 = 28e-3; /* kg/mol */

M_O2 = 32e-3; /* kg/mol */

M_H2O = 18e-3; /* kg/mol */


cathodef_density = (P0/(R*C_T(c,t)))*(1/((x_O2/M_O2) + (x_H2O/M_N2) + ((1-x_O2-
x_H2O)/M_N2)));


return cathodef_density;

}


/*****************************************************************************************************************/

/* CATHODE MOMENTUM SOURCE TERM - X DIRECTION */

/*****************************************************************************************************************/

DEFINE_SOURCE(x_mom_cathode,c,t,dS,eqn) /* cathode x momentum source */

{

real x[ND_ND];

real x_mom_cathode;

real mu = C_MU_L(c,t); /* viscosity (kg/m.s) */

real K; /* Porous media permeability (m2) */

K = 5e-11;

C_CENTROID(x,c,t);

x_mom_cathode = -mu*C_U(c,t)/K;

dS[eqn] = -mu/K;

return x_mom_cathode;
```

```
}

/*****************************************************************************************************************/

/* CATHODE MOMENTUM SOURCE TERM - Y DIRECTION */

/*****************************************************************************************************************/

DEFINE_SOURCE(y_mom_cathode,c,t,dS,eqn) /* cathode y momentum source */

{

real x[ND_ND];

real y_mom_cathode;

real mu = C_MU_L(c,t); /* viscosity (kg/m.s) */

real K; /* Porous media permeability (m2) */

K = 5e-11;

C_CENTROID(x,c,t);

y_mom_cathode = -mu*C_V(c,t)/K;

dS[eqn] = -mu/K;

return y_mom_cathode;

}


/*****************************************************************************************************************/

/* ANODE MOMENTUM SOURCE TERM - Z DIRECTION */

/*****************************************************************************************************************/

DEFINE_SOURCE(z_mom_cathode,c,t,dS,eqn) /* cathode z momentum source */

{

real x[ND_ND];

real z_mom_cathode;

real mu = C_MU_L(c,t); /* viscosity (kg/m.s) */

real K; /* Porous media permeability (m2) */
```

```
K = 5e-11;

C_CENTROID(x,c,t);

z_mom_cathode = -mu*C_W(c,t)/K;

dS[eqn] = -mu/K;

return z_mom_cathode;

}


/*****************************************************************************************************************/

/*WATER VAPOUR SOURCES TERMS*/

/*****************************************************************************************************************/


/*****************************************************************************************************************/

/* WATER VAPOUR CATHODE SOURCES TERMS */

/*****************************************************************************************************************/

DEFINE_SOURCE(cathode_H2O_source,c,t,dS,eqn)

{

/* constants for saturation pressure and water activity*/

real x[ND_ND];

real cathode_H2O_source;

real M_H2O = 0.018;

real A_int = 0.0625/1000;

real T = 353;

real R = 8.314; /* Universal Gas constant (J/mol.K) */

real F = 96485.4; /*Faradays constant (C/mol) */

real A;

real B;
```

```
real C;

real RH;


real exp1;

real base1;

real P_sat; /* Saturation pressure (Pa) */

real P0 = 100000*2; /* atmosphereic pressure (Pa) */

real P_H2;

real x_H2O;

real P_H2O;

real n_basis;

real m_basis;

real y_H2O;

real y_H2;

real H2O_act_anode;

real i = 10000;

real alpha;

/* constants for electro-osmotic drag and water concentration */

real n_d; /*electro-osmotic drag coefficient */

real H2O_conc_anode;


real mem_density; /* membrane dry desnity (kg/m3) */

real mem_mass; /* membrane dry mass (kg/mol) */

real mem_thick; /* membrane thickness (m) */

real tot_volume;

real H2O_conc_anode_avg;
```

```
real n_d_avg;

/* water diffusivity */

real D_H2O;

real D_H2O_avg;

real M_H2 = 2e-3; /* Molecular weight of Hydrogen kg/mol */

real M_O2 = 32e-3; /* Molecular weight of Oxygen kg/mol */

real conc_anode;


/* cathode side terms */

real RH_cathode = 0.5;

real Pwater;

real xwater;

real cathode_Psat;

real cathode_n_basis;

real n_basis_H2O_cathode;

real n_air_dry;

real n_O2_dry;

real n_N2_dry;

real cathode_m_basis;

real cathode_y_H2O;

real cathode_y_O2;

real cathode_y_N2;

real O2_press;

real cathode_conc;

real cathode_H2O_act;

real cathode_H2O_conc;
```

```
real cathode_H2O_conc_avg;

real volume = C_VOLUME(c,t);

/* mole fraction calculation */

RH = 0.8; /* relative humidity at the anode (fraction) */

//RH_cathode = 0.25; /* relative humidity at the cathode (fraction) */

/* Antoine coefficients (T in celcius) */

A = 8.10765;

B = 1750.286;

C = 235;

exp1 = (A - B/((T-273)+C));

base1= 10;

P_sat = pow(base1,exp1); /* Saturation Pressure (mm Hg) */

P_H2O = RH*(P_sat*(101.325/760)); /* Water vapour pressure (kPa) */

x_H2O = P_H2O*1000/P0; /* x_H2O is mole fraction/y_H2O is mass fraction */

cathode_Psat = P_sat;

Pwater = RH_cathode*(cathode_Psat*(101.325/760)); /* Water vapour pressure (kPa) */

xwater = Pwater*1000/P0; /* x_H2O is mole fraction/y_H2O is mass fraction */

/*mole to mass fractions-anode */

n_basis = 100; /* moles of feed (basis) */

m_basis = (x_H2O*n_basis)*18 + ((1-x_H2O)*n_basis)*2;
```

```
y_H2O = ((x_H2O*n_basis)*18)/m_basis;

y_H2 = 1-y_H2O;


/*mole to mass fractions-cathode */

cathode_n_basis = 100; /* moles of feed (basis) */

n_basis_H2O_cathode = xwater*cathode_n_basis;

n_air_dry = cathode_n_basis - n_basis_H2O_cathode;

n_O2_dry = 0.21*n_air_dry;

n_N2_dry = 0.79*n_air_dry;

cathode_m_basis = (n_basis_H2O_cathode)*18 + (n_O2_dry)*32 + (n_N2_dry)*28;


cathode_y_H2O = (n_basis_H2O_cathode*18)/cathode_m_basis;

cathode_y_O2 = (n_O2_dry*32)/cathode_m_basis;

cathode_y_N2 = 1-cathode_y_H2O-cathode_y_O2;


/* Pressure and H2O activation calculations */

P_H2 = (y_H2*R*T*C_R(c,t))/0.002;

O2_press = (cathode_y_O2*R*T*C_R(c,t))/0.032;


conc_anode = y_H2*C_R(c,t)/M_H2;

cathode_conc = cathode_y_O2*C_R(c,t)/M_O2;


H2O_act_anode = y_H2O*R*T*C_R(c,t)/(0.018*(P_H2O*1000)); /* water activity (for net drag and concentration calc's) */
```

```
cathode_H2O_act = cathode_y_H2O*R*T*C_R(c,t)/(0.018*(Pwater*1000)); /* water activity (for net drag and concentration calc's) */


/* electro-osmotic drag and water concentration */

mem_thick = 0.23e-3;

mem_density = 2000.0;

mem_mass = 1.1;


if(H2O_act_anode <= 1)

{

   n_d = 0.0049 + 2.02*H2O_act_anode - 4.53*pow(H2O_act_anode,2) +
   4.09*pow(H2O_act_anode,3);

   H2O_conc_anode = (mem_density/mem_mass)*(0.043 + 17.8*H2O_act_anode -
   39.8*pow(H2O_act_anode,2) + 36*pow(H2O_act_anode,3));

}

else if(H2O_act_anode > 1)

{

   n_d = 1.59 + 0.159*(H2O_act_anode -1);

   H2O_conc_anode = (mem_density/mem_mass)*(14+1.4*(H2O_act_anode-1));

}


if(cathode_H2O_act <= 1)

{

    cathode_H2O_conc = (mem_density/mem_mass)*(0.043 + 17.8*cathode_H2O_act -
    39.8*pow(cathode_H2O_act,2) + 36*pow(cathode_H2O_act,3));

}

else if(cathode_H2O_act > 1)
```

```
{
    cathode_H2O_conc = (mem_density/mem_mass)*(14+1.4*(cathode_H2O_act-1));
}
tot_volume = volume;
H2O_conc_anode_avg = H2O_conc_anode*volume;

cathode_H2O_conc_avg = cathode_H2O_conc*volume;
n_d_avg = n_d*volume;
D_H2O = 5.5e-11*n_d*exp(2416*((1/303)-(1/T)));
D_H2O_avg = D_H2O*volume;

/*net water transfer coefficient*/
alpha = n_d_avg - ((F*D_H2O_avg*(cathode_H2O_conc_avg-
H2O_conc_anode_avg))/(i*mem_thick))
/*water source term at cathode*/
if (THREAD_ID(t)== 2)
{
    cathode_H2O_source = (((i*M_H2O)*(1+2*alpha))/(2*F*A_int));
    dS[eqn] = 0;
}
else
{
    cathode_H2O_source = dS[eqn] = 0;
}
return cathode_H2O_source;
}
```

```
/*****************************************************************************************************************/
/* WATER VAPOUR ANODE SOURCES TERMS */
/*****************************************************************************************************************/
DEFINE_SOURCE(anode_H2O_source,c,t,dS,eqn)
{
/* constants for saturation pressure and water activity*/
real x[ND_ND];
real anode_H2O_source;
real M_H2O = 0.018;
real A_int = 0.0625/1000;
real T = 353;
real R = 8.314; /* Universal Gas constant (J/mol.K) */
real F = 96485.4; /*Faradays constant (C/mol) */
real A;
real B;
real C;
real RH;
real exp1;
real base1;
real P_sat; /* Saturation pressure (Pa) */
real P0 = 100000*2; /* atmosphereic pressure (Pa) */
real P_H2;
real x_H2O;
real P_H2O;
real n_basis;
```

```
real m_basis;

real y_H2O;

real y_H2;

real H2O_act_anode;

real i = 5000;

real alpha;

/* constants for electro-osmotic drag and water concentration */

real n_d; /*electro-osmotic drag coefficient */

real H2O_conc_anode;


real mem_density; /* membrane dry desnity (kg/m3) */

real mem_mass; /* membrane dry mass (kg/mol) */

real mem_thick; /* membrane thickness (m) */

real tot_volume;

real H2O_conc_anode_avg;

real n_d_avg;

/* water diffusivity */

real D_H2O;

real D_H2O_avg;

real M_H2 = 2e-3; /* Molecular weight of Hydrogen kg/mol */

real M_O2 = 32e-3; /* Molecular weight of Oxygen kg/mol */

real conc_anode;


/* cathode side terms */

real RH_cathode = 0.5;

real Pwater;
```

```
real xwater;

real cathode_Psat;

real cathode_n_basis;

real n_basis_H2O_cathode;

real n_air_dry;

real n_O2_dry;

real n_N2_dry;

real cathode_m_basis;

real cathode_y_H2O;

real cathode_y_O2;

real cathode_y_N2;

real O2_press;

real cathode_conc;

real cathode_H2O_act;

real cathode_H2O_conc;

real cathode_H2O_conc_avg;


real volume = C_VOLUME(c,t);


/* mole fraction calculation */

RH = 0.8; /* relative humidity at the anode (fraction) */

//RH_cathode = 0.25; /* relative humidity at the cathode (fraction) */

/* Antoine coefficients (T in celcius) */

A = 8.10765;

B = 1750.286;

C = 235;
```

```
exp1 = (A - B/((T-273)+C));

base1= 10;

P_sat = pow(base1,exp1); /* Saturation Pressure (mm Hg) */

P_H2O = RH*(P_sat*(101.325/760)); /* Water vapour pressure (kPa) */

x_H2O = P_H2O*1000/P0; /* x_H2O is mole fraction/y_H2O is mass fraction */

cathode_Psat = P_sat;

Pwater = RH_cathode*(cathode_Psat*(101.325/760)); /* Water vapour pressure (kPa) */

xwater = Pwater*1000/P0; /* x_H2O is mole fraction/y_H2O is mass fraction */


/*mole to mass fractions-anode */

n_basis = 100; /* moles of feed (basis) */

m_basis = (x_H2O*n_basis)*18 + ((1-x_H2O)*n_basis)*2;


y_H2O = ((x_H2O*n_basis)*18)/m_basis;

y_H2 = 1-y_H2O;


/*mole to mass fractions-cathode */

cathode_n_basis = 100; /* moles of feed (basis) */

n_basis_H2O_cathode = xwater*cathode_n_basis;

n_air_dry = cathode_n_basis - n_basis_H2O_cathode;

n_O2_dry = 0.21*n_air_dry;

n_N2_dry = 0.79*n_air_dry;

cathode_m_basis = (n_basis_H2O_cathode)*18 + (n_O2_dry)*32 + (n_N2_dry)*28;


cathode_y_H2O = (n_basis_H2O_cathode*18)/cathode_m_basis;

cathode_y_O2 = (n_O2_dry*32)/cathode_m_basis;
```

```
cathode_y_N2 = 1-cathode_y_H2O-cathode_y_O2;

/* Pressure and H2O activation calculations */

P_H2 = (y_H2*R*T*C_R(c,t))/0.002;

O2_press = (cathode_y_O2*R*T*C_R(c,t))/0.032;

conc_anode = y_H2*C_R(c,t)/M_H2;

cathode_conc = cathode_y_O2*C_R(c,t)/M_O2;

H2O_act_anode = y_H2O*R*T*C_R(c,t)/(0.018*(P_H2O*1000)); /* water activity (for net drag and concentration calc's) */

cathode_H2O_act = cathode_y_H2O*R*T*C_R(c,t)/(0.018*(Pwater*1000)); /* water activity (for net drag and concentration calc's) */

/* electro-osmotic drag and water concentration */

mem_thick = 0.23e-3;

mem_density = 2000.0;

mem_mass = 1.1;

if(H2O_act_anode <= 1)

{

   n_d = 0.0049 + 2.02*H2O_act_anode - 4.53*pow(H2O_act_anode,2) +
   4.09*pow(H2O_act_anode,3);

   H2O_conc_anode = (mem_density/mem_mass)*(0.043 + 17.8*H2O_act_anode -
   39.8*pow(H2O_act_anode,2) + 36*pow(H2O_act_anode,3));

}
```

```
else if(H2O_act_anode > 1)
{
   n_d = 1.59 + 0.159*(H2O_act_anode -1);
   H2O_conc_anode = (mem_density/mem_mass)*(14+1.4*(H2O_act_anode-1));
}

if(cathode_H2O_act <= 1)
{
   cathode_H2O_conc = (mem_density/mem_mass)*(0.043 + 17.8*cathode_H2O_act -
   39.8*pow(cathode_H2O_act,2) + 36*pow(cathode_H2O_act,3));
}
else if(cathode_H2O_act > 1)
{
   cathode_H2O_conc = (mem_density/mem_mass)*(14+1.4*(cathode_H2O_act-1));
}
tot_volume = volume;
H2O_conc_anode_avg = H2O_conc_anode*volume;

cathode_H2O_conc_avg = cathode_H2O_conc*volume;
n_d_avg = n_d*volume;
D_H2O = 5.5e-11*n_d*exp(2416*((1/303)-(1/T)));
D_H2O_avg = D_H2O*volume;

/*net water transfer coefficient*/
alpha = n_d_avg - ((F*D_H2O_avg*(cathode_H2O_conc_avg-
H2O_conc_anode_avg))/((i+0.000001)*mem_thick));
```

```
/*water source term at cathode*/
if (THREAD_ID(t)== 2)
{
    anode_H2O_source = -(((i*M_H2O)*alpha)/(F*A_int));
    dS[eqn] = 0;
}
else
{
    anode_H2O_source = dS[eqn] = 0;
}
return anode_H2O_source;
}
```